APPLICATION OF BiCONJUGATE GRADIENT STABILIZED METHOD WITH SPECTRAL ACCELERATION FOR PROPAGATION OVER TERRAIN PROFILES

A THESIS

SUBMITTED TO THE DEPARTMENT OF ELECTRICAL AND ELECTRONICS ENGINEERING

AND THE INSTITUTE OF ENGINEERING AND SCIENCE

OF BILKENT UNIVERSITY

IN PARTIAL FULFILLMENT OF THE REQUIREMENTS

FOR THE DEGREE OF

MASTER OF SCIENCE

By

Barış Babaoğlu

October, 2003

I certify that I have read this thesis and that in my opinion it is fully adequate, in scope and in quality, as a thesis for the degree of Master of Science.

Prof. Dr. Ayhan Altıntaş (Supervisor)

I certify that I have read this thesis and that in my opinion it is fully adequate, in scope and in quality, as a thesis for the degree of Master of Science.

Asst. Prof. Vakur B. Erturk (Co-supervisor)

I certify that I have read this thesis and that in my opinion it is fully adequate, in scope and in quality, as a thesis for the degree of Master of Science.

Prof. Dr. Cevdet Aykanat

I certify that I have read this thesis and that in my opinion it is fully adequate, in scope and in quality, as a thesis for the degree of Master of Science.

Dr. Satılmış Topçu

Approved for the Institute of Engineering and Science

Prof. Dr. Mehmet Baray
Director of the Institute of Engineering and Science

ABSTRACT

APPLICATION OF BiCONJUGATE GRADIENT STABILIZED METHOD WITH SPECTRAL ACCELERATION FOR PROPAGATION OVER TERRAIN PROFILES

Barış Babaoğlu

M.S. in Electrical and Electronics Engineering

Supervisors: Prof. Ayhan Altıntaş, Asst. Prof. Vakur B. Ertürk

October 2003

Using the Method of Moments (MoM) for the computation of electromagnetic radiation / surface scattering problems is a very popular approach since obtained results are accurate and reliable. But the memory requirement in the MoM to solve discretized integral equations and the long computational time of $O(N^3)$ operation count (where N is the number of the surface unknowns) make the method less favorable when electrically large geometries are of interest. This limitation can be overcome by using BiConjugate Gradient Stabilized (BiCGSTAB) method, a non-stationary iterative technique that was developed to solve general asymmetric/non-Hermitian systems with an operational cost of $O(N^2)$ per iteration. Furthermore, the computational time can be improved by the spectral acceleration (SA) algorithm which can be applied in any iterative technique. In this thesis, Spectrally Accelerated BiCGSTAB (SA-BiCGSTAB) method is processed over systems that have huge number of unknowns resulting a computational cost and memory requirement of $O(N)$ per iteration. Applications are presented on electrically large rough terrain profiles. The accuracy of the method is compared with MoM, conventional BiCGSTAB method and Spectrally Accelerated Forward-Backward Method (SA-FBM) where available.

Keywords: Electromagnetic rough surface scattering, Method of Moments, BiConjugate Gradient Stabilized method, Spectral Acceleration.

ÖZET

SPEKTRAL HIZLANDIRILMIŞ BiEŞLENİK GRADYAN STABİL YÖNTEMİ İLE ARAZİ KESİTLERİNDE DALGA YAYINIMI UYGULAMALARI

Barış Babaoğlu

Elektrik Elektronik Mühendisliği Bölümü Yüksek Lisans

Tez Yöneticileri: Prof. Ayhan Altıntaş, Yrd. Doç. Vakur B. Ertürk

Ekim 2003

Ulaşılan sonuçların doğruluğu ve güvenilirliğinden dolayı, Moment Metodunun (MoM) elektromanyetik ışınım / yüzey saçınımı hesaplamalarında kullanılması oldukça popüler bir yaklaşımdır. Ancak ayrıklaştırılmış integral denklemlerinin çözülmesi için gerekli hafıza ihtiyacı ve $O(N^3)$'lük uzun hesaplama süresi, bu metodu elektriksel olarak geniş geometriler söz konusu olduğunda gözden düşürmektedir. Bu limitasyon, BiEşlenik Gradyan Stabil (BiCGSTAB) yöntemi kullanarak üstesinden gelinebilir. BiCGSTAB yöntemi, genel asimetrik ve Hermisyon olmayan sistemleri, her iterasyonda $O(N^2)$'lik işlem sayısı yaparak çözmek için geliştirilen durağan olmayan bir iteratif tekniktir. Bunun da ötesinde hesaplama süresi, herhangi bir iteratif yönteme uygulanabilen spektral hızlandırma (SA) algoritmasıyla geliştirilebilir. Bu tezde spektral hızlandırılmış BiCGSTAB (SA-BiCGSTAB) metodu çok fazla sayıda bilinmeyeni bulunan sistemlere tatbik edilmiş, sonuçta hesaplama süresi ve hafıza gereksinimi her iterasyonda $O(N)$'e düşürülmüştür. Uygulamalar elektriksel geniş pürüzlü arazi kesitleri üzerinde gösterilmiştir. Sonuçların doğruluğu MoM, olağan BiCGSTAB yöntemi ve de uygun yerlerde Spektral Hızlandırılmış İleri-Geri (SA-FBM) yöntemiyle karşılaştırılmıştır.

Anahtar Kelimeler: Elektromanyetik pürüzlü yüzey saçınımı, Moment Metodu, BiEşlenik Gradyan Stabil yöntemi, Spektral Hızlandırma

Acknowledgement

I would like to express my deepest gratitude to my supervisors Prof. Ayhan Altıntaş and Asst. Prof. Vakur B. Ertürk for their supervisions, suggestions and encouragement throughout the development of this thesis.

I am also indebted to Prof. Dr. Cevdet Aykanat and Dr. Satılmış Topçu, the members of my jury, accepting to read and review this thesis and for their guidance.

I would also like to thank Gökhan Moral at ISYAM, for his astonishing patience for answering my awkward questions about the FORTRAN software programming language and as well as my colleague Celal Alp Tunç for supplying significant resources for the development of this thesis.

It is a great pleasure to express my special thanks to my family who brought me to this stage with their endless patience and dedication. Finally, I would like to thank Seha, for her unconditional love and interest she has shown during all the phases of this thesis; without her, this thesis would not be possible.

To my family and Seha …

Contents

List of Figures

List of Tables

Chapter 1

Introduction

During the past years, the mobile radio communication industry has grown enormously, powered by digital RF fabrication improvements, large-scale circuit integration and other technologies which make the mobile radio equipment smaller, cheaper but most important, reliable. Since then the study of coverage analysis and propagation losses for wireless communications has been of great interest. The radio spectrum allocation is the basis of RF communications, and it is closely tied to coverage analysis, computation of interference and propagation losses.

In this regard, the accurate prediction of electromagnetic field strengths over large areas (i.e., terrain propagation) in different environments has great importance. Thus, the main problem is related to the computation of precise solution. A great number of solution techniques have been developed. The first class of these techniques is based on propagation prediction models. These are the automatic tools for radio coverage prediction over geographical databases. The second class is the integral equation based methods dealing directly with Maxwell's equations for the computation of scattered field.

1.1 Propagation Prediction Models

These methods are focused on propagation loss and coverage analysis according to their nature. Also they are fast to apply for the investigation of scattered fields. There are three approaches for predicting field patterns, namely, empirical, heuristic and deterministic.

As the name suggests, the empirical method involves the experience of measurements. Okumura – Hata method [1] is a well known example of such approach. Empirical models interest on the geometrical data at the level of categorization. For instance, for urban, sub-urban and the rural areas, different formulae may be issued. The drawback of these methods is that they mainly focus on the field attenuation. The effects of diffraction and reflection due to obstacles in the region of interest are omitted.

Heuristic methods usually depend on high frequency asymptotic principles for the diffraction losses. Well known examples for these methods are Spherical Earth Knife–Edge algorithm [2] based on knife–edge diffraction assumption, Geometrical Theory of Diffraction (GTD) [3] using wedge diffractions including finite conductivity and local roughness effects. Since these methods require more detailed information about the environment than the empirical models, complex geometries defining the number of Knife–Edges or wedges make the usage of the methods overwhelming.

Deterministic models are issued for the simulation of radio wave propagation and are concerned with the computation of radio channel properties related with the description of geographical environment. Most of these approaches depend on ray tracing algorithms, whose computational complexity is prohibitive. Another variant of this kind of methods is a parabolic approximation to the Helmholtz equation, derived for both integral and differential forms [4]-[6]. Nevertheless parabolic approximation assumes that the propagation of the field is addressed through the forward direction. Thus, the backscattered field contribution is omitted.

One should note that there is a trade-off between the accuracy of the prediction and the computational speed in propagation models. As the precision

of the technique is increased, the order of the complexity to define the geographical area of interest also enlarges which creates long CPU times.

1.2 Integral Equation Methods Based On Terrain Propagation

These are numerical methods dealing directly with the solution of Maxwell equations; therefore hesitation in the electromagnetic analysis would be prevented. Moreover, they can be used as a reference solution for the validation of prediction methods and to obtain the limits of these methods under certain circumstances. Many of the integral equations (IE) are based on Method of Moments (MoM) [7]. This method proceeds to find the value of each unknown (for example, current distribution on a rough surface), which is the solution of discretized problem. But when the total number of unknowns, *N*, is very large (dealing with electrically large surface geometries), the solution of such problem grows exponentially in terms of computational CPU time and storage requirements. Direct solution methods of the MoM, such as LU decomposition requires an operational cost of $O(N^3)$. This has led to the development of iterative schemes to reduce computational count to $O(N^2)$.

The first application of IE based method to the terrain propagation problem can be found in [8] where an IE is applied over small terrain profiles. Nevertheless, due to computational cost associated with the number of unknowns, the application of the method on the electrically large profiles is unfeasible. A bit more improved method in terms of computational cost is proposed in [9] with some specific considerations, such as neglecting backscattering and deducing magnetic conductivity. The assumptions make the method less reliable and still time consuming. Later on, in [10] an IE formulation is used in conjunction with an iterative version of MoM known as Banded Matrix Iterative Approach (BMIA). Limited with some certain

problems, a parallel implementation of the method is applicable. However the method maintains the computation complexity.

A more efficient solution is given in [11], in which Fast Far Field Approximation (FAFFA) was introduced and modified for an IE formulation. In this approach, method succeeds in massive computational savings when compared to the previous attempts to apply surface an IE to terrain propagation problem. Until FAFFA algorithm, all previous IE methods required $O(N^2)$ operations per iteration whereas FAFFA achieves $O(N^{4/3})$ operations per iteration.

1.3 Iterative Approaches On One-Dimensional Rough Surface Scattering

When the problem is to evaluate the current distribution over rough surface by means of an iterative method, two different approaches have recently been followed depending on the updating estimates. In the first one, so called stationary technique, the current is updated by applying the surface boundary conditions to the scattered field with the previous iteration's current. Forward – Backward Method (FBM) [12] is a well known technique. It sweeps the surface on the forward and backward directions to find the forward and backward contributions due to the current element located at a fixed observation point. FBM was proposed for calculating the electromagnetic current on ocean-like perfectly electric conducting (PEC) surfaces at low grazing angles. The method gives accurate results within very few iterations but the computational cost is still $O(N^2)$. Furthermore, due to its stationary nature, the method fails to converge when the surface of interest is not ordered (reentrant surface of a ship). The second class of iterative approaches is the non-stationary techniques. These are the extensions of Standard Conjugate Gradient method [13] that were developed to solve general asymmetric/non Hermition systems and therefore do

not attempt to solve the physical multiple scattering of electromagnetic energy directly. Examples of these are given in [14] where BiConjugate Gradient Method (BiCG) is used, Generalized Conjugate Gradient (GCG) used in [15], preconditioned multi-grid Generalized Conjugate Residual (GCR) approach used in [16] and Quasi-minimum Residual (QMR) employed in [17].

All of the methods mentioned previously require an operation count of $O(N^2)$ (except the FAFFA algorithm). Thus when they are associated to solve very-large scale problems, the computational cost prohibits their applicability. However in 1996, Chou and Johnson [18] proposed a spectral acceleration (SA) algorithm to overcome the limitation on slightly rough large scale problems.

The algorithm accelerates the matrix-vector multiplies taking place in the iterative process and divides contributions between points in strong and weak regions. The algorithm is mainly based on a spectral representation of two-dimensional Green's function.

This technique reduces the computational cost and memory requirements to $O(N)$ and the Spectrally Accelerated Forward – Backward Method (SA-FBM) can be applied over electrically large surfaces. But one should note that the original implementation of spectral acceleration is utilized for slightly rough quasi-planar surfaces and may not be suitable for undulating rough geometries.

With the development of SA, the restriction on large-scale problem will no longer exist but to deal with terrain propagation with the large height deviations, a modified version of SA is proposed in [19]. This algorithm implements SA–FBM to very undulating rough surfaces and the computational cost still remains at $O(N)$. Although the algorithm is utilized firstly for the conventional FBM, since it sweeps forward and backward directions on the surface of the scatterer, it can be used in any iterative method.

The SA algorithm was utilized in conjunction with a non-stationary technique BiCG method firstly by Valero [20] in order scattering from the strip gratings.

In this thesis, electrically large rough terrain profiles have been examined with Spectrally Accelerated Biconjugate Gradient Stabilized Method (SA-BiCGSTAB). It should be emphasized that, this sort of implementation of BiCGSTAB method has not existed in the literature yet.

One other novelty of this method is the analysis of multi-valued (reentrant) surface profiles (like a ship on the sea). The conventional stationary techniques can not solve this kind of problems. A generalized version of the FBM (GFBM) [21] was offered to deal with such problem. The method includes significant changes in the decomposition of the system interaction matrix. Because of this decomposition, the approach requires an additional work and more storage requirement at each operation, which can be overwhelming if the multi-valued section is too large. In this context, GFBM can not compete with SA-BiCGSTAB method.

In order to reach these goals, a large number of implementations of SA-BiCGSTAB over various kinds of examples are presented. To show the ability of convergence, the results are compared with MoM, BiCGSTAB, GFBM and SA-FBM, respectively.

All fields and currents in this work are considered to have a time-harmonic dependence of the form $e^{j\omega k}$ that is suppressed from the expressions. The angular frequency is ω and k is the wave number of the medium, which is assumed to be free space, above the rough surface.

Chapter 2

Scattering Problem for 1D Rough Surfaces and Method of Moments (MoM)

2.1 Introduction

This chapter deals with the evaluation of the current distribution over a terrain profile on which an electromagnetic source is incident. To reduce the problem into two dimensions, the surface considered for such problem is assumed to have no variation along the transverse direction of the propagating field. The variation of the height at the surface along the displacement (x-axis) is characterized with the curve C and defined by $z = f(x)$ as depicted in Figure 2.1, yielding the roughness of the surface in one dimension. The electromagnetic fields characterized by $\mathbf{E}^i(\boldsymbol{\rho})$ and $\mathbf{H}^i(\boldsymbol{\rho})$, are incident upon the surface where $\boldsymbol{\rho} = \hat{x}\, x + \hat{z}\, z$. The terrain profile is modeled to be an imperfect conductor (with permeability μ, and permittivity ϵ) and analyzed using an impedance boundary condition (IBC) [22]-[23] to be able to investigate more general situations.

This chapter is devoted to the discussion of integral equations in order to find current distribution on the surface of the scatterer. The formulations of integral equations are described in Section 2.2. Corresponding matrix equations to solve these integral equations are determined in Section 2.3.

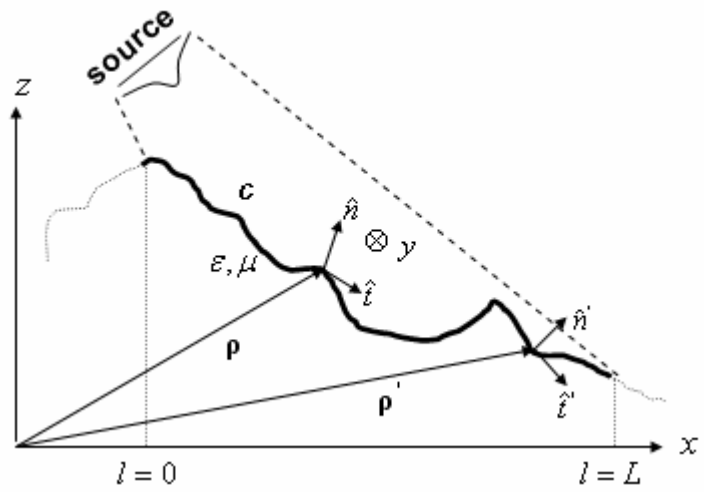

Figure 2.1. A generic terrain profile.

2.2 Electric and Magnetic Field Integral Equations

The main objective of the solution of such a scattering problem is determining the physical or equivalent current distribution behavior on the surface of the scatterer. Once they are known then, the scattered fields can be evaluated by using standard radiation integrals. The method used to solve the system should be capable of finding current densities over terrain profiles accurately. This task can be achieved by an integral equation (IE) method.

In general there are many forms of integral equations. Two of the most popular examples for the time-harmonic electromagnetic fields are known as *electric field integral equation* (EFIE) and *magnetic field integral equation* (MFIE). The EFIE enforces the boundary condition on the tangential electric field and the MFIE enforces the boundary condition on the tangential components of the magnetic field. EFIE will be employed for horizontal polarization, namely, transverse magnetic (TM) case, and MFIE discussion will be shown for vertical polarization, namely, transverse electric (TE) case. In each case an IBC approximation will be used. The IBC implies that only the electric and magnetic fields external to the scatterer are relevant and their

relationship is a function of the material constitution (i.e., surface impedance) or surface characteristics (i.e., roughness) of the scatterer.

2.2.1 EFIE for Horizontal Polarization

Given that the IBC approximation is applied for a given scatterer shown in Figure 2.1, the total (incident plus scattered) electric field external to the surface, $\mathbf{E^t}$, is related as

$$\mathbf{E^t} - (\hat{n} \cdot \mathbf{E^t})\hat{n} = \eta_s(\hat{n} \times \mathbf{H^t}), \tag{2.1}$$

and from the duality condition, total magnetic field $\mathbf{H^t}$ yields

$$\mathbf{H^t} - (\hat{n} \cdot \mathbf{H^t})\hat{n} = \frac{-1}{\eta_s}(\hat{n} \times \mathbf{E^t}), \tag{2.2}$$

where η_s is the surface impedance and $\hat{n}$ is the unit surface normal of the terrain. The surface impedance is assumed to be constant throughout this paper but it can be easily modified if it varies along *x*-axis by replacing with $\eta_s(\rho)$. When the incident field has a horizontal polarization, (i.e., $\mathbf{E^i} = \hat{y}\, E_y$), (2.1) is reduced to

$$\mathbf{E^t} = \eta_s(\hat{n} \times \mathbf{H^t}). \tag{2.3}$$

The electric surface current density induced on the surface along *y* direction is defined as

$$\mathbf{J}_s(\boldsymbol{\rho}) = \hat{n} \times \mathbf{H^t} \tag{2.4}$$

yielding (2.1)

$$\mathbf{E^t} = \mathbf{E}^i + \mathbf{E}^s = \eta_s \mathbf{J}(\boldsymbol{\rho}) \tag{2.5}$$

where $\mathbf{E^i}$ denotes the incident field and $\mathbf{E^s}$ denotes scattered field above the scatterer. The scattered electric field is a superposition of **A** and **F**, the magnetic and electric auxiliary vector potentials, respectively [24];

$$\mathbf{E^s} = \mathbf{E_A} + \mathbf{E_F} = -j\omega\mathbf{A} - j\frac{1}{\omega\mu\varepsilon}\nabla\left(\nabla.\mathbf{A}\right) - \frac{1}{\varepsilon}\nabla \mathrm{x}\mathbf{F} \qquad (2.6)$$

where **A** and **F** are shown to be

$$\mathbf{A} = \frac{\mu}{4\pi}\iint_S \mathbf{J_s}(\boldsymbol{\rho}')\frac{e^{-jkR}}{R}ds' \qquad (2.7)$$

$$\mathbf{F} = \frac{\varepsilon}{4\pi}\iint_S \mathbf{M_s}(\boldsymbol{\rho}')\frac{e^{-jkR}}{R}ds' \qquad (2.8)$$

where, the prime coordinates denote the source points, *S* is the surface of the scatterer at the source points, $\mathbf{M_s}$ is the equivalent magnetic current on the surface and *R* is the distance from the source point to observation point given by

$$R = \sqrt{(y-y')^2 + \left|\boldsymbol{\rho} - \boldsymbol{\rho}'\right|}. \qquad (2.9)$$

Since the incident electric field is only $\hat{y}$ directed, the scattered and total electric fields have only $\hat{y}$ directed components which are independent of *y* variations (two dimensional). Therefore, the scattered electric field can be found by assuming that **A** has only y component which has no variations along the *y*-axis. Consequently, (2.6) reduces to

$$\mathbf{E^s} = -j\omega\mathbf{A} - \frac{1}{\varepsilon}\nabla \mathrm{x}\mathbf{F}\,. \qquad (2.10)$$

Substituting (2.7) and (2.8) into (2.10) and making the use of following relation hip between electric and magnetic currents given by

$$\mathbf{M}_s = \mathbf{E^t}\ \mathrm{x}\ \hat{\mathbf{n}} = -\eta_s(\hat{n}\ \mathrm{x}\ \mathbf{J}_s) \qquad (2.11)$$

which can be implied from (2.1) and (2.2), the scattered electric field is obtained as

$$\mathbf{E^s} = -j\omega\mu\iint_S \mathbf{J_s}(\boldsymbol{\rho}')G(\mathbf{r},\mathbf{r}')ds' + \eta_s\nabla \mathrm{x}\iint_S (\hat{n}'\mathrm{x}\mathbf{J_s}(\boldsymbol{\rho}'))\ G(\mathbf{r},\mathbf{r}')ds' \qquad (2.12)$$

where $G(\mathbf{r}, \mathbf{r'})$ is the three dimensional free space Green's function given by

$$G(\mathbf{r},\mathbf{r}') = \frac{e^{-jkR}}{4\pi R}. \tag{2.13}$$

To simplify the second integral at the right hand side of (2.12), we benefit from the vector identity

$$\nabla x(\mathbf{V}\psi) = \psi\nabla x\mathbf{V} - \mathbf{V}x\nabla\psi \tag{2.14}$$

Substituting (2.14) into (2.12) yields

$$\nabla x[(\hat{n}'x\mathbf{J}_s)G] = G\nabla x(\hat{n}'x\mathbf{J}_s) + \nabla G x(\hat{n}'x\mathbf{J}_s). \tag{2.15}$$

Furthermore, the following vector identity

$$\mathbf{V}_1x(\mathbf{V}_2x\mathbf{V}_3) = (\mathbf{V}_1.\mathbf{V}_3)\mathbf{V}_2 - (\mathbf{V}_1.\mathbf{V}_2)\mathbf{V}_3 \tag{2.16}$$

to expand the relationship at the first term of the right hand side of (2.14) results

$$G\nabla x(\hat{n}'x\mathbf{J}_s) = G\left\{(\nabla.\mathbf{J}_s)\hat{n}' - (\nabla.\hat{n}')\mathbf{J}_s\right\} = 0 \tag{2.17}$$

such that the divergence of the surface current and the divergence of unit vector related with the source coordinate is equal to zero. Consequently, the second term at the right hand side of (2.15) becomes

$$\begin{aligned}\nabla Gx(\hat{n}'x\mathbf{J}_s) &= (\nabla G.\mathbf{J}_s)\hat{n}' - (\hat{n}'.\nabla G)\mathbf{J}_s \\ &= -(\hat{n}'.\nabla G)\mathbf{J}_s\end{aligned} \tag{2.18}$$

since the gradient of the Green's function and current vector are perpendicular to each other. Thus the final expression for (2.12) is simplified to:

$$\begin{aligned}\mathbf{E}^s = -j\omega\mu\int_C\int_{-\infty}^{+\infty}\mathbf{J}_s(\boldsymbol{\rho}')G(\mathbf{r},\mathbf{r}')dy'd\rho' - \\ \eta_s\int_C\int_{-\infty}^{+\infty}\mathbf{J}_s(\boldsymbol{\rho}')\,\hat{n}'.\nabla G(\mathbf{r},\mathbf{r}')dy'd\rho'\end{aligned} \tag{2.19}$$

where C is the terrain contour. Using the fact that

$$\int_{-\infty}^{+\infty}\frac{e^{-j\alpha\sqrt{\beta^2+l^2}}}{\sqrt{\beta^2+l^2}}dl = -j\pi H_0^{(2)}(\alpha\beta). \tag{2.20}$$

where $H_0^{(2)}$ is the Hankel function of second kind and order zero, and expressing R as given in (2.9) , the scattered field expression in (2.19) becomes

$$\mathbf{E^s} = -\frac{\omega\mu}{4}\int_C \mathbf{J_s}(\boldsymbol{\rho}')H_0^{(2)}(k|\boldsymbol{\rho}-\boldsymbol{\rho}'|)d\rho' - j\frac{k\eta_s}{4}\int_C \mathbf{J_s}(\boldsymbol{\rho}')\,\hat{n}'.\hat{\boldsymbol{\rho}}\,H_1^{(2)}(k|\boldsymbol{\rho}-\boldsymbol{\rho}'|)d\rho' \tag{2.21}$$

where $H_1^{(2)}$ is the Hankel function of second kind of order one. Substituting (2.21) into (2.5), one obtains

$$-E_y^i(\boldsymbol{\rho}|_{\rho=\rho_s}) = -\eta_s J_y(\boldsymbol{\rho}|_{\rho=\rho_s}) - \frac{\omega\mu}{4}\int_C J_y(\boldsymbol{\rho}')H_0^{(2)}(k|\boldsymbol{\rho}-\boldsymbol{\rho}'|)d\rho' - j\frac{k\eta_s}{4}\int_C J_y(\boldsymbol{\rho}')\,\hat{n}'.\hat{\boldsymbol{\rho}}\,H_1^{(2)}(k|\boldsymbol{\rho}-\boldsymbol{\rho}'|)d\rho'. \tag{2.22}$$

Equation (2.22) is referred as the *electric field integral equation* (EFIE) that will be used for impedance surfaces. Note that, the corresponding EFIE for a perfectly electric conducting (PEC) scatterer case can be obtained from (2.22) replacing η_s by 0, which results

$$-E_y^i(\boldsymbol{\rho}|_{\rho=\rho_s}) = -\frac{\omega\mu}{4}\int_C J_y(\boldsymbol{\rho}')H_0^{(2)}(k|\boldsymbol{\rho}-\boldsymbol{\rho}'|)d\rho'. \tag{2.23}$$

Equations (2.22) and (2.23) can be used to find the unknown current density $J_y(\boldsymbol{\rho}')$ at any point on the surface of the terrain profile. Then the scattered field can be computed via this current density.

2.2.2 MFIE for TE Polarization

For the transverse electric case, (i.e., $\mathbf{H^i} = \hat{y}\,\mathrm{H_y}$) since the incident magnetic field is directed along the $\hat{y}$ direction, the current induced on the surface has

only a component which is tangential to *C.* That is,

$$\mathbf{J}_s = \hat{t}\,J_t(\boldsymbol{\rho}), \quad \hat{t} = \hat{y}\ \mathrm{x}\ \hat{n}. \tag{2.24}$$

On the surface of the terrain the current density, related to the incident and scattered fields for the geometry of Figure 2.1, can be written as:

$$\begin{aligned}\mathbf{J}_s|_C &= \hat{t}\, J_t(\boldsymbol{\rho})|_C = \hat{n}\ \mathrm{x}(\mathbf{H}^i+\mathbf{H}^s)|_C \\ &= \hat{n}\ \mathrm{x}\ \hat{y}\, H_y\,|_C\ +\ \hat{n}\ \mathrm{x}\ \mathbf{H}^s|_C \\ &= -\hat{t}\, H_y\,|_C + \hat{n}\ \mathrm{x}\ \mathbf{H}^s|_C.\end{aligned} \tag{2.25}$$

Since left and right sides of (2.25) have only tangential components, the second term at the right hand side of the (2.25) must have a tangential component. So (2.25) can be written as

$$J_s|_C = -H_y\,|_C + \hat{t}.[\hat{n}\ \mathrm{x}\ \mathbf{H}^s|_C]. \tag{2.26}$$

Similar to the scattered electric field, the scattered magnetic field can be written as a superposition of magnetic and the electric auxiliary vector potentials **A** and **F**, respectively

$$\mathbf{H}^s = \mathbf{H}_\mathbf{F} + \mathbf{H}_\mathbf{A} = \frac{1}{\mu}\nabla \mathrm{x}\mathbf{A} - j\omega\mathbf{F} - j\frac{1}{\omega\mu\varepsilon}\nabla\left(\nabla.\mathbf{F}\right). \tag{2.27}$$

Since the scattered magnetic field has only a *y* component, the scattered and total magnetic fields have y components which are independent of *y* variations (two dimensional). Therefore the scattered field can be found by expanding (2.27), assuming **F** has only a *y* component which does not have a *y* variation, (2.27) reduces to

$$\mathbf{H}^s = \frac{1}{\mu}\nabla \mathrm{x}\mathbf{A} - j\omega\mathbf{F}. \tag{2.28}$$

Expanding (2.28) in terms of induced surface currents, the scattered magnetic field is obtained as

$$\begin{aligned}\mathbf{H}^s = \nabla \mathrm{x}\iint_S (\hat{t}'J_t(\rho'))G(\mathbf{r},\mathbf{r}')ds' \ + \\ + j\omega\varepsilon\eta_s \iint_S [\hat{n}'\ \mathrm{x}\ (\hat{t}'J_t(\rho'))]\ G(\mathbf{r},\mathbf{r}')ds'.\end{aligned} \tag{2.29}$$

By the use of (2.14), the first integral at the right hand side of (2.29) reduces to

$$\nabla \mathrm{x} \iint_S (\hat{t}' J_t(\boldsymbol{\rho}')) G(\mathbf{r},\mathbf{r}') ds' = -\iint_S (\hat{t}' J_t(\boldsymbol{\rho}')) \mathrm{x} [\nabla G(\mathbf{r},\mathbf{r}')] ds' \quad (2.30)$$

where $G(\mathbf{r}, \mathbf{r}')$ is the Green's function given by (2.13). To find the tangential component of the scattered field for the boundary condition in (2.26), the explicit expression is given by

$$\hat{t}.[\hat{n} \mathrm{x} \mathbf{H}^s] = -\iint_S J_t(\boldsymbol{\rho}') \, \hat{t}.\{\hat{n} \mathrm{x}[\hat{t}' \mathrm{x} \nabla' G(\mathbf{r},\mathbf{r}')]\} ds' + + j\omega\varepsilon\eta_s \iint_S \hat{t}.\{\hat{n} \mathrm{x}[\hat{n}' \mathrm{x} (\hat{t}' J_t(\rho'))]\} \mathrm{G}(\mathbf{r},\mathbf{r}') ds'. \quad (2.31)$$

Substituting $\hat{t}' = -\hat{n}' \mathrm{x} \hat{y}$ to evaluate dot and cross products of the first term of at the right hand side of (2.31), one obtains

$$\begin{aligned} -\hat{t}.\{\hat{n} \mathrm{x} [\hat{t}' \mathrm{x} \nabla G]\} &= -\hat{t}.\{\hat{n} \mathrm{x} [(-\hat{n}' \mathrm{x} \hat{y}) \mathrm{x} \nabla G]\} \\ &= -\hat{t}.\{\hat{n} \mathrm{x} [-\hat{y}(\hat{n}' \,.\, \nabla G) + \hat{n}'(\hat{y} \,.\nabla G)]\} \\ &= -\hat{t}.\{\hat{n} \mathrm{x} [-\hat{y}(\hat{n}' \,.\, \nabla G)]\} \\ &= -\hat{t}.\, \hat{t}(\hat{n}' \,.\, \nabla G) = -\hat{n}' \,.\, \nabla G. \end{aligned} \quad (2.32)$$

Note that the gradient of the Green's function and the $\hat{y}$ directed unit vector are perpendicular to each other. Furthermore, dot and cross products of the second term of at the right hand side of (2.31) are treated as follow;

$$\begin{aligned} \hat{t}.\{\hat{n} \mathrm{x}[\hat{n}' \mathrm{x} \hat{t}']\} &= \hat{t}.\{\hat{n}' \, (\hat{n}.\hat{t}') - \hat{t}' \, (\hat{n}.\hat{n}')\} \\ &= \hat{t}.\{-\hat{t}' \, (\hat{n}.\hat{n}')\} = -1. \end{aligned} \quad (2.33)$$

Where C is the contour of the terrain, substituting results of (2.32) and (2.33) into (2.31) results in

$$\hat{t}.[\hat{n} \mathrm{x} \mathbf{H}^s] = -\int_C \int_{-\infty}^{+\infty} J_t(\boldsymbol{\rho}') \, \hat{n}'.\nabla G(\mathbf{r},\mathbf{r}') dy' d\rho' - j\omega\varepsilon\eta_s \int_C \int_{-\infty}^{+\infty} J_t(\boldsymbol{\rho}') G(\mathbf{r},\mathbf{r}') dy' d\rho'. \quad (2.34)$$

Substituting R as given in (2.9) and using (2.20), (2.34) will turn into:

$$\hat{t}.[\hat{n} \text{ x } \mathbf{H}^{s}] = -j\frac{k}{4}\int_{C} J_t(\boldsymbol{\rho}')\,\hat{n}'.\,\hat{\boldsymbol{\rho}}\,H_1^{(2)}(k|\boldsymbol{\rho}-\boldsymbol{\rho}'|)d\rho' - \frac{\omega\varepsilon\eta_s}{4}\int_{C} J_t(\boldsymbol{\rho}')H_0^{(2)}(k|\boldsymbol{\rho}-\boldsymbol{\rho}'|)d\rho'. \quad (2.35)$$

If we substitute (2.35) into (2.26) and rearrange it, we obtain

$$-H_y^i(\rho|_{\rho=\rho_s}) = J_t(\boldsymbol{\rho}|_{\rho=\rho_s}) + j\frac{k}{4}\int_{c} J_t(\boldsymbol{\rho}')\,\hat{n}'.\,\hat{\boldsymbol{\rho}}\,H_1^{(2)}(k|\boldsymbol{\rho}-\boldsymbol{\rho}'|)d\rho' + \frac{\omega\varepsilon\eta_s}{4}\int_{c} J_t(\boldsymbol{\rho}')H_0^{(2)}(k|\boldsymbol{\rho}-\boldsymbol{\rho}'|)d\rho', \quad (2.36)$$

Equation (2.36) is referred as the *magnetic field integral equation* (MFIE) for impedance surfaces. Note that, the corresponding MFIE for a perfectly electric conducting (PEC) scatterer case can be obtained from (2.36) replacing η_s by 0, which results

$$-H_y^i(\rho|_{\rho=\rho_s}) = J_t(\boldsymbol{\rho}|_{\rho=\rho_s}) + j\frac{k}{4}\int_{c} J_t(\boldsymbol{\rho}')\,\hat{n}'.\,\hat{\boldsymbol{\rho}}\,H_1^{(2)}(k|\boldsymbol{\rho}-\boldsymbol{\rho}'|)d\rho'. \quad (2.37)$$

Equations (2.36) and (2.37) can be used to find the unknown current density $J_y(\boldsymbol{\rho}')$ at any point on the surface of the terrain profile. Then the scattered field can be computed via this current density.

Solution of the integral equations (2.22) and (2.36) to find unknown currents is not analytically possible. Therefore, a method of moments (MoM) solution has been developed for the investigation of the induced current, as explained in the following chapter.

2.3 Method of Moments (MoM) Formulation

Although the terrain *C* has an arbitrary extension, the incident field on the surface is considered to be finite so that the illuminated rough surface and, consequently the integration in equations (2.22) and (2.36) can be confined to a finite region of length L. Thus, these equations can be solved by using a

numerical technique called method of moments (MoM). In this thesis, MoM is used in conjunction with the point matching technique. The surface of the scatterer is divided into *N* segments. Then, unknown current distribution on the scatterer surface is expanded in *N* terms of basis functions, forming *N* unknown current coefficients. Each current coefficient is associated with a segment of the scatterer surface. Therefore, at a fixed observation point due to the incident field, one obtains a single equation with *N* unknowns. Then enforcing the field at each observation point on the surface, *N* linearly independent equations are found. Consequently, the integral equation is transformed into a linear system equation which is easier to be solved.

2.3.1 Point Matching Method

The EFIE in (2.22) and the MFIE in (2.36) are solved for the unknown surface current density $\boldsymbol{J}_s(\boldsymbol{\rho}')$ using MoM procedure. Namely, first the surface current density is expanded in terms of a finite series of the form of

$$J_s(\boldsymbol{\rho}') = \sum_{m=1}^{N} I_m g_m(\boldsymbol{\rho}') \tag{2.38}$$

where $g_m(\boldsymbol{\rho}')$ represents each known *basis (expansion)* function and I_m is the unknown coefficients of this basis function to be determined at the end of MoM procedure When (2.38) is substituted into (2.23) or (2.36) for a *n*th observation point on the scatterer surface;

$$\begin{aligned} -T_y^i(\boldsymbol{\rho})|_{T=E,H} &= c_1 \sum_{m=1}^{N} I_m g_m(\boldsymbol{\rho}) + c_2 \int_C \sum_{m=1}^{N} I_m g_m(\boldsymbol{\rho}')\, H_0^{(2)}(k\,|\boldsymbol{\rho}-\boldsymbol{\rho}_m|)\, d\rho' \\ &\quad + c_3 \int_C \sum_{m=1}^{N} I_m g_m(\boldsymbol{\rho}')\, \hat{n}'.\hat{\boldsymbol{\rho}}\, H_1^{(2)}(|\boldsymbol{\rho}-\boldsymbol{\rho}_m|)\, d\rho' \end{aligned} \tag{2.39}$$

where $c_1 = -\eta_s$, $c_2 = -\omega\mu/4$ and $c_3 = -jk\eta_s/4$ for the EFIE. And for the MFIE, $c_1 = \eta_s$, $c_2 = \omega\varepsilon\eta_s/4$ and $c_3 = jk/4$. Expression given by (2.39) can be illustrated in general as

$$v = \sum_{m=1}^{N} I_m F(g_m) \tag{2.40}$$

where

$$v = -T_y^i(\boldsymbol{\rho})|_{T=E,H}$$

$$F(\rho_m) = c_1 \sum_{m=1}^{N} g_m(\boldsymbol{\rho}) + c_2 \int_C \sum_{m=1}^{N} g_m(\boldsymbol{\rho}')\, H_0^{(2)}(k\,|\boldsymbol{\rho} - \boldsymbol{\rho}_m|)\, d\rho' \tag{2.41}$$

$$+ c_3 \int_C \sum_{m=1}^{N} g_m(\boldsymbol{\rho}')\, \hat{n}'.\hat{\boldsymbol{\rho}}\, H_1^{(2)}(|\boldsymbol{\rho} - \boldsymbol{\rho}_m|)\, d\rho'.$$

In (2.41), F is called as the linear integral operator, g_m is the response function and v is the excitation function. A numerical solution of (2.41) for a single observation point $\boldsymbol{\rho} = \boldsymbol{\rho_n}$ leads to one equation with N unknowns. If we repeat this N time by choosing N observation points, we have a system of N linear equations with N unknowns. Since this linear system was derived by applying boundary conditions at N discrete points, the technique is called as the *point matching method*. To improve the point matching method solution, a vector inner product can be defined as:

$$\langle \mathbf{w}, \mathbf{g} \rangle = \iint_S \mathbf{w}^*.\mathbf{g}\, ds, \tag{2.42}$$

where * is the conjugate of a vector, w is the *weighting* functions and S is the surface of the structure to be analyzed. This weighting factor of basis functions is a better approximation instead of single point matching method.

2.3.2 Weighted Residuals for Point Matching

The point matching method enforces the electromagnetic boundary condition only at discrete points. Between these points the boundary conditions may not be satisfied so that a residual error may occur between the exact boundary condition and the one found by point matching method. To minimize this residual, the method of *weighted residuals* is utilized in conjunction with the inner product in (2.42). This technique is called the *method of moments*

(MoM). MoM forces the boundary conditions to be satisfied in average sense over the entire surface. To achieve this situation, we define a set of *N weighting* functions $\{w_n\} = w_1, w_2, \ldots\ldots w_N$ in the domain of the operator *F*. If we take the inner products between each side of (2.38),

$$\langle w_n, v\rangle = \sum_{m=1}^{N} I_m \langle w_n, F(g_m)\rangle \quad n = 1, 2, \ldots\ldots N \tag{2.43}$$

In this thesis a set of Dirac delta weighting functions, i.e., $\delta(p - p_n)$ where p is a position with respect to origin and p_n is the point at which the boundary condition is enforced, is used to reduce number of required operations (integrals coming from vector inner product). When we utilize these weighting functions in (2.40) and use (2.42) as the inner product, (2.40) becomes

$$\begin{aligned}
&\langle \delta(p - p_n), v\rangle = \sum_{m=1}^{N} I_m \langle \delta(p - p_n)\ , F(g_m)\rangle \quad n = 1, 2, \ldots\ldots N \\
&\iint_S \delta(p - p_n) v\ ds = \sum_{m=1}^{N} I_m \iint_S \delta(p - p_n) F(g_m)\ ds \quad n = 1, 2, \ldots\ldots N \\
&v|_{p=p_n} = \sum_{m=1}^{N} I_m F(g_m)|_{p=p_n} \qquad n = 1, 2, \ldots\ldots N.
\end{aligned} \tag{2.44}$$

So we deal with only the remaining integrations whose specified by $F(g_m)$ in equation (2.41).

2.3.3 MoM Formulation for EFIE

The set of *N* equations in (2.41) may be written in the matrix form of,

$$\bar{\mathbf{Z}} \ .\ \mathbf{I} = \mathbf{V} \tag{2.45}$$

where $\bar{\mathbf{Z}}$ is the impedance matrix. $\mathbf{V}$ is the excitation vector due to electromagnetic source at the match points whose elements are given by

$$v_n = -E_y^i(\boldsymbol{\rho}_n). \tag{2.46}$$

For the linear integral operator *F*, if we use *pulse* basis function which can be denoted as:

$$g_m(\boldsymbol{\rho}') = \begin{cases} 1 & \boldsymbol{\rho}' \in m^{th}\ segment \\ 0 & \text{elsewhere} \end{cases} \tag{2.47}$$

than the impedance matrix elements in (2.45), for n^{th} receiving (observation) and m^{th} source points pair, can be approximated as [19]

$$Z_{nm} \cong \begin{cases} -\dfrac{\omega\mu}{4}\left[1 - j\dfrac{2}{\pi}\ln\left(\dfrac{\gamma k \Delta x_m}{4e}\right)\right]\Delta x_m - \dfrac{\eta_{\mathrm{m}}}{2} & n = m \\ -\dfrac{\omega\mu}{4}H_0^{(2)}(k|\boldsymbol{\rho}_n - \boldsymbol{\rho}_m|)\Delta x_m - j\dfrac{k\eta_{\mathrm{m}}}{4}\Delta x_m H_1^{(2)}(k|\boldsymbol{\rho}_n - \boldsymbol{\rho}_m|)\hat{n}_m'.\hat{\rho}_{nm} & n \neq m. \end{cases} \tag{2.48}$$

where $\gamma = 1.7811$ is the Euler constant , e is equal to 2.728, Δx_m is the distance between two consecutive source points (segment width) and η_m is the surface impedance at the point ρ_m. Off-diagonal matrix impedance entries can also be represented by the two dimensional Green's function, i.e.,

$$Z_{nm} \cong -j\omega\mu G(\boldsymbol{\rho}_n, \boldsymbol{\rho}_m)\Delta x_m + \eta_{\mathrm{m}}\Delta x_m \frac{\partial G(\boldsymbol{\rho}_n, \boldsymbol{\rho}_m)}{\partial n_m} \tag{2.49}$$

where

$$G(\boldsymbol{\rho}_n, \boldsymbol{\rho}_m) = \frac{H_0^{(2)}(k|\boldsymbol{\rho}_n - \boldsymbol{\rho}_m|)}{4j} \tag{2.50}$$

and the second term at the right hand side of (2.49) is partial derivative of the Green's function due to the normal vector at the source point.

Consequently, we transform the EFIE in (2.22) into a linear system equation given in (2.45) by the help of MoM.

2.3.4 MoM Formulation for MFIE

If we follow the same procedure for the MFIE in (2.36), by enforcing the field at the N match points and expanding the current in terms basis functions, we transform (2.36) to a linear system equation as given in (2.45) where the elements of the excitation vector **V** are

$$v_n = -H_y^i(\boldsymbol{\rho}_n). \tag{2.51}$$

By employing *pulse* basis function, the impedance matrix entries will be [19]

$$Z_{nm} \cong \begin{cases} \dfrac{\omega\varepsilon\eta_{\mathrm{m}}}{4}\left[1-j\dfrac{2}{\pi}\ln\left(\dfrac{\gamma k\Delta x_m}{4e}\right)\right]\Delta x_m + \dfrac{1}{2} & n = m \\ \dfrac{\omega\varepsilon\eta_{\mathrm{m}}}{4}H_0^{(2)}(k|\boldsymbol{\rho}_n-\boldsymbol{\rho}_m|)\Delta x_m + j\dfrac{k}{4}\Delta x_m H_1^{(2)}(k|\boldsymbol{\rho}_n-\boldsymbol{\rho}_m|)\hat{n}_m'.\,\hat{\rho}_{nm} & n \neq m. \end{cases} \tag{2.52}$$

Alternatively, the off-diagonal entries of the impedance matrix can be represented by the two-dimensional Green's function,

$$Z_{nm} \cong j\omega\varepsilon\eta_{\mathrm{m}}G(\boldsymbol{\rho}_n,\boldsymbol{\rho}_m)\Delta x_m - \Delta x_m\frac{\partial G(\boldsymbol{\rho}_n,\boldsymbol{\rho}_m)}{\partial n_m} \tag{2.52}$$

2.3.5 Solution of MoM

Once the impedance matrices given with the entries (2.48) for TM polarization and (2.52) for TE polarization are formed, the linear system equation in (2.45) should be solved for unknown current coefficients $\mathbf{I} = \{I_m\}$. The direct solution methods like Gaussian elimination and LU decomposition requires a computational cost of $O(N^3)$ where N is the number of unknowns. Hence, as the dimension of the problem gets larger, computational requirements of the MoM increases very rapidly. Nevertheless, less time consuming alternative methods are available to solve these linear system equations. These methods are called iterative methods resulting an operation count of $O(N^2)$ per

iteration. One of the variants of iterative processes named Gradient type of methods, is explained in Chapter 3.

Chapter 3

Gradient Type of Iterative Solvers and the Spectral Acceleration (SA) Algorithm

3.1 Introduction

The primary factor limiting the use of MoM in the calculation of electromagnetic scattering from rough surfaces is that a linear system equation must be solved to obtain currents induced on the scatterer. Direct solution methods such as LU decomposition require $O(N^3)$ operations, where N is the number of unknowns in the discretized representation of the surface current. Electrically larger scattering surfaces (for very large N) increase the computational cost of the method and make it intractable especially at high frequencies.

Using iterative techniques, computational cost is reduced to $O(N^2)$ operations per iteration. The basic will of an iterative process is to reach to the exact solution by updating estimates at each iteration. Two different approaches can be applied as iterative schemes to solve this system equation formed by MoM. These are, namely, stationary and non-stationary iterative techniques. In each of the method, different update schemes are used for the estimates to find the exact solution.

A method is called stationary if the rule to determine the estimates at each iteration does not change from iteration to iteration (i.e. the iteration matrix is stable during the process). In stationary iterative techniques, the surface current is approximated by physical optics approximation applied to the incident field [25]. The current is then updated by applying surface boundary condition. Kapp and Brown [26] and Holliday *et al.* [12] choose the ordering of the updates to follow multiple scattering paths on the surface. This led Kapp and Brown and Holliday *et al.* to name their approaches as method of ordered multiple interactions (MOMI) and forward backward method (FBM), respectively. Such two techniques have shown a very effective and rapid convergence activities to solve linear system equations constructed by MFIE in vertical polarization case and EFIE in horizontal polarization case for the PEC and non-PEC surfaces which are single valued and rough in one dimension. But when the ordering of the scatterer is multi-valued (reentrant surfaces), divergence problem occur.

Non-stationary techniques are the second kind of iterative methods used to solve systems formed by MoM solution. These methods are extensions of standard conjugate gradient (CG) method [13] which converge to the exact solution assuming infinite precision by constructing orthogonal vector sequences. Examples are given by bi-conjugate gradient (BiCG) method used in [14] generalized conjugate gradient (GCG) method [15] and quasi-minimum residual (QMR) method [17] are some typical examples. These methods are developed to solve asymmetric/non-Hermitian complex linear systems and hence, their algorithms are different than those of stationary methods. In these kinds of methods, the rule to determine the estimates changes from iteration to iteration. The rule is based on orthogonality conditions in the space defining the linear system equation. Consequently, a new iteration matrix is generated at every iteration step to update the estimates.

This chapter is devoted to the discussion of gradient type methods and an acceleration algorithm which can be applied on such methods. The properties of conjugate gradient type methods are presented in Section 3.2. Numerical results for BiCG Stabilized methods are given in Section 3.3. The acceleration algorithm's assets are exhibited in Section 3.4.

3.2 Conjugate Gradient Type Methods

All of these methods explained below are assumed to solve a linear system given by $\bar{\mathbf{A}}\mathbf{x} = \mathbf{b}$. Here $\bar{\mathbf{A}}$ is a *N*x*N* interaction matrix, **b** is a response vector for the system and **x** is the unknown vector to be solved.

3.2.1 Conjugate Gradient Method

Being the oldest and best known nonstationary technique, the conjugate gradient method is an effective method for symmetric positive definite systems. The process, which stimulates the method is the generation of vector sequences of iterates (i.e., consecutive approximations to the solution), creating residuals that correspond to the iterates, and search directions that are used to update the iterates and residuals. Although the length of these sequences can become large, only a small number of vectors are needed to be kept in memory. In order to calculate update scalars that are defined to assure that the sequences fulfill certain orthogonality conditions, there are two inner products to be used at each iteration of the method. These conditions guarantee on a symmetric positive definite linear system that the distance to the true solution is minimized according to some standards.

The iterates $\mathbf{x}^{(i)}$ are updated in each iteration by a multiple α_i of the search direction vector $\mathbf{p}^{(i)}$:

$$\mathbf{x}^{(i)} = \mathbf{x}^{(i-1)} + \alpha_i \mathbf{p}^{(i)} \tag{3.1}$$

Correspondingly the residuals $\mathbf{r}^{(i)} = \mathbf{b} - \bar{\mathbf{A}}\,\mathbf{x}^{(i)}$ are updated as,

$$\mathbf{r}^{(i)} = \mathbf{r}^{(i-1)} - \alpha_i \mathbf{q}^{(i)} \tag{3.2}$$

where

$$\mathbf{q}^{(i)} = \bar{\mathbf{A}}\mathbf{p}^{(i)} . \tag{3.3}$$

The choice $\alpha_i = \mathbf{r}^{(i-1)^T}\mathbf{r}^{(i-1)} \;/\; \mathbf{p}^{(i)^T}\,\bar{\mathbf{A}}\mathbf{p}^{(i)}$ minimizes over all possible choices for α. The search directions are updated using the residuals

$$\mathbf{p}^{(i)} = \mathbf{r}^{(i-1)} + \beta_{i-1}\mathbf{p}^{(i-1)} \tag{3.4}$$

where the choice

$$\beta_i = \mathbf{r}^{(i)^T}\mathbf{r}^{(i-1)} \;/\; \mathbf{r}^{(i-1)^T}\mathbf{r}^{(i-1)} \tag{3.5}$$

ensures that $\mathbf{p}^{(i)}$ and $\bar{\mathbf{A}}\mathbf{p}^{(i)}$ (or equivalently $\mathbf{r}^{(i)}$ and $\mathbf{r}^{(i-1)}$) are orthogonal. In fact, one can show that this choice of β_i makes $\mathbf{p}^{(i)}$ and $\mathbf{r}^{(i)}$ orthogonal to *all* previous $\bar{\mathbf{A}}\mathbf{p}^{(j)}$ and $\mathbf{r}^{(j)}$ respectively.

As can be seen in the Figure 3.1, in the pseudo code [13] is given for the preconditioned conjugate gradient method, there is a preconditioner $\bar{\mathbf{M}}$. Preconditioners are very commonly used matrix forms which enhance the condition number of the original matrix $\bar{\mathbf{A}}$, thus generally reducing the number of iterations to converge to the solution of the linear system. But to construct a good preconditioner matrix which can improve the iterative technique by means of iteration, the effort in terms of computational cost is increased. For $\bar{\mathbf{M}} = \bar{\mathbf{I}}$ (where $\bar{\mathbf{I}}$ is the identity matrix), one takes the unpreconditioned version of the conjugate gradient algorithm. In that case, by omitting the "solve" line and replacing $\mathbf{z}^{(i-1)}$ by $\mathbf{r}^{(i-1)}$ (and $\mathbf{z}^{(0)}$ by $\mathbf{r}^{(0)}$), the algorithm may be further simplified. In this thesis, unpreconditioned versions of conjugate type methods are used because as it will be explained in Chapter 3.3, there is no need to store interaction matrix. Thus, it will be unnecessary to use a preconditioner matrix.

Pseudocode :

Compute $\mathbf{r}^{(0)} = \mathbf{b} - \bar{\mathbf{A}}\mathbf{x}^{(0)}$ for some initial guess $\mathbf{x}^{(0)}$.

for $i = 1, 2, ...$

  solve $\bar{\mathbf{M}}\mathbf{z}^{(i-1)} = \mathbf{r}^{(i-1)}$

  $\rho_{i-1} = \mathbf{r}^{(i-1)^T}\mathbf{z}^{(i-1)}$

  if $i = 1$

    $\mathbf{p}^{(1)} = \mathbf{z}^{(0)}$

  else

    $\beta_{i-1} = \rho_{i-1} / \rho_{i-2}$

    $\mathbf{p}^{(i)} = \mathbf{z}^{(i-1)} + \beta_{i-1}\mathbf{p}^{(i-1)}$

  endif

  $\mathbf{q}^{(i)} = \bar{\mathbf{A}}\mathbf{p}^{(i)}$

  $\alpha_i = \rho_{i-1} / \mathbf{p}^{(i)^T}\mathbf{q}^{(i)}$

  $\mathbf{x}^{(i)} = \mathbf{x}^{(i-1)} + \alpha_i\mathbf{p}^{(i)}$

  $\mathbf{r}^{(i)} = \mathbf{r}^{(i-1)} - \alpha_i\mathbf{q}^{(i)}$

  check convergence; continue if necessary

end

Figure 3.1 Pseudo code for the Conjugate Gradient method

The unpreconditioned conjugate gradient method creates the *i*th iterate $\mathbf{x}^{(i)}$ as an element of

$$\mathbf{x}^{(0)} + \text{span}\{\mathbf{r}^{(0)}, ..., \bar{\mathbf{A}}^{(i-1)}\mathbf{r}^{(0)}\} \tag{3.6}$$

so that

$$(\mathbf{x}^{(i)} - \mathbf{x}_e)^T \bar{\mathbf{A}} (\mathbf{x}^{(i)} - \mathbf{x}_e) \tag{3.7}$$

is minimized, where $\mathbf{x}_e$ is the exact solution of $\bar{\mathbf{A}}\mathbf{x} = \mathbf{b}$. The existence of this minimum can be assured in general only if $\bar{\mathbf{A}}$ is symmetric positive definite. Since the interaction matrices formed by MoM solutions in Chapter 2 are not positive definite, CG method is ineffective for our problem type. There are many variants of iterative techniques, which can handle linear system equations formed by the method of moments solution. These methods come out from the same origin. They depend on constructing orthogonal vector sequences which will be used to update the estimates for the next iteration.

3.2.2 BiConjugate Gradient Method

The conjugate gradient method is not suitable for nonsymmetrical systems In this case, the biconjugate gradient method (BiCG) can be used. BiCG substitutes the orthogonal sequence of residuals by two mutually orthogonal sequences, at the price of no longer providing a minimization. Nevertheless, the positive definiteness condition does not affect this method. So the method becomes suitable for the solution of electromagnetic scattering problem.

By using dual relations based on $\bar{\mathbf{A}}^T$ instead of $\bar{\mathbf{A}}$, the update relations for residuals in the conjugate gradient method can be amplified in the biconjugate gradient method Thus, we update two sequences of residuals

$$\mathbf{r}^{(i)} = \mathbf{r}^{(i-1)} - \alpha_i \bar{\mathbf{A}}\mathbf{p}^{(i)} \text{ and } \tilde{\mathbf{r}}^{(i)} = \tilde{\mathbf{r}}^{(i-1)} - \alpha_i \bar{\mathbf{A}}^T \tilde{\mathbf{p}}^{(i)}, \quad (3.8)$$

and two sequences of search directions

$$\mathbf{p}^{(i)} = \mathbf{r}^{(i-1)} - \beta_{i-1}\mathbf{p}^{(i)} \text{ and } \tilde{\mathbf{p}}^{(i)} = \tilde{\mathbf{r}}^{(i-1)} - \beta_{i-1}\tilde{\mathbf{p}}^{(i)}. \quad (3.9)$$

The choices:

$$\alpha_i = \frac{\tilde{\mathbf{r}}^{(i-1)^T}\mathbf{r}^{(i-1)^T}}{\tilde{\mathbf{p}}^{(i)^T}\bar{\mathbf{A}}\mathbf{p}^{(i)}} \text{ and } \beta_i = \frac{\tilde{\mathbf{r}}^{(i)^T}\mathbf{r}^{(i)^T}}{\tilde{\mathbf{r}}^{(i-1)^T}\mathbf{r}^{(i-1)^T}} \quad (3.10)$$

ensure the orthogonality conditions;

$$\tilde{\mathbf{r}}^{(i)^T}\mathbf{r}^{(j)^T} = \tilde{\mathbf{p}}^{(i)^T}\bar{\mathbf{A}}\mathbf{p}^{(j)} = 0. \quad (3.11)$$

if $i \neq j$. The pseudo code is given in Figure 3.2 [13].

The BiCG method delivers the same results as the conjugate gradient method for symmetric positive definite systems, but at twice the cost per iteration. In case of nonsymmetrical matrices, it has been revealed that the BiCG method is more or less comparable to the full biconjugate stabilized (BiCGSTAB) method with regards to number of iterations in phases of the process where there is significant reduction of the norm of the residual.

Pseudocode :

Compute $\mathbf{r}^{(0)} = \mathbf{b} - \bar{\mathbf{A}}\mathbf{x}^{(0)}$ for some initial guess $\mathbf{x}^{(0)}$.

Choose $\tilde{\mathbf{r}}^{(0)}$ (for example, $\tilde{\mathbf{r}}^{(0)} = \mathbf{r}^{(0)}$).

for $i = 1, 2, \ldots$

  solve $\bar{\mathbf{M}}\mathbf{z}^{(i-1)} = \mathbf{r}^{(i-1)}$

  solve $\bar{\mathbf{M}}^T\tilde{\mathbf{z}}^{(i-1)} = \tilde{\mathbf{r}}^{(i-1)}$

  $\rho_{i-1} = \mathbf{z}^{(i-1)^T}\tilde{\mathbf{r}}^{(i-1)}$

  if $i = 1$

    $\mathbf{p}^{(i)} = \mathbf{z}^{(i-1)}$

    $\tilde{\mathbf{p}}^{(i)} = \tilde{\mathbf{z}}^{(i-1)}$

  else

    $\beta_{i-1} = \rho_{i-1} / \rho_{i-2}$

    $\mathbf{p}^{(i)} = \mathbf{z}^{(i-1)} + \beta_{i-1}\mathbf{p}^{(i-1)}$

    $\tilde{\mathbf{p}}^{(i)} = \tilde{\mathbf{z}}^{(i-1)} + \beta_{i-1}\tilde{\mathbf{p}}^{(i-1)}$

  endif

  $\mathbf{q}^{(i)} = \bar{\mathbf{A}}\mathbf{p}^{(i)}$

  $\tilde{\mathbf{q}}^{(i)} = \bar{\mathbf{A}}^T\tilde{\mathbf{p}}^{(i)}$

  $\alpha_i = \rho_{i-1} / \tilde{\mathbf{p}}^{(i)^T}\mathbf{q}^{(i)}$

  $\mathbf{x}^{(i)} = \mathbf{x}^{(i-1)} + \alpha_i\mathbf{p}^{(i)}$

  $\mathbf{r}^{(i)} = \mathbf{r}^{(i-1)} - \alpha_i\mathbf{q}^{(i)}$

  $\tilde{\mathbf{r}}^{(i)} = \tilde{\mathbf{r}}^{(i-1)} - \alpha_i\tilde{\mathbf{q}}^{(i)}$

  check convergence; continue if necessary

end

Figure 3.2 Pseudo code for the Bi-Conjugate Gradient method

BiCG requires computing a matrix-vector product $\mathbf{Ap}^{(i)}$ and a transpose product $\bar{\mathbf{A}}^T\tilde{\mathbf{p}}^{(i)}$. In some applications, the latter product may be impossible to perform; in cases such as if the matrix is not constructed. In a parallel environment the two matrix-vector products can theoretically be carried out at the same time; however, in a distributed-memory environment, there will be extra communication costs associated with one of the two matrix-vector products, depending on the storage scheme for $\bar{\mathbf{A}}$. To lessen this problem a

duplicate copy of the matrix can be used, which performs at the cost of doubling the storage requirements for the matrix.

3.2.3 BiConjugate Gradient Stabilized Method

There are numerous alternatives of BiCG that raise the efficiency of this group of methods in some confident situations. One of the alternatives is biconjugate gradient stabilized method. BiCGSTAB often converges twice as fast as the BiCG. At least locally, a residual vector is minimized which results in a considerably smoother convergence behavior.

BiCGSTAB has two ending tests. The method may converge at the first test on the norm of $\boldsymbol{s}$ where $\boldsymbol{s}$ is a relation between the recent and preceding residual error vectors. Then the subsequent update would be numerically tentative. Ending on the first test avoids a few unnecessary operations as well. BiCGSTAB calls for two more inner products than those of biconjugate gradient method, i.e., two matrix-vector products versus four inner products. Since BiCGSTAB is the fastest one of all the other conjugate type methods in terms of iteration number, all of the numerical results in this thesis are evaluated by this algorithm.

It should be noted that the convergence ability of the conjugate type methods strongly depends on the condition number of the interaction matrix, the number of iterations to reach desired level of error varies with the properties of the matrix. For instance diagonally dominant matrices is fast to solve with the BiCGSTAB method, But when we are dealing with reentrant surfaces yielding large off-diagonal elements interaction matrices, the algorithm requires more iterations. Also the condition number is a function of maximum and minimum eigen values of the matrix. Thus, as the number of unknowns to be solved increases the number of iterations required for a converged result increases. The pseudo code is given in Figure 3.3 [13].

Pseudocode :

Compute $\mathbf{r}^{(0)} = \mathbf{b} - \bar{\mathbf{A}}\mathbf{x}^{(0)}$ for some initial guess $\mathbf{x}^{(0)}$.

Choose $\tilde{\mathbf{r}}$ (for example, $\tilde{\mathbf{r}} = \mathbf{r}^{(0)}$).

for $i = 1, 2, ...$

$\rho_{i-1} = \tilde{\mathbf{r}}^T \mathbf{r}^{(i-1)}$

if $\rho_{i-1} = 0$, method fails

if $i = 1$

$\mathbf{p}^{(i)} = \mathbf{r}^{(i-1)}$

else

$\beta_{i-1} = (\rho_{i-1} / \rho_{i-2}) / (\alpha_{i-1} / \omega_{i-1})$

$\mathbf{p}^{(i)} = \mathbf{r}^{(i-1)} + \beta_{i-1}(\mathbf{p}^{(i-1)} - \omega_{i-1}\mathbf{v}^{(i-1)})$

endif

solve $\bar{\mathbf{M}}\hat{\mathbf{p}} = \mathbf{p}^{(i)}$

$\mathbf{v}^{(i)} = \bar{\mathbf{A}}\hat{\mathbf{p}}$

$\alpha_i = \rho_{i-1} / \tilde{\mathbf{r}}^T \mathbf{v}^{(i)}$

$\mathbf{s} = \mathbf{r}^{(i-1)} - \alpha_i \mathbf{v}^{(i)}$

check norm of $\mathbf{s}$; if small enough: set $\mathbf{x}^{(i)} = \mathbf{x}^{(i-1)} + \alpha_i \hat{\mathbf{p}}$ and stop

solve $\bar{\mathbf{M}}\hat{\mathbf{s}} = \mathbf{s}$

$\mathbf{t} = \bar{\mathbf{A}}\hat{\mathbf{s}}$

$\omega_i = \mathbf{t}^T \mathbf{s} / \mathbf{t}^T \mathbf{t}$

$\mathbf{x}^{(i)} = \mathbf{x}^{(i-1)} + \alpha_i \hat{\mathbf{p}} + \omega_i \hat{\mathbf{s}}$

$\mathbf{r}^{(i)} = \mathbf{s} - \omega_i \mathbf{t}$

check convergence; continue if necessary

for continuation it is necessary that $\omega_i \neq 0$

end

Figure 3.3 Pseudo code for the BiConjugate Gradient Stabilized method

Method	Inner Product	SS	Matrix-Vector Prod.
BiCG	2	5	2
BiCGSTAB	4	6	2

Table 3.1 Operation count per iteration for BiCG and BiCGSTAB methods

Summary of operations per iteration for conventional BiCG and BiCGSTAB methods are given in Table 3.1. SS is the vector summations and subtractions number.

The storage requirements for conventional BiCG and BiCGSTAB methods are given in Table 3.2. *N* is the number of unknowns. On the other hand, the matrix storage requirement can be avoided at the cost of reevaluating each matrix entry at each iteration.

Method	**Storage Requirement**
BiCG	Matrix + 10*N*
BiCGSTAB	Matrix + 11*N*

Table 3.2 Storage requirements for BiCG and BiCGSTAB methods

3.3 Numerical Results for the BiCGSTAB Method

In this section, some numerical results are presented to validate the convergence and accuracy of the Biconjugate Stabilized method over one-dimensional rough terrain profiles. Applying method of moments, a matrix equation is formed to obtain the unknown current coefficients

$$\bar{\mathbf{Z}} \,.\, \mathbf{I} \;=\; \mathbf{V} \tag{3.12}$$

where the elements of the impedance matrices are given by (2.48) for TM polarization and given by (2.52) for TE polarization, respectively. Results are obtained both for perfect and imperfect conductor surfaces. In order to check the accuracy of the method, results are compared with the method of moments. The pulse width in point matching technique is taken as $\Delta x = \lambda / 10$. Residual error is employed as a stopping criterion of the iterative method. The residual error vector at the i^{th} iteration step is defined as

$$\mathbf{r}^i = \mathbf{V} - \bar{\mathbf{Z}} \cdot \mathbf{I}^i \tag{3.13}$$

and the corresponding residual error is given as,

$$residual\ error = \frac{\| \mathbf{r}^i \|}{\| \mathbf{V} \|} \tag{3.14}$$

where $\| \cdot \|$ denotes the vector norm. The stopping criterion of the BiCGSTAB method is limited by the residual error of 10^{-3} in this thesis. It has been seen that this error rate is sufficient to obtain accurate results.

3.3.1 Source Incident on the Terrain Profile

Three kinds of sources are considered in this thesis. The first one is finite end plane wave as shown in Figure 3.4(a). The elements of the excitation vector, the right hand side of (2.46), for the TM polarization than will be

$$v_n = E^i(\boldsymbol{\rho}_n) = \begin{cases} -e^{-jk(x_n \cos\theta - z_n \sin\theta)} & \text{, on the surface} \\ 0 & \text{, elsewhere} \end{cases} \tag{3.15}$$

where the subscript n denotes the location of observation points on the terrain. For the TE polarization, the elements of the right hand side of (2.51) can be expressed as

$$v_n = -H^i(\boldsymbol{\rho}_n) = \frac{1}{\eta_0} \begin{cases} -e^{-jk(x_n \cos\theta - z_n \sin\theta)} & \text{, on the surface} \\ 0 & \text{, elsewhere} \end{cases} . \tag{3.16}$$

The second source is an isotropic radiator located above the surface as shown in Figure 3.4(b). The elements of the of the excitation vector will be for TM and TE cases are

$$v_n = -E^i(\boldsymbol{\rho}_n) = -E_0 \frac{e^{-jkd_n}}{d_n} \tag{3.17}$$

and

$$v_n = -H^i(\boldsymbol{\rho}_n) = -\frac{E_0}{\eta_0} \frac{e^{-jkd_n}}{d_n}, \tag{3.18}$$

respectively. The source distance d_n is

$$d_n = \sqrt{(x_n - x_s)^2 + (z_n - z_s)^2} \ . \tag{3.19}$$

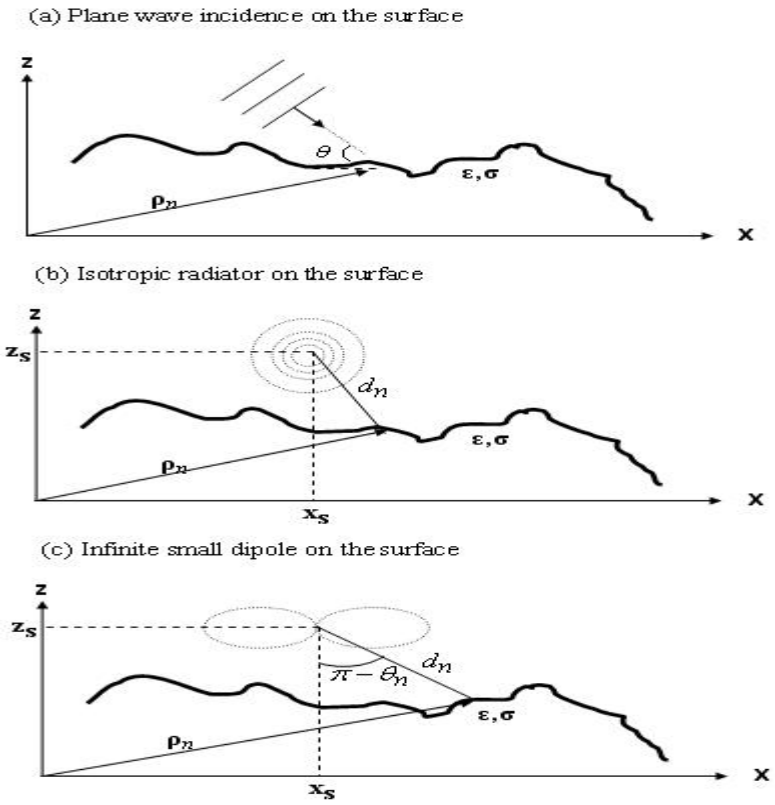

Figure 3.4 Sources incident on the terrain profile

Using the radiation density integral in [27] to find the average transmitted power, we can evaluate the magnitude of the electric field as:

$$P_{rad} = \int_{\theta=0}^{\pi} \int_{\phi=0}^{2\pi} \frac{|E_0|^2}{2\eta} \sin\theta d\theta d\phi \tag{3.20}$$

and

$$E_0 = \sqrt{60 P_{rad}} \ . \tag{3.21}$$

The last source considered here is an infinitesimal dipole depicted in Figure 3.4(c). For this type of source elements of the incident field vector for both vertical and horizontal polarizations are:

$$v_n = -E^i(\boldsymbol{\rho}_n) = -E_0 \frac{e^{-jkd_n}}{d_n} \sin\theta_n \tag{3.22}$$

and

$$v_n = -H^i(\boldsymbol{\rho}_n) = -\frac{E_0}{\eta_0} \frac{e^{-jkd_n}}{d_n} \sin\theta_n \tag{3.23}$$

where

$$\sin\theta_n = \frac{x_n - x_s}{d_n} \ . \tag{3.24}$$

The electric field magnitude will be:

$$E_0 = \sqrt{90 P_{rad}} \ . \tag{3.25}$$

3.3.2 Applications of BiCGSTAB over Rough Surfaces

Operating frequency is chosen to be 300MHz, which yields to 1 meters wavelength for all of the results. Figure 3.5 shows a strip surface of width 50λ.

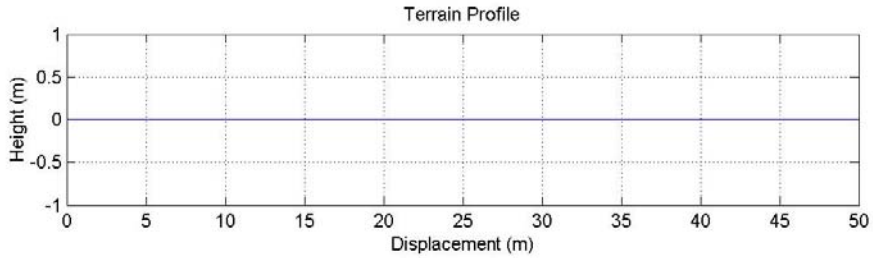

Figure 3.5 Strip surface of width 50λ

Plane wave incidence is considered for both TM and TE polarizations. Figure 3.6 shows results for oblique ($\theta = \pi / 2$) incidence. To see the absorption effects of the terrain profile, both PEC ($\eta_s = 0$) and imperfect conducting case are considered. For the non-PEC case the surface impedance is taken as $\eta_s = 17.6 + j16.8$. As can be seen in Figure 3.6(c), the TE polarized plane wave, induced on the strip for the PEC case, results a stable current on the

terrain profile. If we look at the interaction matrix entries in (2.45), we see that the self terms is equal to ½ since $\eta_m = 0$ and the mutual terms is equal to 0 since the unit vector $\hat{n}_m$ is always perpendicular to surface of the strip. This shows us that the tangential current in the MFIE is found to be:

$$J_t(\boldsymbol{\rho}) = -2H^i(\boldsymbol{\rho}) \tag{3.26}$$

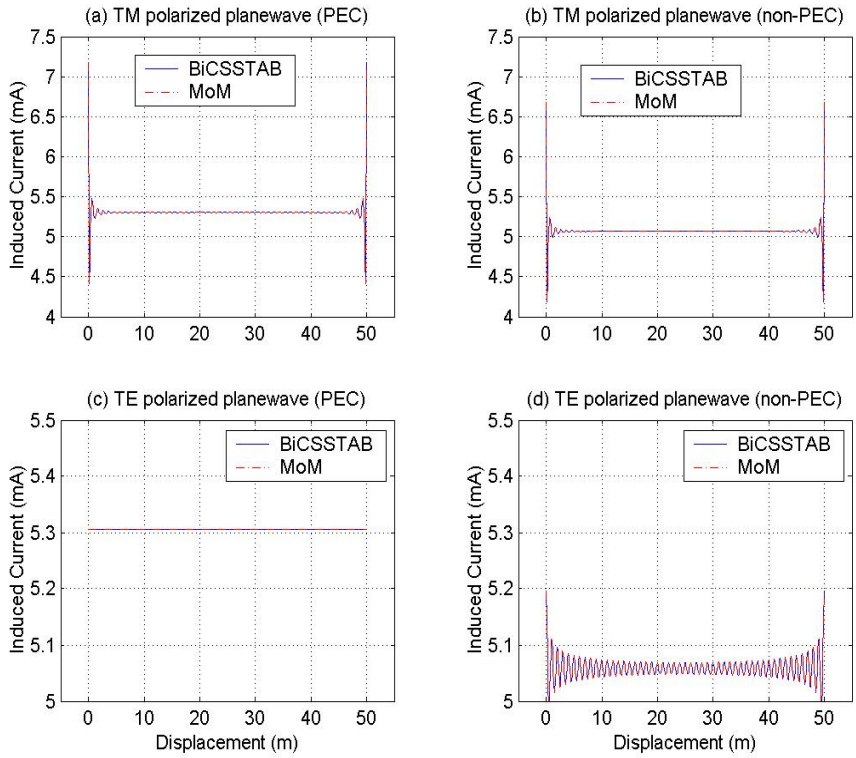

Figure 3.6 Distributed current on a strip, oblique plane wave incidence

This is a reliable result considering that the surface profile is extended to infinity, thus the induced current on an infinite strip is the physical optics current $\mathbf{J}_s^{PO} = 2\hat{n} \times \mathbf{H}^{inc}$. Hence, reaching accurate solution of the induced current over strip profiles for vertical polarization is not numerically possible. However, when the strip is imperfect conducting, the MFIE yields accurate results as shown in Figure 3.6(d). This is also true when we are dealing with

undulating geometries that the dot product term in (2.45), to find mutual elements interaction, does not vanish.

Figure 3.7 illustrates the residual errors of Figure 3.6. It can be clearly seen in Figure 3.7(a) and Figure3.7 (b) that non-PEC case reaches at the desired level of error in a faster way. Also for the TE polarization case, the convergence ability is higher since the interaction matrix formed by MFIE is more diagonally dominant compared with one formed by EFIE for TM case.

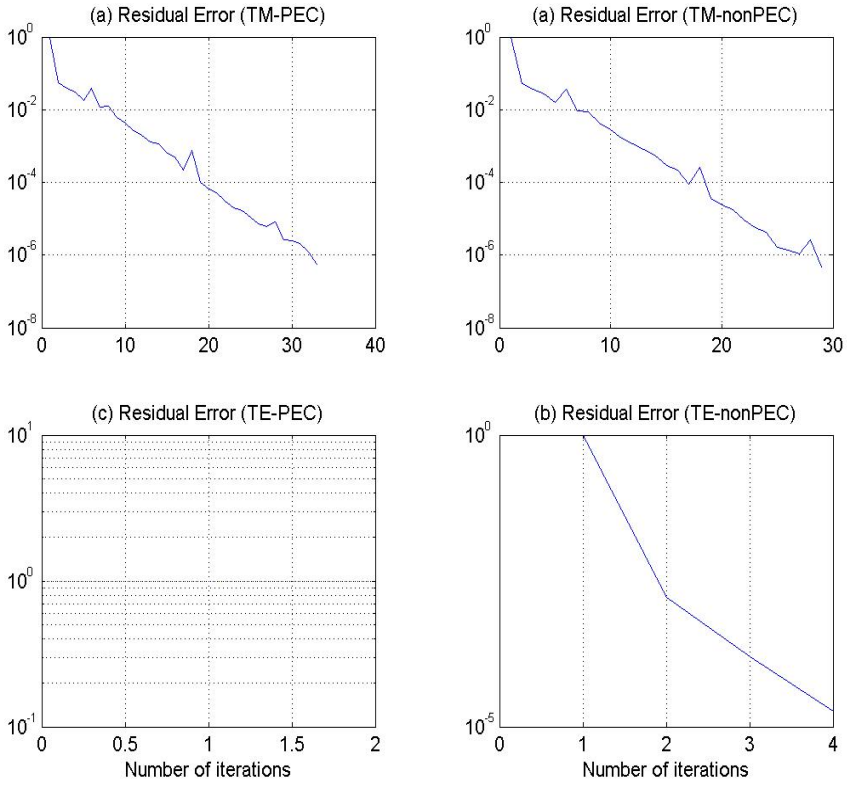

Figure 3.7 Residual errors of Figure 3.6

Figure 3.8 shows a rough surface of width 100λ illuminated by a plane wave for both polarization cases. Maximum height deviation is about 21λ.The incident angle is now $\theta = \pi / 20$ (grazing incidence). Imperfect conducting case is considered with $\eta_s = 17.6 + j16.8$. Results show that the BiCGSTAB

converges successfully. Because of grazing angle condition, shadowing effects are seen after the hill of the terrain. The residual errors with respect to the iteration number are given in Figure 3.9.

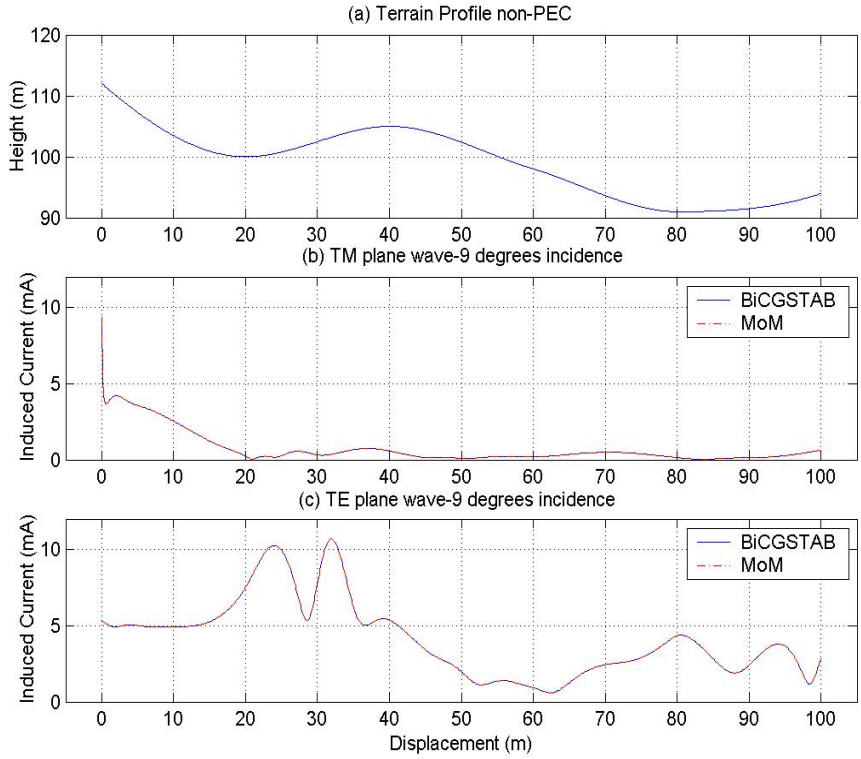

Figure 3.8 Distributed current on a 100λ rough surface, grazing plane wave

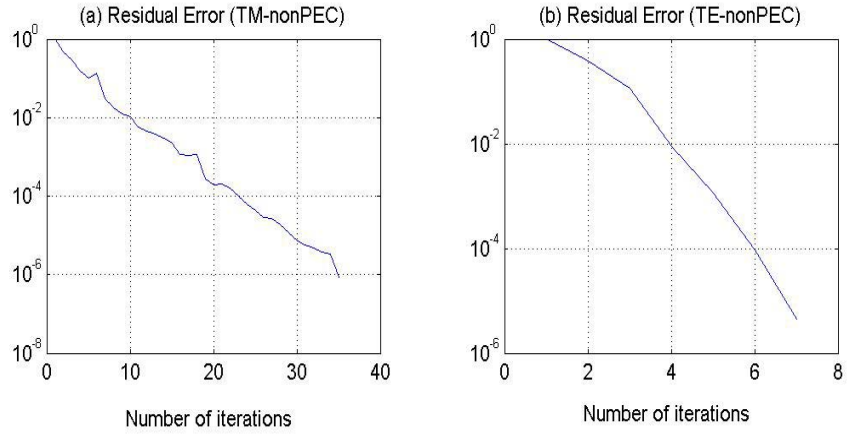

Figure 3.9 Residual errors of Figure 3.8

The third example is again a 100λ width rough surface illuminated by a isotropic radiator placed at 25λ above at the left most point of the terrain. The radiated power is assumed to be 25 Watts. Both cases for TM and TE polarization are plotted for perfect conducting surface.

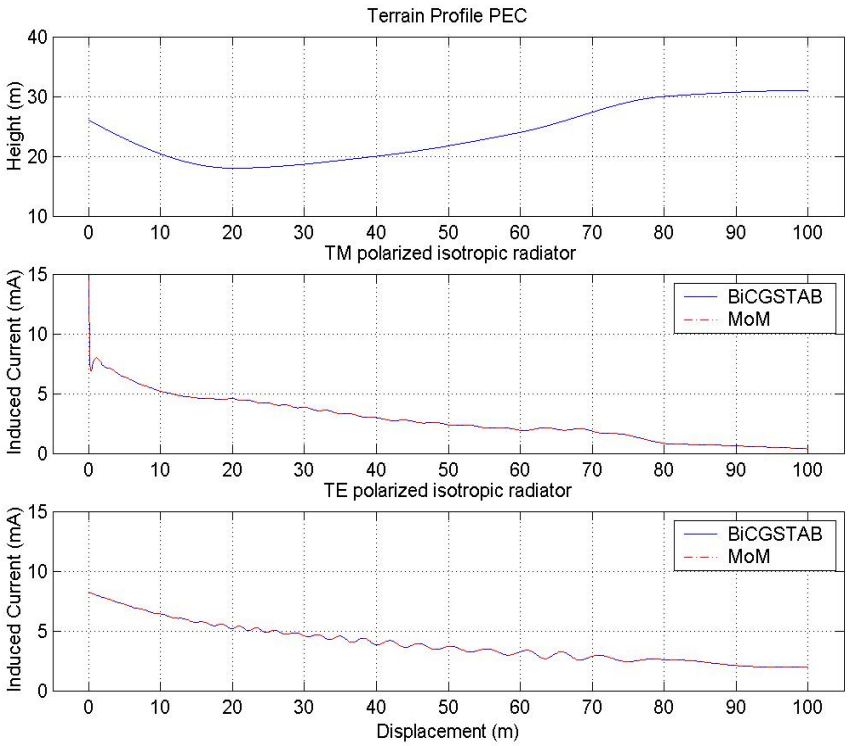

Figure 3.10 Isotropic radiator on the rough surface

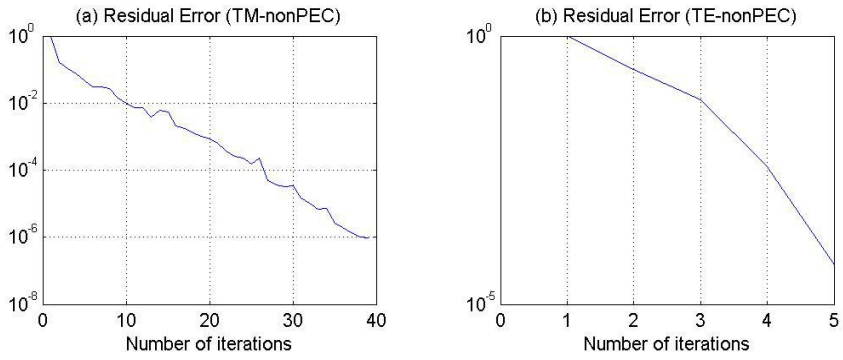

Figure 3.11 Residual errors of Figure 3.10

The currents for both polarization cases decay to zero. This is normal for an isotropic source that the field strength is inversely proportional to the distance taken.

Figure 3.12 displays a rough surface of width 200λ. The results are again compared with MoM solution for validity. An infinitesimal dipole is placed above height 25λ at the center of the terrain. The surface impedance is given as $\eta_s = 17.6 + j16.8$. The radiated power is 25 Watts.

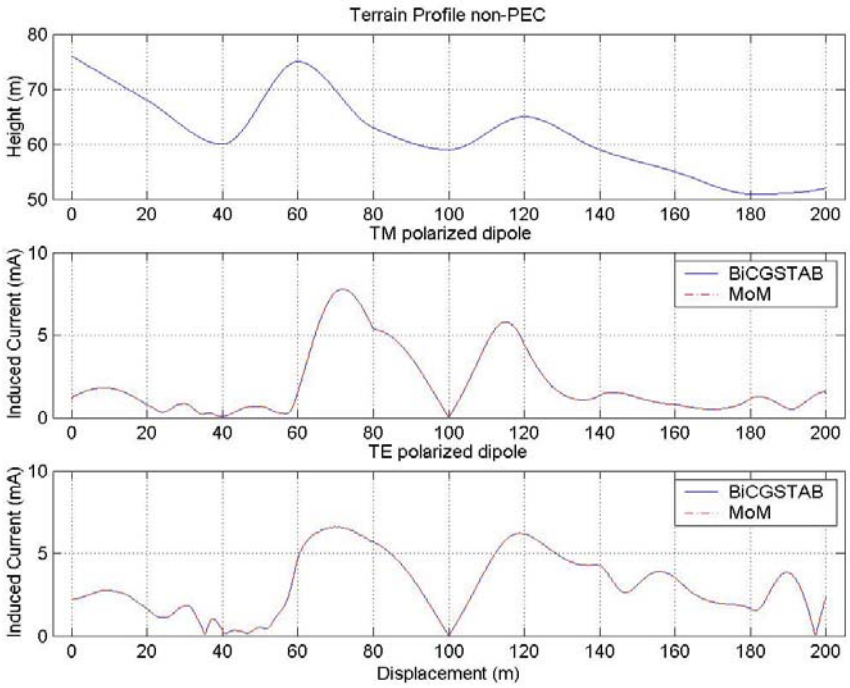

Figure 3.12 Dipole antenna on the rough surface

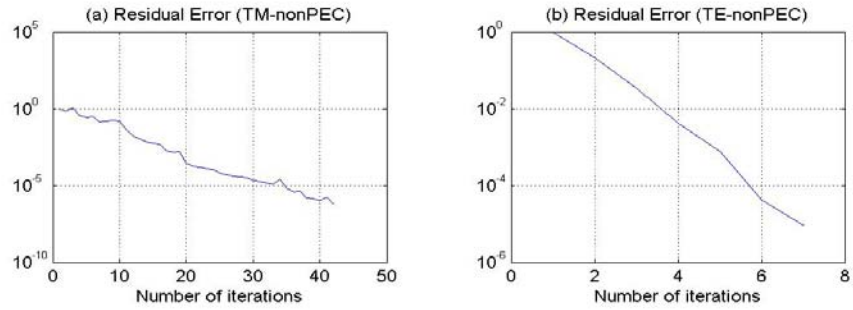

Figure 3.13 Residual errors of Figure 3.12

Because of the hill geometry, the current suddenly decreases between 20 and 80 meters. This is the shadowing effect of the peak of the terrain preceding to where the dipole is located. The left lobe of the current is higher than the right one due to θ_n deviation. The residual error rates with respect to the number of iterations are given in Figure 3.13 for both polarization cases.

Figure 3.14 is another surface profile of width 200λ. Imperfect conducting case is considered with $\eta_s = 17.6 + j16.8$. Dipole antenna is located at the 40^{th} meters on the displacement axis above 25λ of the surface. Average radiated power is now 40 Watts. The shadowing effects are clearly seen on the surface.

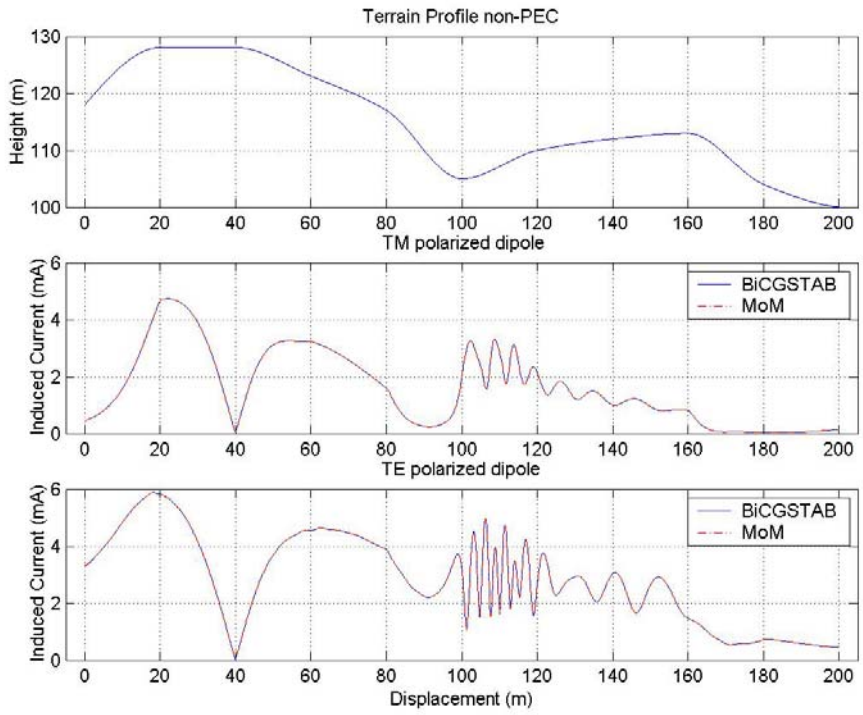

Figure 3.14 Dipole antenna on the rough surface

N = 2000 is the upper limit for us to use MoM as a reference due to RAM requirement of the computer. Also the operation count of $O(N^3)$ to employ LU decomposition to invert the MoM matrix makes the process really

cumbersome after this number of unknowns. The numerical examples show that BiCGSTAB method is well suited for scattering problems. By applying this method, the operation count is reduced to $O(N^2)$. So BiCGSTAB method can be used as a reference solution for the analysis of the terrain profile. One other advantage is that the storage requirement can be kept at $O(N)$ at the cost of reevaluating each of the matrix entries at every iteration.

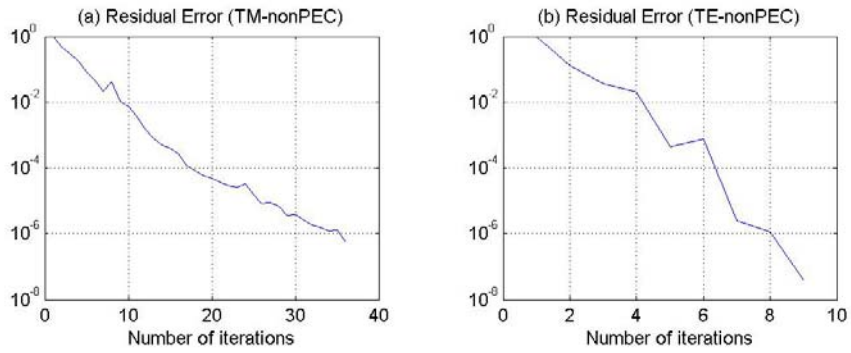

Figure 3.15 Residual errors of Figure 3.14

The next example is an unordered surface profile. The target under test is a ship placed on a 400 meters sea surface. To generate random sea surface for a given wind speed, an infinite-depth Pierson-Moskowitz ocean spectrum [28] is used. Both PEC and imperfect conducting cases are considered. As we mentioned before since the surface of the scatter is multi-valued, stationary methods such as FBM can not solve this kind of problem. In order to show the validity of the BiCGSTAB the results are compared with generalized forward-backward method (GFBM). To cope with divergence in a multi valued region, Pino *et all.* [21] have introduced a generalized version of this method. The method is based on same general concepts stated for FBM but includes significant changes in the decomposition of system interaction matrix. This decomposition is complicated fact for large-scale problems. This fact comes from dividing the surface area into three regions. The first and the last regions are reserved to single valued surface geometry and solved via conventional FBM. The second one called MoM region includes the reentrant surface

elements (i.e., ship) where the number of elements is given as N_{MoM} and solved by matrix vector production approximation. The computational cost is $O(N_{MoM}^2)$. Thus this approach requires an additional work and more storage requirement at each iteration, which can be very overwhelming if the multi-valued section is too large. As a conclusion, the rapid convergence of FBM looses its attraction. Figure 3.16 displays the height and width properties of the ship under target with respect to λ. Frequency is 300MHz with number of unknowns $N = 4500$.

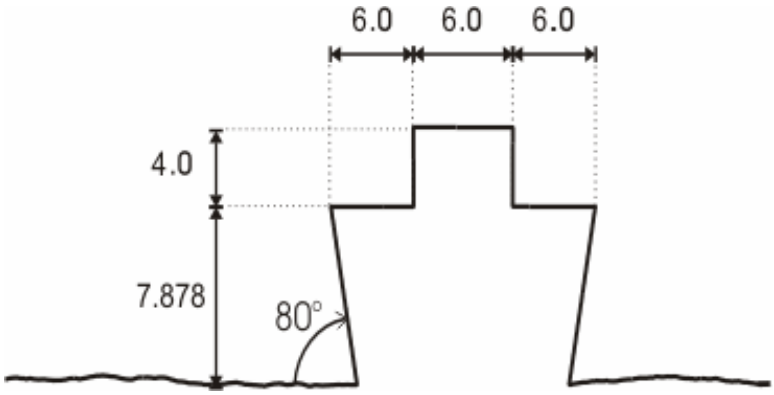

Figure 3.16 The ship under target

The results are evaluated for TM polarization both for PEC and non-PEC case. For the imperfect conducting case, the sea is modeled with a surface impedance $\eta_s = 76.4 + j65.1$ while the ship remains PEC. Plane wave incidence is considered with an angle $\theta = \pi / 36$. Current distributions on the surface of the sea and the ship due to 0 m/s (flat surface), 5m/s and 10m/s wind speed are plotted in Figure 3.17, Figure 3.18 and Figure 3.19, respectively.

The results show that BiCGSTAB method yield accurate results without cumbersome operations like sectioning the area of target like GFBM does and storing the impedance matrix in the ship region. Nevertheless, since the off-diagonal elements of interaction matrix are large owing to the multi-valued ordering at the ship surface, the number of iterations is increased to obtain a

residual error of 10^{-3}. Figure 3.20 shows the error rates for perfect conductivity condition.

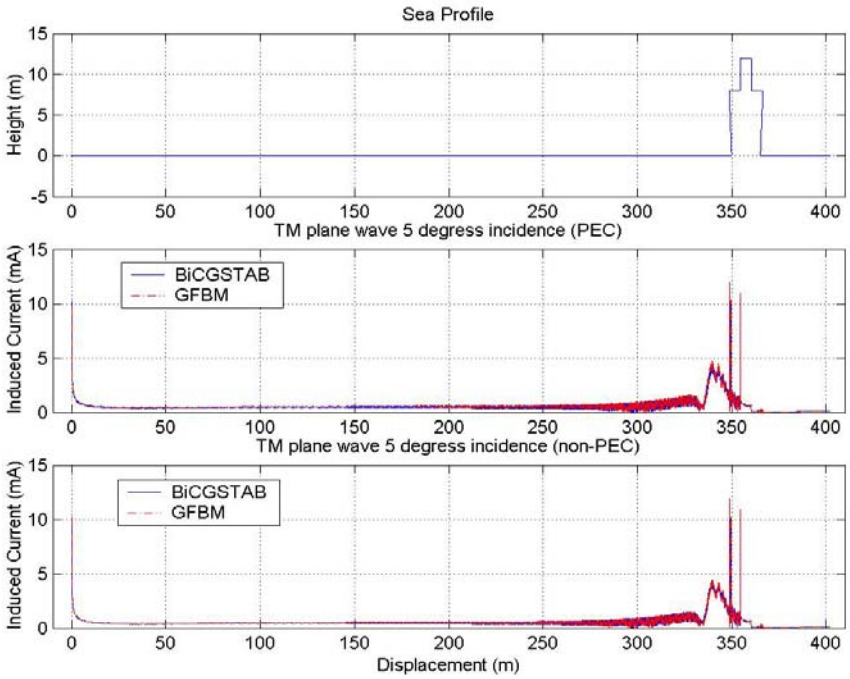

Figure 3.17 Current distribution on a ship (wind speed: 0m/s)

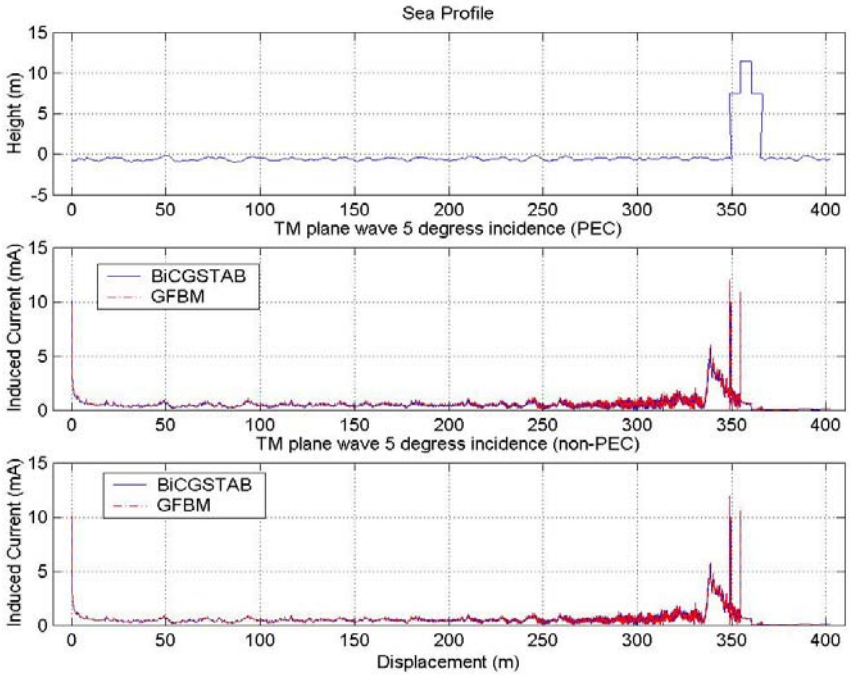

Figure 3.18 Current distribution on a ship (wind speed: 5m/s)

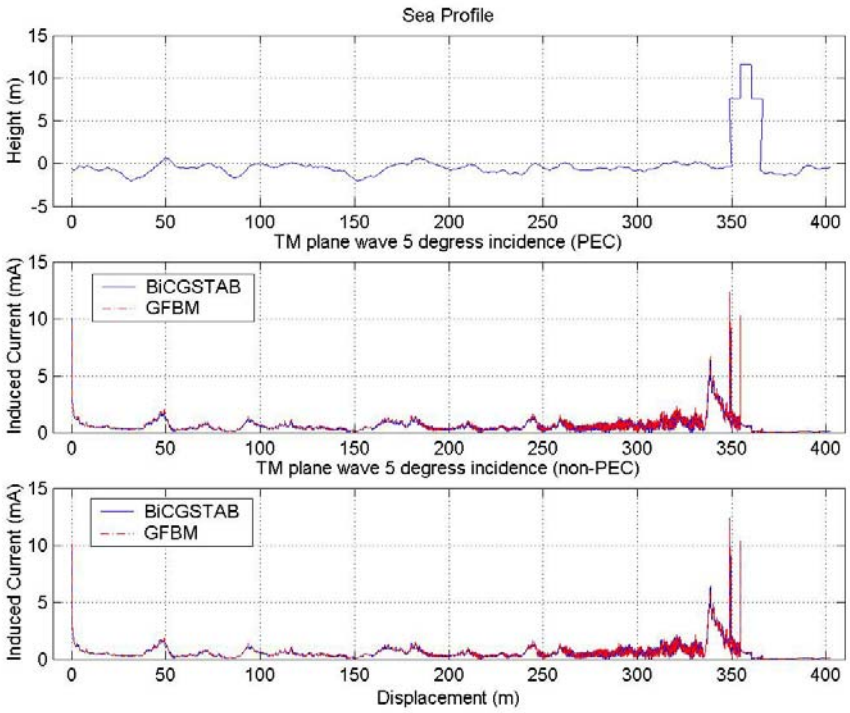

Figure 3.19 Current distribution on a ship (wind speed: 10m/s)

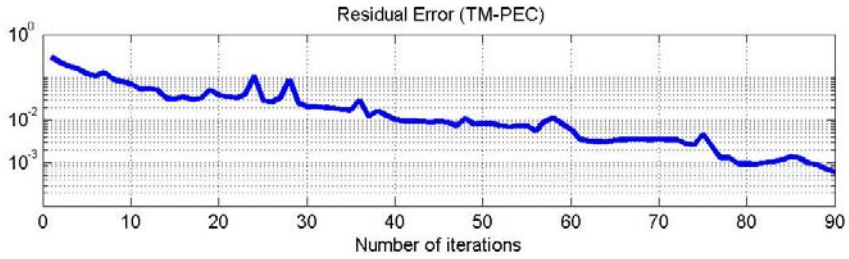

Figure 3.20 Residual error for PEC case

And in Figure 3.21, residual error is plotted for imperfect conductor case.

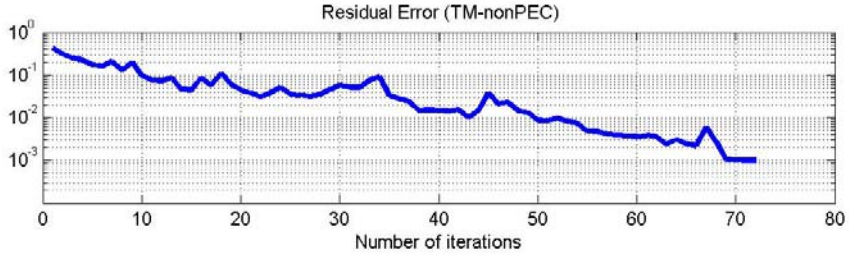

Figure 3.21 Residual error for non-PEC case

It's clearly seen the residual error rates deceases slowly due to the reentrant surface of the ship. While iteration number for the PEC case is about 90 for three different wind speeds, this number is reduced to about 70 for imperfect conductor surface because of having better conditioning of impedance matrices.

3.3.3 Computational Cost of BiCGSTAB

Investigations on rough surface profiles show that BiCGSTAB obtains numerically accurate results for both TM and TE polarization cases. BiCGSTAB reaches a residual error of 10^{-3} about 25 iterations for TM case and about 10 iterations for TE case (reentrant surfaces are exceptions). But it's better not to define exact number to reach to desired level of error because, as stated earlier, the number of iterations is strongly dependent upon the number of unknowns to be solved. While MoM's computational cost is related to the matrix fill time and LU inversion, BiCGSTAB has a computational cost due to matrix-vector multiplication and number of iterations. Table 3.3 shows this relation on the assumption that BiCGSTAB reaches residual error of 10^{-3}. Since the data is not available for the MoM solution, Cpu-time values for matrix filling time found by using spline extrapolation after 2000 unknowns.

N	**Mat-Fill (s)**	**LU inversion (s)**	**TM-BiSTAB (s)**	**TE-BiSTAB (s)**
500	1.5	55	9.5	2
1000	5.5	542	41.5	9
2000	25.5	5018.5	199	70
5000	172	NA	1312.5	360
10000	600	NA	5057	1281
20000	2417	NA	48232	5372

Table 3.3 Computational cost for BiCGSTAB method

From the table above, it is obvious that MoM requires $O(N^3)$ cpu-time while the BİCGSTAB requires $O(N^2)$ computational cost. The computational cost with respect to unknowns is plotted in Figure 3.22.

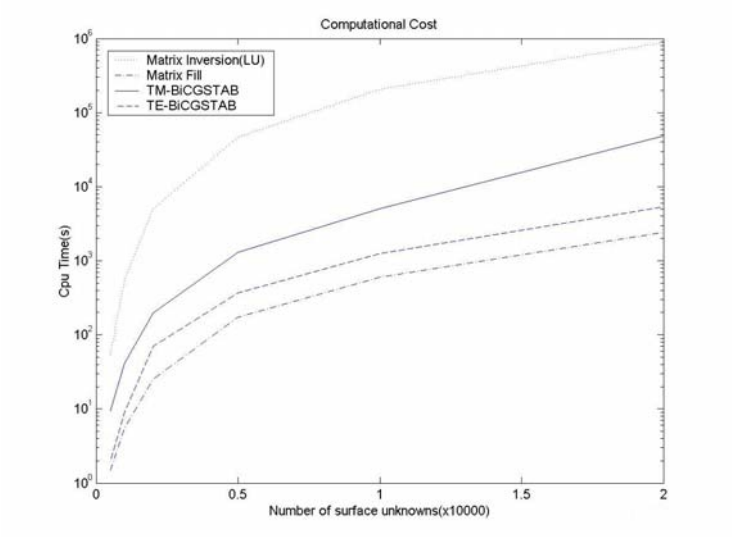

Figure 3.22 Computational Cost

The examinations and comparisons demonstrate that, the BiCGSTAB can be used as a reference solution instead of MoM for the study of scattering problems for both horizontal and vertical polarizations with a computational cost of $O(N^2)$.

3.4 Spectral Acceleration Algorithm

As mentioned before, BiCG and BiCGSTAB require two matrix- vector multiplies at each iteration which means $O(N^2)$ operations per iteration. These methods provide accurate results and presents fast convergence. Nevertheless, for very large N (i.e., when the problem of interest is electrically large such as terrain profiles in the rural areas), the operation count per iteration increases drastically such that the use of method becomes inefficient. Keeping the impedance matrix, found by employing MoM solution, raises storage requirements. At a certain dimension of the problem, storing interaction matrix

becomes unfeasible. However, in 1996, *Chou and Johnson* [18] have come up with an alternative scheme. They have proposed an acceleration algorithm named spectral acceleration (SA) for faster computation of the interactions between widely separated points. SA was utilized firstly for the original forward-backward method and they have proved that this approach results in a solution with an operation count of *O(N)*. The algorithm is mainly based on a spectral domain representation of two-dimensional Green's function which is applicable to both for PEC and imperfect conducting cases. In SA, there is no need to store the impedance matrix at the cost of reevaluating only a very small portion of elements interaction. Therefore storage requirement is decreased significantly. Although SA algorithm is well suited for FBM that it precedes the forward and backward sweeps of the propagating fields, it can also be used in any standard iterative processes like BiCG or BiCGSTAB methods. *Valero* [29] utilized the SA algorithm in conjunction with BiCG firstly in order to make fast analysis of electromagnetic scattering from the strip gratings. However, analyzing electrically large terrain profiles has never been examined in the literature.

3.4.1 SA Algorithm for Quasi-planar Surfaces

In SA, radiating elements over a given receiving element are divided into two groups. The first one is the *forward propagating field* via preceding source elements and the second one is *backward propagating field* via the following source elements with respect to *n*th receiving point as illustrated in Figure 3.23 for a flat surface for the *n*th receiving element.

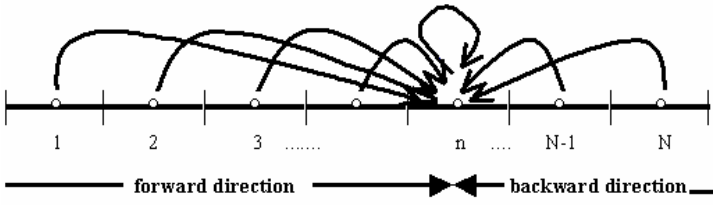

Figure 3.23 Forward and backward propagating fields on a flat surface

The forward propagating field is also divided into two groups: *strong interaction group* and *weak interaction group*. The decisive factor defining these groups is the distance from the receiving element. Hence for a distance L_s, the strong group contains $N_s = L_s / \Delta x$ (Δx is the unit pulse width) elements including the interaction of its self, and the rest of the source elements construct the weak group (Figure 3.24). Thus, the total field in the forward direction will be the sum of strong and weak group contributions. The same assumption holds for the backward propagation.

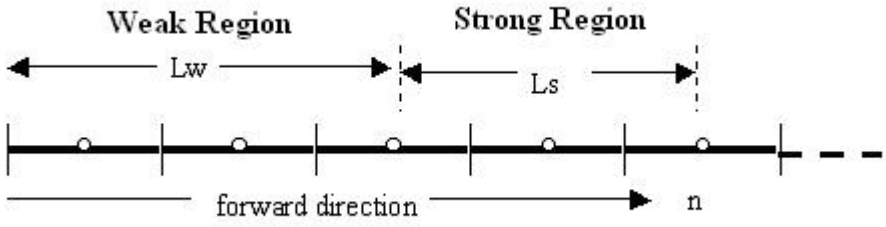

Figure 3.24 Weak and strong regions for the *n*th receiving point at forward direction

3.4.1.1 Spectral Acceleration for Horizontal Polarization

The algorithm procedure for the electric field integral equation for the TM polarization is given below. As mentioned, the fields are divided into two groups; the electric field formed by forward propagating field denoted as E_f and the one formed by backward propagating field denoted as E_b. As stated earlier, SA algorithm was originally derived for the FBM. FBM assumes that the lower triangular interaction matrix and the unknown current coefficient vector product create the forward propagating field. So the backward propagating field is left to be the multiplication of upper triangular interaction matrix with the unknown current coefficient vector. Due to this consideration, forward field can be illustrated as,

$$E_f(\boldsymbol{\rho}_n) \;=\; \overline{\mathbf{Z}}^f . \mathbf{I} \;=\; \sum_{m\,=\,1}^{N} I_m Z_{nm} \;. \tag{3.27}$$

At the forward propagating field expression in (3.27), superscript *f* at the top of the impedance matrix denotes the sum of lower triangular and diagonal parts of the matrix. In fact, when SA is used for the FBM, the diagonal part is excluded from the algorithm (i.e., the upper summation limit at the right hand side of (3.27) is *n-1*). This is the main difference between accelerated versions of the FBM and the conjugate gradient type methods. The backward propagating field can be expressed as

$$E_b(\boldsymbol{\rho}_n) \;=\; \overline{\mathbf{Z}}^b . \mathbf{I} \;=\; \sum_{m\,=\,n+1}^{N} I_m Z_{nm} \;. \tag{3.28}$$

Similar to the forward propagation case, superscript *b* at the top of the impedance matrix denotes the upper triangular part. For simplicity, only the forward propagating field will be focused in here, the backward part can be treated in the same manner and is given in appendices.

The forward field is also divided into two groups; the contributions coming from the strong region and the contributions due to weak region, i.e.,

$$\overline{\mathbf{Z}}^f . \mathbf{I} \;=\; E_f(\boldsymbol{\rho}_n) \;=\; E_{f,w}(\boldsymbol{\rho}_n) \;+\; E_{f,s}(\boldsymbol{\rho}_n) \tag{3.29}$$

where the strong and weak contributions can be written as

$$E_{f,s}(\boldsymbol{\rho}_n) \;=\; \sum_{m\,=\,n-N_s+1}^{N} I_m Z_{nm} \tag{3.30}$$

$$E_{f,w}(\boldsymbol{\rho}_n) \;=\; \sum_{m\,=\,1}^{n-N_s} I_m Z_{nm} \tag{3.31}$$

with the impedance matrix elements defined in (2.48). The radiations of the strong group contributions are found in the conventional matrix-vector multiplication by evaluating the exact impedance elements. However, weak group contribution is obtained by employing spectral representation of the two-dimensional Green's function.

$$G(\rho_n, \rho_m) = \frac{-j}{4\pi} \int_{C_\phi} e^{-jk[(x_n - x_m)\cos\phi + (z_n - z_m)\sin\phi]} d\phi \tag{3.32}$$

where C_ϕ is the contour of integration in the complex ϕ space shown in Figure 3.25. We also need the derivative of the Green's function due to normal vector at the source point, which takes place within the off-diagonal entries of the impedance matrix defined in (2.49)

$$\frac{\partial G(\rho_n, \rho_m)}{\partial n_m} = \frac{k}{4\pi} \int_{C_\phi} \left[\cos\theta_m \cos\phi + \sin\theta_m \sin\phi\right] . e^{-jk[(x_n - x_m)\cos\phi + (z_n - z_m)\sin\phi]} d\phi \tag{3.33}$$

where θ_m is the angle between the normal vector at the source point $\hat{n}_m$ and the unit vector $\hat{x}$.

Substituting equations (3.32) and (3.33) into (3.31) and interchanging the summation and integration gives,

$$E_{f,w}(\boldsymbol{\rho}_n) = -\frac{\omega\mu}{4\pi} \int_{C_\phi} F_n(\phi) e^{-jk(z_n \sin\phi)} d\phi \tag{3.34}$$

where

$$F_n(\phi) = \sum_{m=1}^{n-N_s} I_m \Delta x_m \left\{1 - \frac{\eta_m}{\eta_0}[\cos\theta_m \cos\phi + \sin\theta_m \sin\phi]\right\} . e^{-jk\left[(x_n - x_m)\cos\phi - z_m \sin\phi\right]} \tag{3.35}$$

The integrand $F_n(\phi)$ can be represented via recursive formulation:

$$F_n(\phi) = F_{n-1}(\phi) e^{-jk(x_n - x_{n-1})\cos\phi} + I_{ns} \Delta x_{ns} \left\{1 - \frac{\eta_{ns}}{\eta_0}[\cos\theta_{ns} \cos\phi + \sin\theta_{ns} \sin\phi]\right\} . e^{-jk\left[(x_n - x_{ns})\cos\phi - z_{ns} \sin\phi\right]} \tag{3.36}$$

with $F_n(\phi) = 0$ for $n \le N_s$. The subscript *ns* is equal to *n* - N_s. By employing this recursive procedure a great reduction of computational cost is obtained. Due to this formula, the integrand of *n*th element updates itself in terms of the

previous one, which keeps all of the weak interactions until that receiving element. Hence, operation count required for the weak region process is *O(N)*. An analogous procedure can also be implemented for the backward case and is given in Appendix A.I.

3.4.1.2 Spectral Acceleration for Vertical Polarization

If we use MFIE formulation for TE polarization, the forward propagating magnetic field, is the sum of strong and weak contributions,

$$H_f(\boldsymbol{\rho}_n) = H_{f,w}(\boldsymbol{\rho}_n) + H_{f,s}(\boldsymbol{\rho}_n) \tag{3.37}$$

with

$$H_{f,s}(\boldsymbol{\rho}_n) = \sum_{m=n-N_s+1}^{n} I_m Z_{nm} \tag{3.38}$$

and

$$H_{f,w}(\boldsymbol{\rho}_n) = \sum_{m=1}^{n-N_s} I_m Z_{nm} \tag{3.39}$$

where the elements of the impedance matrix are defined in (2.52). The radiations of the strong group contributions are found in the conventional matrix-vector multiplication by evaluating the exact impedance elements. However, weak group contribution is obtained by employing spectral representation of the two-dimensional Green's function. Than by using (3.32) and (3.33), the forward propagating magnetic field is given by

$$H_{f,s}(\boldsymbol{\rho}_n) = -\frac{\mathrm{k}}{4\pi}\int_{C_\phi} F_n(\phi) e^{-jk(z_n \sin\phi)} d\phi \ , \tag{3.40}$$

where

$$F_n(\phi) = \sum_{m=1}^{n-N_s} I_m \Delta x_m \left\{ \cos\theta_m \cos\phi + \sin\theta_m \sin\phi - \frac{\eta_m}{\eta_0} \right\} \cdot e^{-jk\left[(x_n - x_m)\cos\phi - z_m \sin\phi\right]} \cdot \tag{3.41}$$

The integrand $F_n(\phi)$ can be evaluated via a recursive formulation given by

$$F_n(\phi) = F_{n-1}(\phi)e^{-jk(x_n - x_{n-1})\cos\phi} + I_{ns}\Delta x_{ns}\left\{\cos\theta_{ns}\cos\phi + \sin\theta_{ns}\sin\phi - \frac{\eta_m}{\eta_0}\right\} \cdot e^{-jk\left[(x_n - x_{ns})\cos\phi - z_{ns}\sin\phi\right]} \tag{3.42}$$

with $F_n(\phi) = 0$ for $n \le N_s$. The subscript *ns* is equal to $n - N_s$. By applying this recursive process on the integrand, we again provide an operation count of *O(N)*. As a result, an equivalent procedure can be applied for the backward propagating field, which is divided also into two groups, strong and weak interactions and is given in Appendix A.II.

.

3.4.1.3 Integration Contour for Quasi-planar Surfaces

Since the Hankel function is analytic in the complex angular plane for widely separated points, the integration path can be deformed to a steepest descent path (SDP). The SDP of a flat surface (i.e., $z_n - z_m = 0$) passing through the origin is shown in Figure 3.25 as SDP_0. Due to asymptotic analysis, it is seen that most of the contribution of the integrand occurs on the SDP near a saddle point located on the real axis. As the distance increases from the saddle point along the SDP, the complex values on this path make the integrand in (3.34) and (3.40) decrease exponentially, hence, the contributions become negligible. Since the significant contributing region is much smaller than the original path C_ϕ, the deformation process is very advantageous numerically. This smaller integration path also reduces rapid oscillations of the integrand in (3.34) and (3.40) which would cause numerical instabilities due to limited precision of the computer. It is obvious that multi steepest descent paths occur for rough surfaces. In this case, each pair of source point (located at $\boldsymbol{\rho_m}$) and the observation point (located at $\boldsymbol{\rho_n}$), constructs a saddle point located on the real axis of the complex angular plane. Saddle points are given as,

$$\phi_{nm} = \tan^{-1}\left(\frac{z_n - z_m}{x_n - x_m}\right). \tag{3.43}$$

As seen in Figure 3.25, the complex space is divided into regions to be related in the spatial domain. Regions, where significant contributions due to saddle points on the real axis take place, are lit regions (A and B). The lit region is similar to the geometric optic (GO) region defined in uniform theory of diffraction (UTD) [30] as shown in Figure 3.26. The width of the lit region depends on saddle points' distribution. The parts of the real axis outside the lit region are denoted as shadow regions (C and D). The contributions coming from shadow regions are weak compared to those of lit regions.

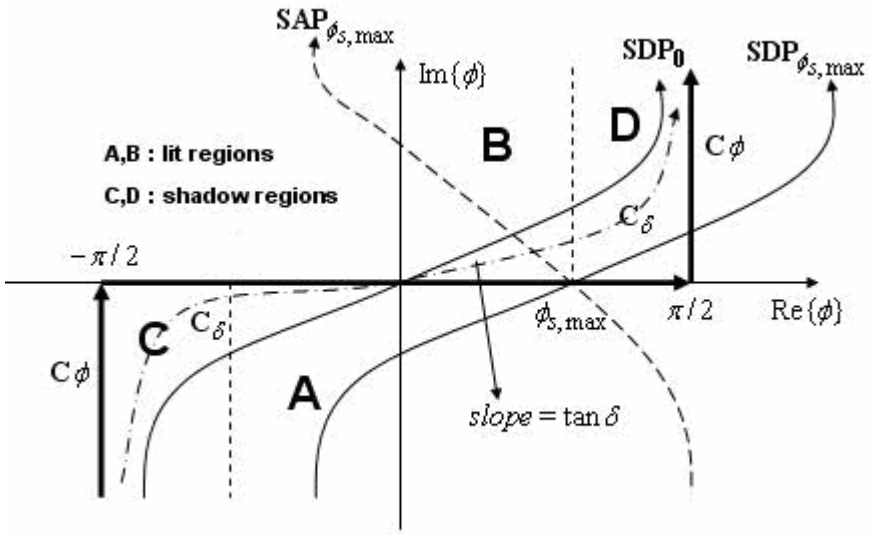

Figure 3.25 Integration paths of Hankel function

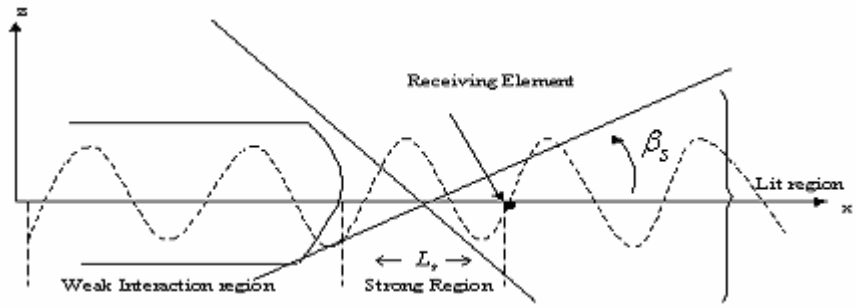

Figure 3.26 Geometric interpretation of asymptotic lit region

For rough geometries, since the lit regions A and B consist of many saddle points, there is no longer a unique SDP along which the attenuation of the integrand is obtained via a single saddle point. Also the shadow regions, C and D, will be combined with both SDP and steepest ascent paths (SAP) of the saddle points where the integrand at these regions may increase exponentially for large height deviations (i.e, the lit region is enlarged). This effect is illustrated in Figure 3.27 showing the behavior of the integrand along the SDP of a flat surface for different height (dz) and displacement (dx) deviations.

In order to avoid numerical instabilities caused by the integrand, it is advantageous to choose an L_s such that the lit region remains small and to deform the contour of integration C_ϕ to a shorter path C_δ. C_δ is defined to be a straight line with a slope *tanδ* through boundaries of regions A and B. $\delta = \pi / 4$ for a flat surface but it is chosen smaller to avoid extreme exponential growths in the regions C and D when undulating geometries are of interest. This choice of δ, maintains contributions outside the lit regions to be trivial.

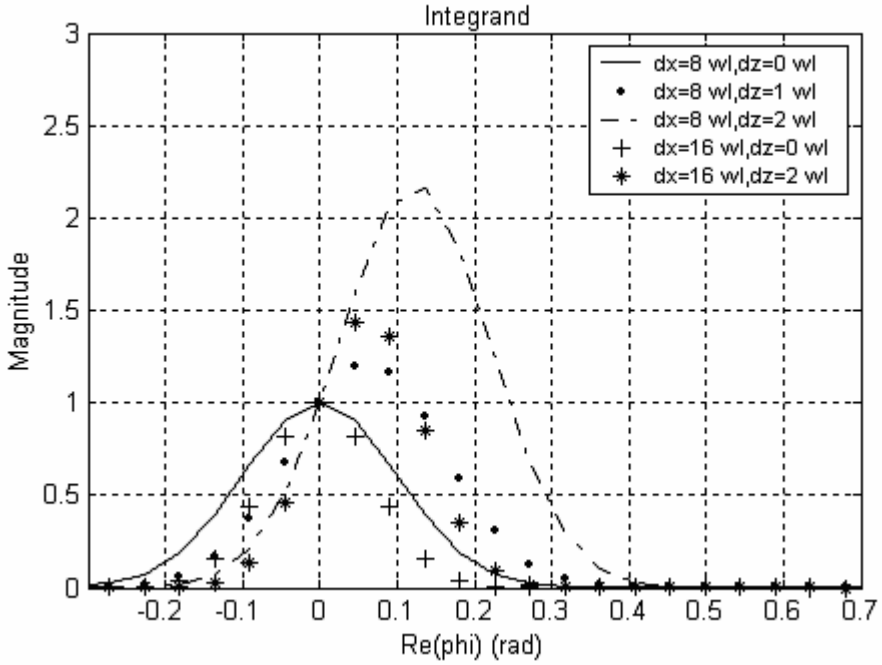

Figure 3.27 Integrand along the SDP of a flat surface

The value of δ for a quasi-planar surface is defined by limiting the maximum integrand value of the most critical point, which is the maximum saddle point defining the geometry. The integrand will have its maximum value on the deformed path C_δ at the point where the SAP through $\phi_{s,\max}$ crosses C_δ as shown in Figure 3.25. Through empirical tests, this maximum value is obtained as e^{20}. But for more rough surfaces smaller values can be used. By doing this δ can be approximately given as: [18]

$$\delta = \tan^{-1}(1/\mathrm{b}) \quad \mathrm{b} = \max\left[\sqrt{\frac{kR_{s,\max}}{20}}\phi_{s,\max} - 1\,,\,1\right] \tag{3.44}$$

with

$$R_{s,\max} = \sqrt{L_s^2 + (z_{\max} - z_{\min})^2} \tag{3.45}$$

and

$$\phi_{s,\max} = \tan^{-1}\left(\frac{z_{\max} - z_{\min}}{R_s}\right) \tag{3.46}$$

are used since $R_{s,max}$ is the largest distance between source and observation points for the outermost saddle point at the shadow boundary.

3.4.1.4 Integration Steps

The integrals of (3.34) and (3.40) can be discretized into $2Q+1$ plane wave directions (where $Q<<N$). It is worth to mention that Q is independent of the unknowns, N. Then the integration is mapped to real axis by

$$\Delta\phi \rightarrow \Delta\phi e^{j\delta} \tag{3.47}$$

with

$$\phi \rightarrow p\Delta\phi e^{j\delta}. \tag{3.48}$$

Exponentially decaying behavior of the integrand allows us to filter it. Thus, (3.34) and (3.40) can be illustrated as

$$E_{f,w}(\boldsymbol{\rho}_n) = -\frac{\omega\mu}{4\pi}\sum_{p=-Q}^{Q} W(\phi_p)F_n(\phi)e^{-jk(z_n\sin\phi)}\Delta\phi e^{j\delta}\,, \tag{3.49}$$

$$H_{f,w}(\boldsymbol{\rho}_n) = -\frac{k}{4\pi}\sum_{p=-Q}^{Q} W(\phi_p)F_n(\phi)e^{-jk(z_n\sin\phi)}\Delta\phi e^{j\delta}, \quad (3.50)$$

respectively. $W(\phi_p)$ is the windowing function defined as

$$W(\phi_p) = \begin{cases} 1 & |\phi_p| \le \beta_s \\ 0 & |\phi_p| > \beta_s \end{cases}. \quad (3.51)$$

Here, β_s is the geometrical optics lit region indicated in Figure (3.26). β_s is selected according to the maximum roughness of the surface. The pragmatic tests have shown that a value of $\beta_s = \sqrt{10/kL_s}$ with $L_s \ge (z_{max} - z_{min})/4$ yield accurate results. These choices are evaluated by examining SDP of quasi-planar surfaces and may not hold for very rough surfaces. Using the windowing effect due to β_s, reduces the number of plane waves and Q can be found as [18],

$$Q = \beta_s/\Delta\phi + 5 \quad (3.52)$$

with

$$\Delta\phi = \sqrt{5/(\mathrm{kR}_s)}/22\,. \quad (3.53)$$

As a result, an equivalent procedure can be applied for the backward propagating field

3.4.1.5 Operation Count for SA Algorithm for Quasi-planar Surfaces

As we proposed before, the total operation count to determine the matrix-vector products in the gradient types of the iterative techniques is reduced to *O(N)*.If we look at the forward propagating field evaluation, the number of operations involved in the computation of strong contribution for N receiving elements are NxN_s ($N_s << N$). The operation count to compute $2Q$+1 plane waves in (3.36) and (3.42) is 4(2Q+1)x(*(N-*N_s*)* for each plane wave and

the operation count to evaluate the weak propagating field is 2(2Q+1)x(*(N-N_s)*. As a result, the total operation count is:

$$N\text{x}N_s \; + \; (N - N_s)\text{x}6(2Q+1) \; \rightarrow \; O(N) \qquad (3.54)$$

It is noted that N_s is a constant and the number Q does not depend on the size N. That is why, (3.54) is valid when N increases. The total memory storage is estimated as 3N vectors for the total, forward and backward fields and (2Q+1) plane waves.

3.4.2 SA Algorithm for Rough Surfaces

The method proposed by [18] is a very effective technique giving very accurate results when dealing with quasi-planar surfaces (like ocean-waves). However, when the surface becomes very undulating (i.e. terrain profiles in nature are considered), the SA developed by [18] yields inaccurate results. To overcome this problem Lopez *et all* . [19] proposed a modified version of this acceleration algorithm. These are trivial modifications applied to parameters of complex integral contour C_δ for the correction of integrand values. The critical point of this algorithm, different than the original SA algorithm is to introduce the term $e^{-jkz_n \sin\phi}$ into the equations (3.34) and (3.40). Because this term itself, would cause numerical difficulties considering the dimensions of the terrain profiles in the rural areas. In the meantime, when it is put inside (3.34) and (3.40) and recursive relations are derived, the expressions related to the height deviation usually presents less numerical instabilities. The modified SA algorithm in here will be performed for both EFIE for TM polarization and MFIE for TE polarization cases.

3.4.2.1 Spectral Acceleration for Horizontal Polarization

As we stated earlier, SA presumes that the forward propagating field at the nth receiving element is the sum of contributions coming from two groups

$$E_f(\boldsymbol{\rho}_n) \;=\; E_{f,w}(\boldsymbol{\rho}_n) \;+\; E_{f,s}(\boldsymbol{\rho}_n) \tag{3.55}$$

where

$$E_{f,s}(\boldsymbol{\rho}_n) \;=\; \sum_{m\,=\,n-N_s+1}^{n} I_m Z_{nm} \tag{3.56}$$

named as forward strong field due to contributions in the vicinity of N_s elements through the receiving point including itself. And the second group is denoted as forward weak field and expressed as

$$E_{f,w}(\boldsymbol{\rho}_n) \;=\; \sum_{m\,=1}^{n-N_s} I_m Z_{nm} \tag{3.57}$$

due to weak contributions between widely separated points. The strong field is evaluated directly through conventional matrix-vector products where the elements of the impedance matrix given in (2.48) is evalutaed directly, and the weak interactions are computed by spectral representation of Green's funciton. By introducing (3.32) and (3.33) into (3.57) the forward weak field will is expressed as

$$E_{f,w}(\boldsymbol{\rho}_n) \;=\; -\frac{\omega\mu}{4\pi}\int_{C_\phi} F_n(\phi)\,d\phi \;, \tag{3.58}$$

where

$$F_n(\phi) \;=\; \sum_{m\,=\,1}^{n-N_s} I_m \Delta x_m \left\{1-\frac{\eta_m}{\eta_0}[\cos\theta_m\cos\phi \;+\; \sin\theta_m\sin\phi]\right\} \cdot e^{-jk\left[(x_n\,-x_m)\cos\phi\,-(z_n-z_m)\sin\phi\right]} \cdot \tag{3.59}$$

The integrand $F_n(\phi)$ can be represented via recursive formulation:

$$\begin{aligned} F_n(\phi) = F_{n-1}(\phi)e^{-jk[(x_n-x_{\text{n-1}})\cos\phi+(z_n-z_{n-1})\sin\phi]} \\ + I_{ns}\Delta x_{ns}\left\{1-\frac{\eta_{ns}}{\eta_0}[\cos\theta_{ns}\cos\phi+\sin\theta_{ns}\sin\phi]\right\} \\ \cdot e^{-jk\left[(x_n\,-x_{\text{ns}})\cos\phi-(z_n-z_{ns})\sin\phi\right]} \end{aligned} \tag{3.60}$$

with $F_n(\phi) = 0$ for $n \le N_s$. The subscript *ns* is equal to $n - N_s$. In (3.60), the term $e^{-jk(z_n - z_{ns})\sin\phi}$ presents less numerical instability as mentioned before. An equivalent procedure can be applied for the backward propagating field as given in Appendix B.I.

3.4.2.2 Spectral Acceleration for Vertical Polarization

If we use MFIE formulation for the vertical polarization case, the forward propagating magnetic field will be the sum of strong and weak group contributions, namely.

$$H_f(\boldsymbol{\rho}_n) \;=\; H_{f,w}(\boldsymbol{\rho}_n) \;+\; H_{f,s}(\boldsymbol{\rho}_n) \tag{3.61}$$

with

$$H_{f,s}(\boldsymbol{\rho}_n) \;=\; \sum_{m\,=\,n-N_s+1}^{n} I_m Z_{nm} \tag{3.62}$$

and

$$H_{f,w}(\boldsymbol{\rho}_n) \;=\; \sum_{m\,=1}^{n-N_S} I_m Z_{nm} \tag{3.63}$$

The strong field is evaluated directly through conventional matrix-vector products where the elements of the impedance matrix given in (2.52) are evaluated directly. By substituting (3.32) and (3.33) into (3.63), the contribution of the weak field can be expressed as

$$H_{f,w}(\boldsymbol{\rho}_n) \;=\; -\frac{k}{4\pi}\int_{C_\phi} F_n(\phi)\,d\phi \;, \tag{3.64}$$

where

$$F_n(\phi) \;=\; \sum_{m\,=\,1}^{n-N_s} I_m \Delta x_m \left\{ \cos\theta_m \cos\phi \;+\; \sin\theta_m \sin\phi \;-\; \frac{\eta_m}{\eta_0} \right\} \cdot e^{-jk\left[(x_n - x_m)\cos\phi \,-\, (z_n - z_m)\sin\phi\right]} \tag{3.65}$$

The integrand $F_n(\phi)$ can be represented via a recursive formulation

$$F_n(\phi) = F_{n-1}(\phi)e^{-jk[(x_n - x_{n-1})\cos\phi + (z_n - z_{n-1})\sin\phi]} + I_{ns}\Delta x_{ns}\left\{\cos\theta_{ns}\cos\phi + \sin\theta_{ns}\sin\phi - \frac{\eta_{ns}}{\eta_0}\right\} \cdot e^{-jk\left[(x_n - x_{ns})\cos\phi - (z_n - z_{ns})\sin\phi\right]} \quad (3.66)$$

with $F_n(\phi) = 0$ for $n \le N_s$. The subscript *ns* is equal to *n* - N_s. In (3.66), the term $e^{-jk(z_n - z_{ns})\sin\phi}$ presents less numerical instability as mentioned before. The backward propagating field can be found by splitting the magnetic field also into two groups; strong and weak contributions as given in Appendix B.II.

Once the integrands are determined, it is necessary to form the integration path along which the numerical integration will take place. The parameters used for recognition of the integration path will be defined next.

3.4.2.3 Integration Path for Rough Surfaces

Since the Hankel function is analytic for widely separated points in the complex angular domain, the integral contour C_ϕ can be deformed into a path C_δ as shown in Figure 3.28 along which the integrands in (3.58) and (3.64) decays rapidly . This path is chosen to reduce to computational cost needed to evaluate the integral and to avoid numerical instabilities (possible exponential growths of the integrand, which may be very oscillatory along the real axis).

As can be seen in Figure 3.28, the path related to C_δ is composed by three stretches. The numerical integral is performed along these stretches. The main one labeled as *C* usually gives accurate results. However, when more rough terrain geometries are of interest, two more stretches; the left one labeled as *L* and the right one labeled as *R*, can be included into the integration path.

Other parameters illustrated in Figure 3.28 for defining the integral path are explained below.

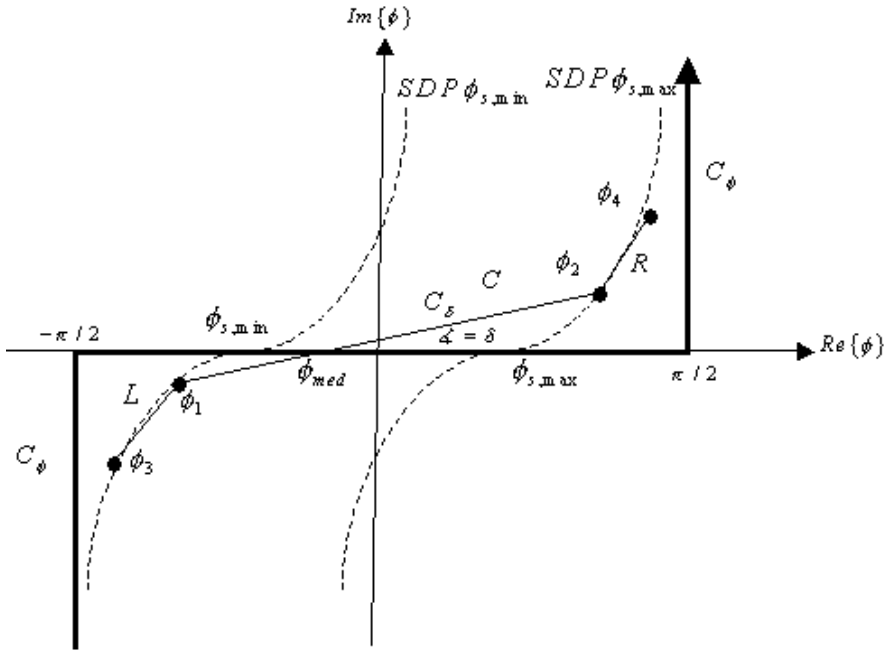

Figure 3.28 Integration path in the complex plane

Acquiring these parameters is based on the saddle point distribution in the complex ϕ plane. Each pair of source point (located at $\boldsymbol{\rho_m}$) and the observation point (located at $\boldsymbol{\rho_n}$) corresponds to a saddle point located given by

$$\phi_{nm} = \tan^{-1}\left(\frac{z_n - z_m}{x_n - x_m}\right) \tag{3.67}$$

where these saddle points are limited between the maximum and minimum slopes of the terrain (i.e., $\phi_{nm} \in \left[\phi_{s,min}, \phi_{s,max}\right]$).The saddle points are not distributed homogeneously along the real axis. For a downhill profile the saddle points are located on the negative real axis and for uphill profile, they are distributed on the positive real axis. ϕ_{med} gives a general idea of the terrain profile and it is evaluated as the medium value of other saddle points. The

integration path usually provides accurate results when ϕ_{med} is located at the middle of these three stretches.

In order to get a complete determination of the central stretch *C*, the inclination angle δ should be established. This is the angle between the real axis of the complex plane and *C*. The most critical saddle point defining the profile geometry determines the inclination angle. This is the point where the steepest ascent path (SAP) of the maximum saddle point crosses the central stretch. For a simple estimation we limit this contribution with e^2. This number has been found through some empirical tests as a most favorable value. Nevertheless, smaller values can be optimized for different terrain geometries. Referring to this choice, the inclination angle will be given as [19],

$$\tan\delta \leq \frac{1}{\sqrt{\frac{kR_s}{2}\left|\phi_{nm} - \phi_{med}\right|} - 1} \tag{3.68}$$

where R_s is defined as

$$R_s = \sqrt{(x_n - x_m)^2 + (z_n - z_m)^2}. \tag{3.69}$$

As stated in (3.68), the inclination angle can be given as an inequality expression. Thus, we have to find the minimum value of this expression to get the worst case. This means the computation of the maximum value of $\sqrt{R_s}\,|\phi_{nm} - \phi_{med}|$. The computation of this value for all pairs of source/ observation points require an operation count of $O(N^2)$, which is an undesired result for our purpose. That's why an approximation can be subjected via line segments to define the terrain profile. The length of these segments is proportional to the strong group length L_s. The endpoints of these segments can then be used to find the related saddle points. Consequently, the total amount operations will be lessened in order to compute the minimum value of inclination angle.

As shown in the Figure 3.28, the central stretch is bounded by the steepest descent path of the minimum saddle point $SDP\phi_{s,\min}$ at ϕ_1 and with the steepest descent path of the maximum saddle point $SDP\phi_{s,\max}$ at ϕ_2. The integrand $F_n(\phi)$ usually decays to zero at these limit points. However when more undulating geometries are of interest, the integrand may not reduce along the central stretch *C*. In this case, the contributions after points ϕ_1 and ϕ_2 should be included for the integration path. So, two more stretches, *L* and *R,* are attached at the end points of *C*. These added stretches coincide with the steepest descent paths therefore they can be approximated by straight lines making 45^o degrees with the real axis. By enlarging the integration path, our new limits are extended from ϕ_1 to ϕ_3 at the left hand side and from ϕ_2 to ϕ_4 at the right hand side shown in Figure 3.28. The integrand is assumed to fall at a reference value ζ at these end points. To find the exact values of ϕ_3 and ϕ_4, we compute where the integrand of $\phi_{s,\max}$ and $\phi_{s,\min}$ reaches the value of ζ. The imaginary parts of ϕ_3 and ϕ_4 are evaluated as [19]

$$\mathrm{Im}\{\phi_3\} = -\mathrm{Im}\{\phi_4\} = -\sqrt{\frac{-\ln\zeta}{kL_s}} \tag{3.70}$$

where **Im**{.} denotes the imaginary part of the complex number. In general, a value of $\zeta = \mathrm{e}^{-3}$ provides accurate results in the complex integration.

3.4.2.4 Integration Steps

After defining the integration path where the numerical integration takes place, we have to determine integration steps at each stretch. For the central stretch *C*, the integration step is defined as in [18],

$$\Delta\phi_C = \sqrt{5/(\mathrm{kR}_{\mathrm{s,max}})}/22 \tag{3.71}$$

where $R_{s.max}$, being related with the maximum height deviation and the strong contribution length, can be given as

$$R_{s,\max} = \sqrt{L_s^2 + (z_{\max} - z_{\min})^2} \tag{3.72}$$

This integration sampling rate can also be used for other two lateral stretches. Nevertheless, since the integrand values on the lateral stretches smoothly approach to zero when compared with highly oscillatory behaving at *C*, larger integration steps can be used. We now have to define new $R_{s.max}$ values due to most critical contributions at *L* and *R* stretches. For the lateral stretch *L*, the $R_{s,max}$ is associated with the maximum distance between source / observation point pairs which have the same $\phi_{s,\min}$ value. In the same manner for the lateral stretch *R*, $R_{s,max}$ is associated with the maximum distance between source/observation point pairs, which have the same $\phi_{s,\max}$ value. By substituting these maximum distance values, the new integration steps will be

$$\Delta\phi_L = \sqrt{5/(\mathrm{kR}_{\max,\phi_{s,min}})}/22 \tag{3.73}$$

for the left stretch *L*, and

$$\Delta\phi_R = \sqrt{5/(\mathrm{kR}_{\max,\phi_{s,max}})}/22 \tag{3.74}$$

for the right stretch *R*. Then the integration step is mapped to real axis of the complex domain via

$$\begin{aligned} \Delta\phi_C &\rightarrow \Delta\phi_C e^{j\delta} \\ \Delta\phi_L &\rightarrow \Delta\phi_L e^{j\pi/4} \\ \Delta\phi_R &\rightarrow \Delta\phi_R e^{j\pi/4} \ . \end{aligned} \tag{3.75}$$

As a conclusion, the weak field propagating in the forward direction for the n^{th} receiving element is obtained as:

$$T_{f,w}(\rho_n)\Big|_{T=E,H} = \sum_{p=\phi_3}^{\phi_1-\Delta\phi_L e^{j\pi/4}} F(\phi_p)\Delta\phi_L e^{j\pi/4} + \sum_{p=\phi_1}^{\phi_2-\Delta\phi_C e^{j\delta}} F(\phi_p)\Delta\phi_C e^{j\delta} + \sum_{p=\phi_2}^{\phi_4} F(\phi_p)\Delta\phi_R e^{j\pi/4} \quad . \tag{3.76}$$

3.4.2.5 Operation Count for the SA Algorithm for Rough Surfaces

As we proposed before, the total operation count to determine the matrix-vector products in the gradient types of the iterative techniques is reduced to *O(N)*. To prove this, let's look at the forward propagating field evaluation. The operations to find the strong contributions are NxN_s $(N_s << N)$. The process to estimate the weak contributions in (3.60) and (3.66) is $(N\text{-}N_s)$x $4(Q_L + Q_C + Q_R)$ $(Q_L + Q_C + Q_R << N)$, where Q numbers are independent of N, and hence, do not increase with the increasing N and treating N_s as a constant number, if we sum up these two operation numbers we have an operation count of

$$N\text{x}N_s \; + \; (N - N_s)\text{x}4(Q_L + Q_C + Q_R) \; \rightarrow \; O(N) \tag{3.77}$$

which remains to be *O(N)*. The total memory storage is estimated as $3N$ vectors for the total, forward and backward fields and $(Q_L + Q_C + Q_R)$ plane waves.

3.5 Numerical Results for Quasi-planar Surfaces

In this section, we will present some numerical results for strip and slightly rough surfaces. The solutions constructed with BiCGSTAB method used in conjunction with SA algorithm. To show the accuracy of the method,

MoM solutions via Gauss elimination are employed and attached into the figures up to 2000 surface unknowns. For larger unknowns, the accuracy of the method is compared with the conventional BiCGSTAB method since it is not possible to store the interaction matrix and apply LU decomposition for the MoM. Both TM and TE polarization cases are investigated. The results are available for oblique and grazing incidence of plane waves, isotropic radiator and infinitesimal dipole antenna. To see the absorption effects of the terrain profile both PEC ($\eta_s = 0$) and imperfect conducting surfaces are considered. The stopping criterion of the SA-BiCGSTAB method is limited by the residual error of 10^{-3}. The lit region angle illustrated in Figure 3.26 is evaluated by $\beta_s = \sqrt{10/kL_s}$ with $L_s = (z_{\max} - z_{\min})/4$ yielding the number of integral points fixed in (3.49) and (3.50) as $2Q+1 = 139$ except the first example in Figure 3.29.

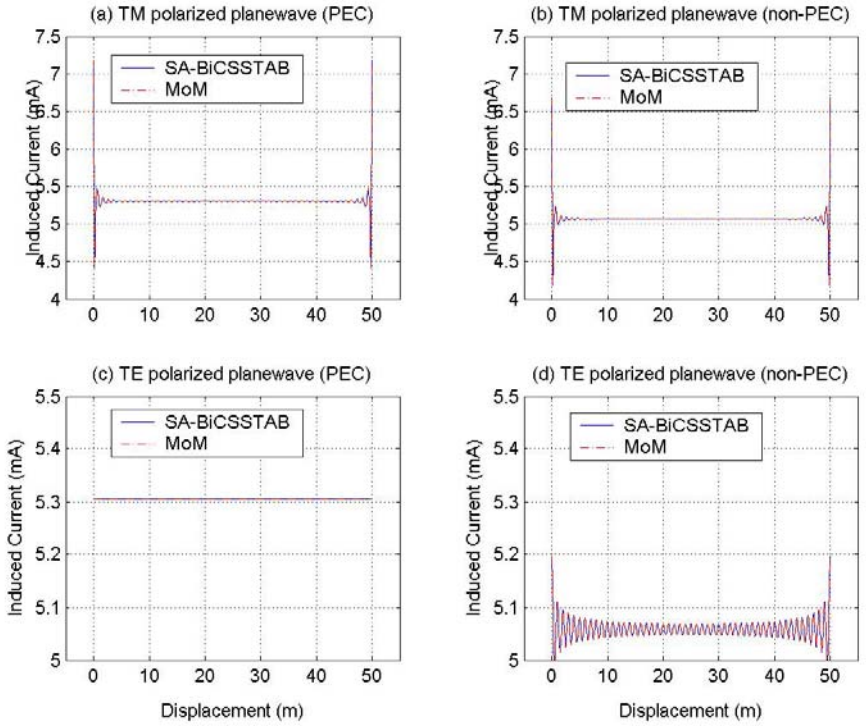

Figure 3.29 Distributed current on a strip, oblique plane wave incidence

The first result is an example of oblique incidence of a plane wave on a strip of width 50λ given in Figure 3.5. The strong region length L_s is chosen as 1λ which yields to N_s = 10. Q is computed to be 37, which means the number of the plane waves is $2Q$+1 = 75.

The results show us that SA-BiCGSTAB suits well with the reference MoM solutions. As mentioned before, for the TE case (Figure 3.29(c)), the induced current is the physical optics current $\mathbf{J}_s^{PO} = 2\hat{n}$ x $\mathbf{H}^{inc}$. Imperfect conducting cases are illustrated in Figure 3.29 (b) and (d) Due to material constitution, a little amount of the current is absorbed inside the profile. Also it is now possible to reach the numerically accurate results for the TE case.

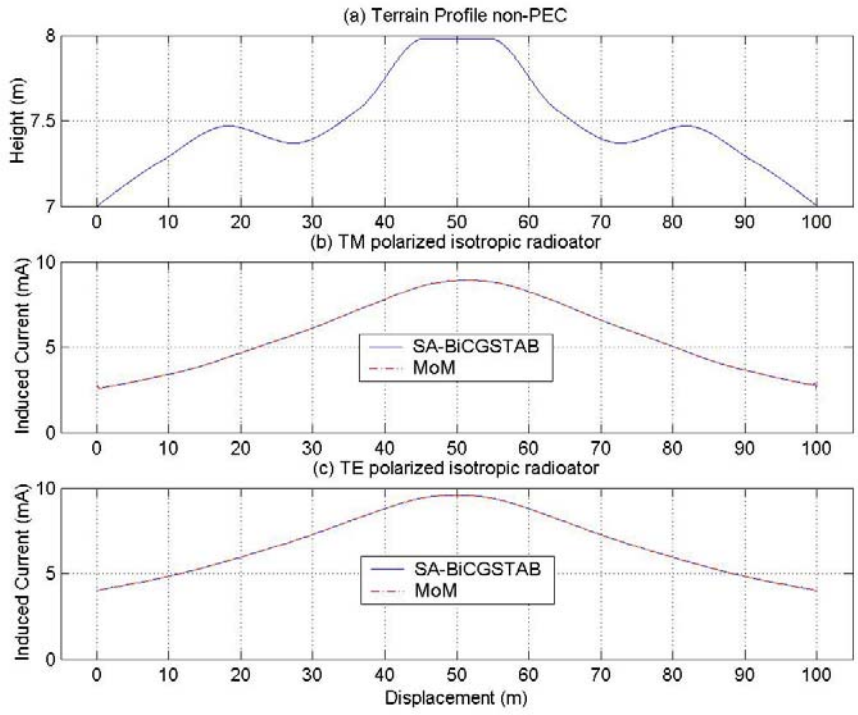

Figure 3.30 Isotropic radiator on a quasi-planar surface

Figure 3.30 illustrates a slightly rough surface of width 100λ with a maximum height deviation 0.98λ. The source is an isotropic radiator at a height above 25λ of the center with and average radiated power P_{rad} 18W. Non-PEC

case is considered with $\eta_s = 17.6 + j16.8$. The strong region length is taken as 0.3λ. Because of the symmetrical property of the terrain profile, induced currents are also symmetrical. Residual errors are plotted in Figure 3.31

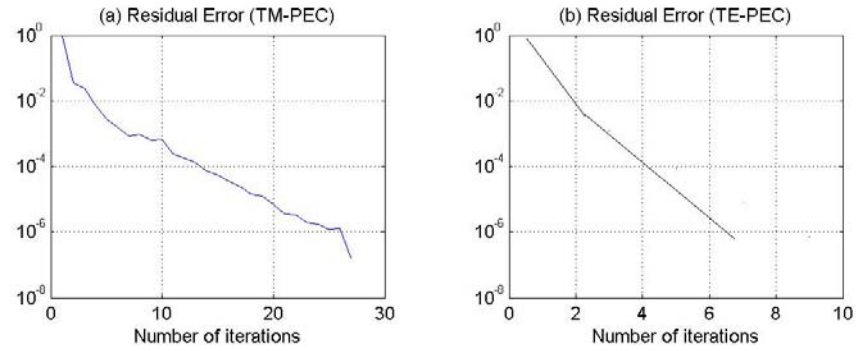

Figure 3.31 Residual errors for Figure 3.30

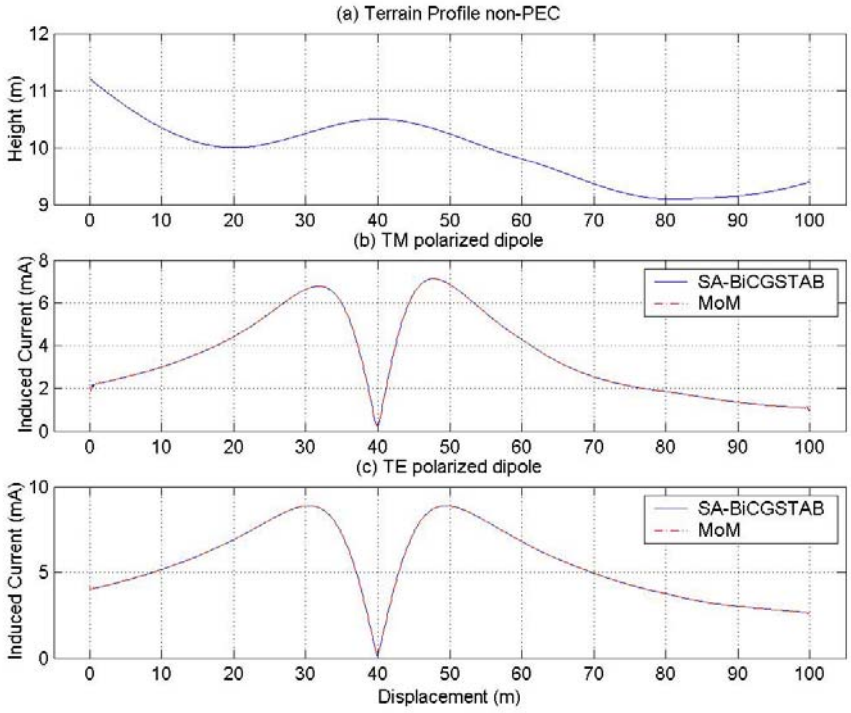

Figure 3.32 Dipole antenna on a quasi-planar surface

Figure 3.32 displays a terrain profile of width 100λ, illuminated by a dipole antenna located at the 40^{th} meters with a height of 10λ with P_{rad} 15W. The surface impedance is taken as $\eta_s = 15 + j20$. Error rates are given in Figure 3.33.

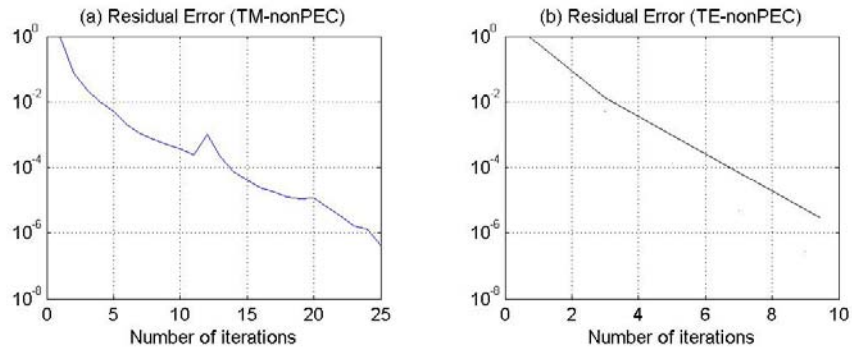

Figure 3.33 Residual errors of Figure 3.32

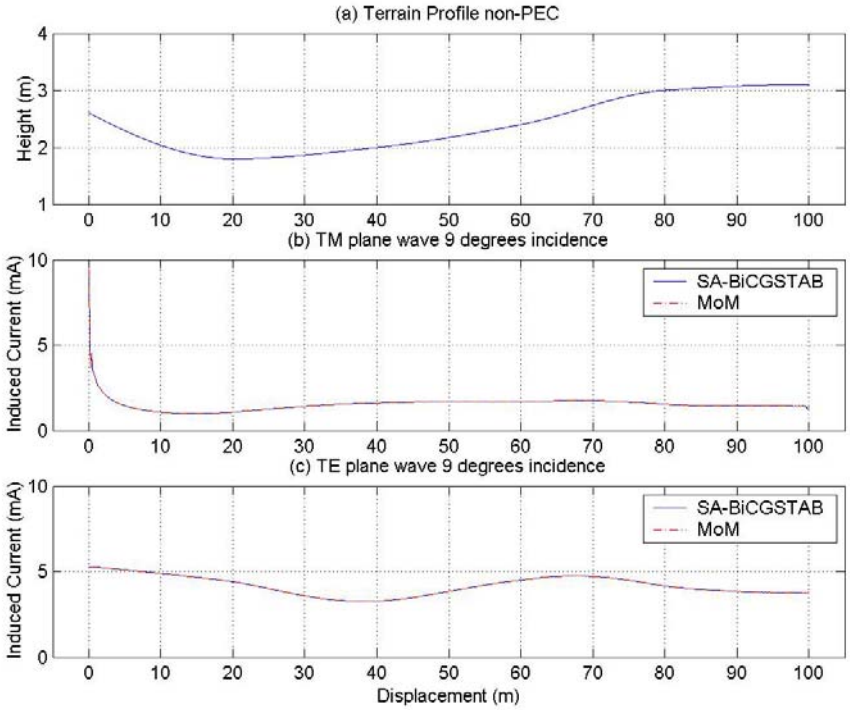

Figure 3.34 Plane wave on a quasi-planar surface with grazing incidence

Figure 3.34 is another example of 100λ width quasi-planar surface illuminated by a plane wave with a grazing incident angle $\theta = \pi / 20$. Non-PEC case is considered with $\eta_s = 20 + j15$. Residual error rates for both polarizations are given in Figure 3.35.

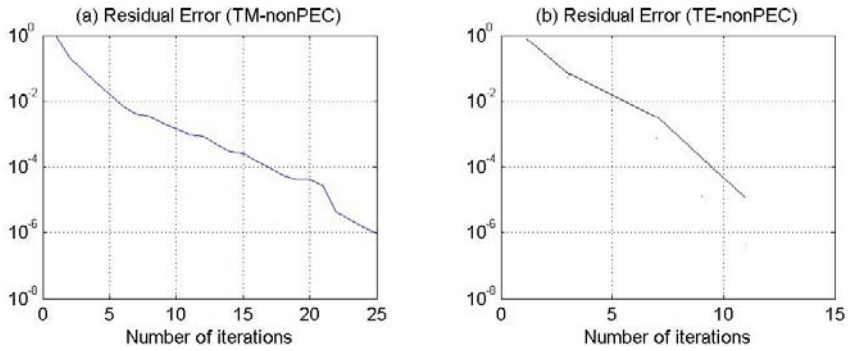

Figure 3.35 Residual errors for Figure 3.34

It's clear that SA-BiCGSTAB method's convergence ability, by means of number of iterations, is higher for TE polarization case.

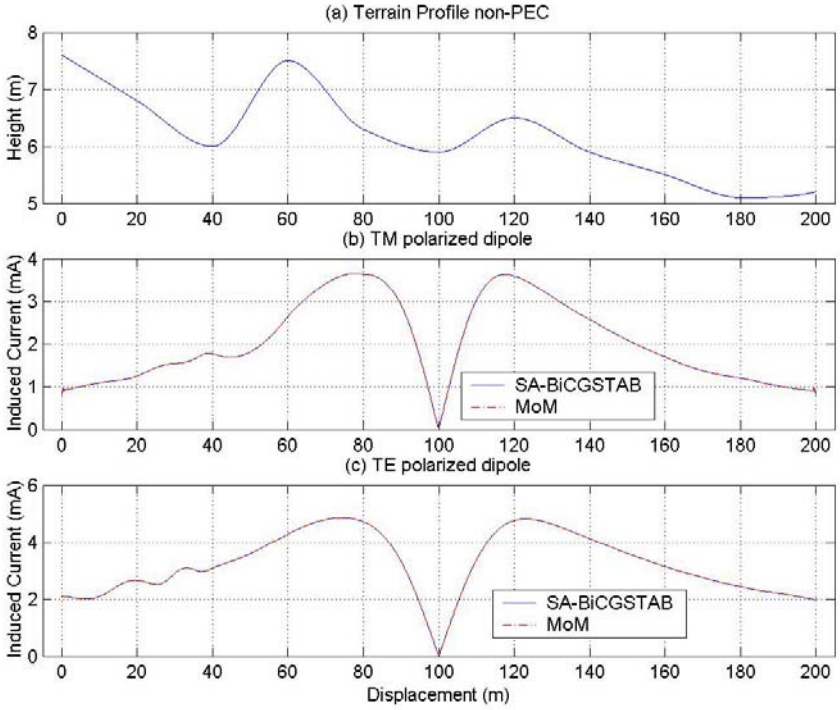

Figure 3.36 Dipole antenna on quasi-planar surface

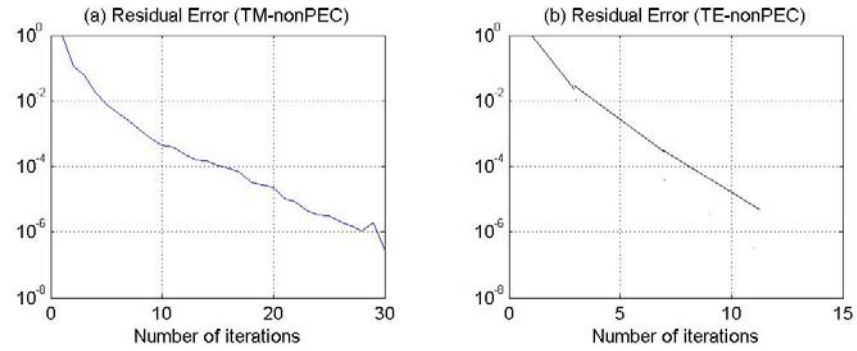

Figure 3.37 Residual errors for Figure 3.36

Figure 3.36 illustrates a quasi-planar surface profile of width 200λ yielding 2000 unknowns. The surface is illuminated by a dipole located symmetrically with a height 25λ above at the center of the terrain. Average radiated power is P_{rad} 25W. Surface impedance is $\eta_S = 17.6 + j16.8$. Residual error rates are plotted in Figure 3.37.

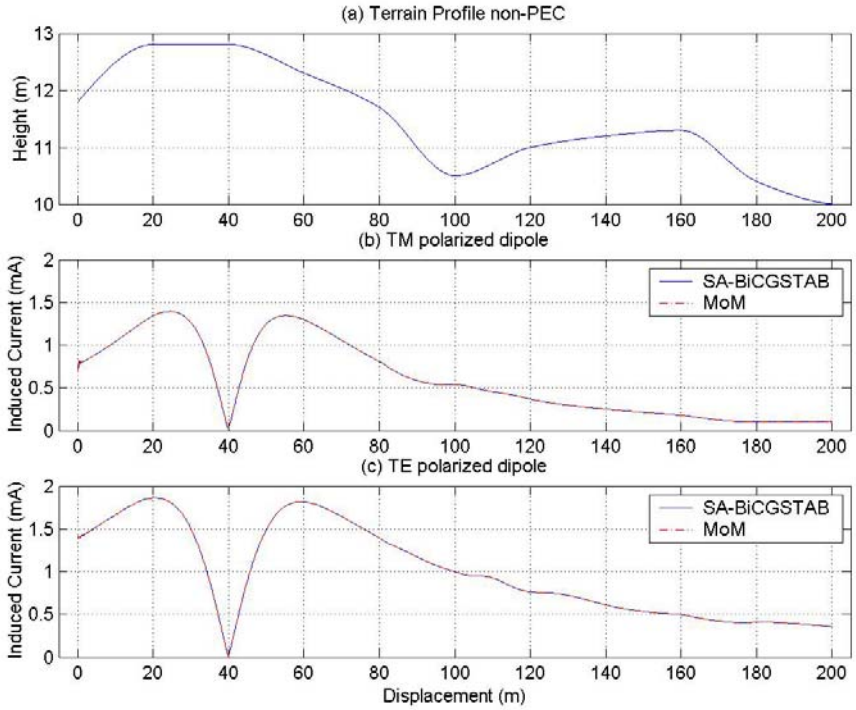

Figure 3.38 Dipole antenna on quasi-planar surface

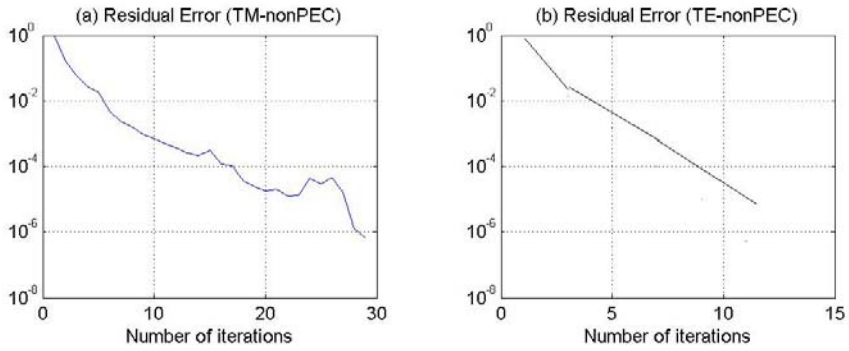

Figure 3.39 Residual errors for Figure 3.38

Figure 3.38 illustrates a quasi-planar surface profile of width 200λ yielding 2000 unknowns. The surface is illuminated by a dipole located at a height above 25λ at the 40^{th} meters of the terrain. Average radiated power is P_{rad} 2.5W. Surface impedance is $\eta_S = 17.6 + j16.8$. Residual error rates are plotted in Figure 3.39.

The next example is an unordered surface profile. The target under test is a ship placed on a 400 meters sea surface. The electrical length properties are illustrated in Figure 3.16. To generate random sea surface for a given wind speed, an infinite-depth Pierson-Moskowitz ocean spectrum [27] is used. Imperfect conducting case is considered. As we mentioned before since the surface of the scatter is multi-valued, stationary methods such as FBM can not solve this kind of problem. In order to show the validity of the SA-BiCGSTAB the results are compared with spectral accelerated generalized forward-backward method (SA-GFBM). To cope with divergence in a multi valued region, Pino *et all.* [29] have introduced a generalized version of spectrally accelerated forward-backward method.

The results are evaluated for TM polarization both for PEC and non-PEC cases. For the imperfect conducting case, the sea is modeled with an

surface impedance $\eta_s = 76.4 - j65.1$ while the ship remains PEC. Plane wave incidence is considered with an angle $\theta = \pi / 36$. Current distributions on the surface of the sea and the ship due to 0 m/s, 5m/s and 10m/s wind speed are plotted in Figure 3.40 Figure 3.41 and Figure 3.42, respectively. The frequency is 300MHz with N=4500. To use the competence of SA algorithm to study on this sea profile, some of the parameters at the original algorithm is modified. The first one is the lit region angle, β_s, demonstrated in Figure 3.26. Since the maximum height deviation is increased, the lit region in the spatial domain must be enlarged. The second parameter, on which a modification is applied, is the limit value of the integrand of the maximum saddle point. Instead of restricting it to the original value of e^{20}, e^2 is chosen. As stated earlier, because of the reentrant surface sections due to the ship profile, the diagonally dominant property of the impedance matrices for both TM and TE polarization cases are no longer valid. Hence, the number of iterations to reach the desired level of residual error is about 72. Nevertheless, the total computational time is about 12 minutes for each polarization, which seems really cost effective when compared with the solution of the problem by the conventional BiCGSTAB method.

Figure 3.43 is an example of a quasi-planar rough surface of width 1000λ with a maximum height deviation 1.7λ. Profile is illuminated with a infinitesimal dipole antenna located at 60^{th} meters at the x axis above a height of 25λ. The average radiated power P_{rad} given by the source is 25W. Imperfect conductivity property of the terrain is considered with the surface impedance $\eta_s = 20 + j15$. Since the number of unknowns is 10000 (at 300MHz frequency), MoM result is not available. Thus the comparison to validate the accuracy of the method is made by the original BiCGSTAB method. The residual error rates are plotted in Figure 3.44

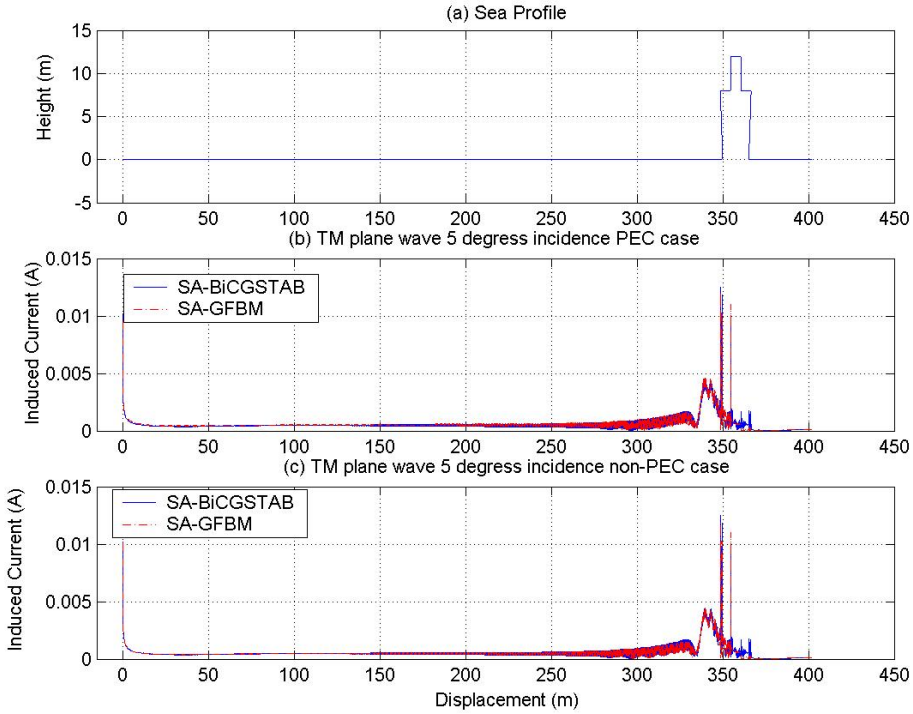

Figure 3.40 Current distribution on a ship (wind speed: 0m/s)

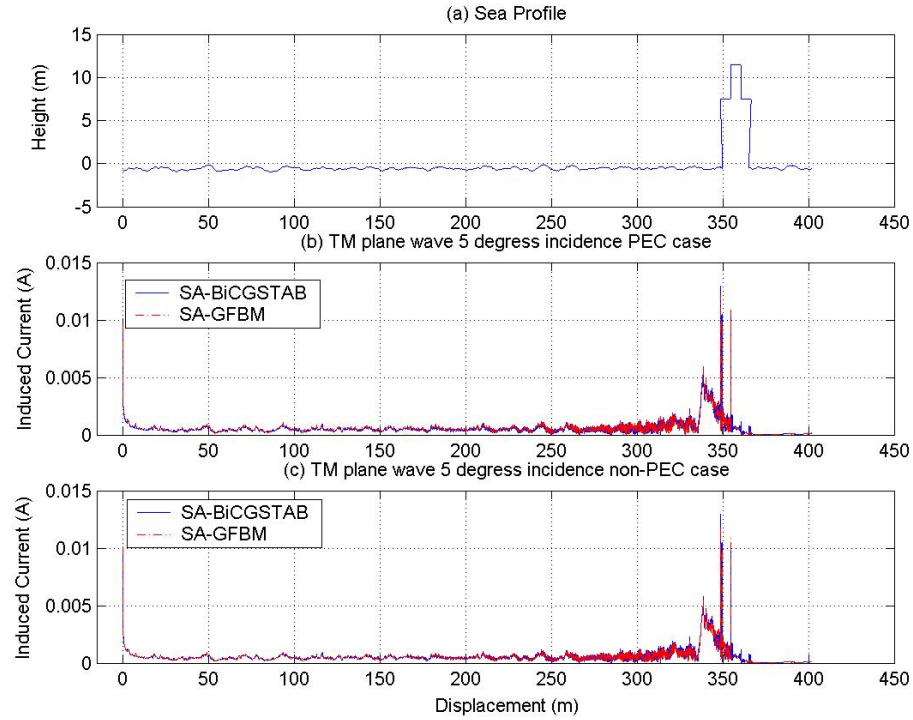

Figure 3.41 Current distribution on a ship (wind speed: 5m/s)

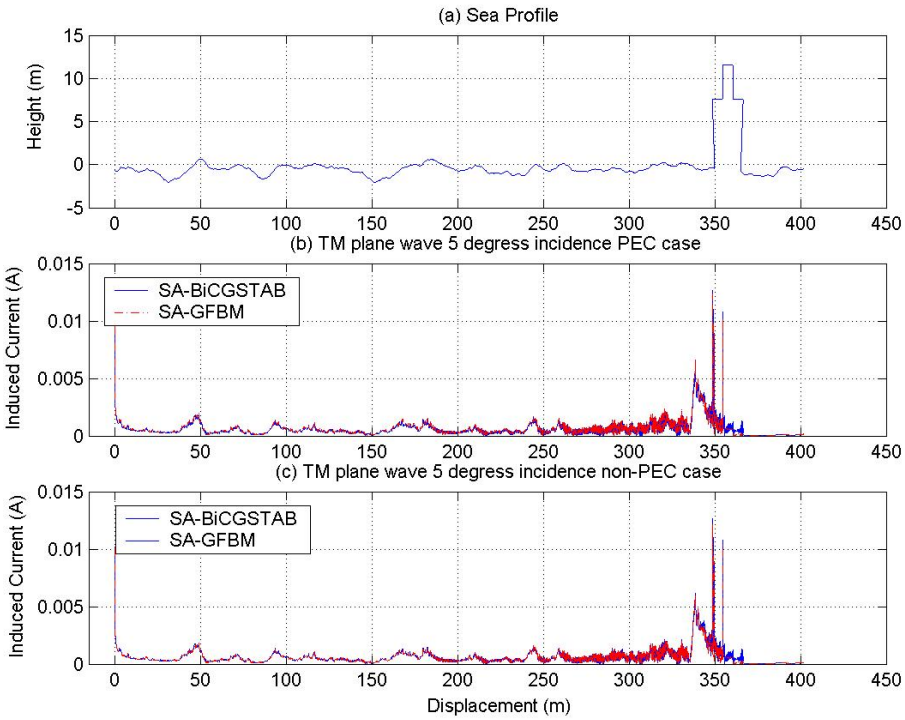

Figure 3.42 Current distribution on a ship (wind speed: 10m/s)

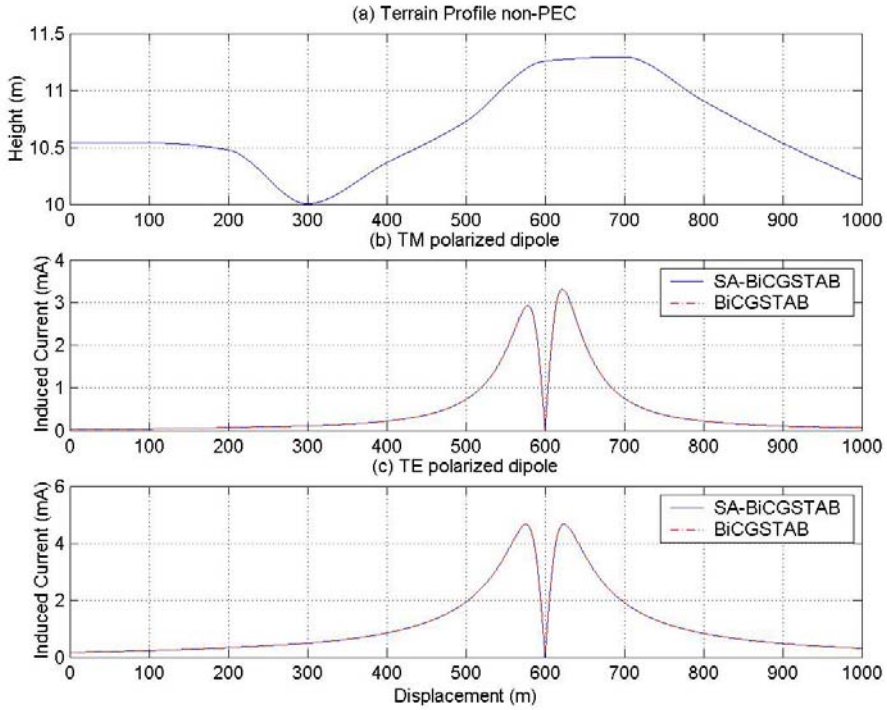

Figure 3.43 Dipole on a quasi-planar surface of width 1000λ

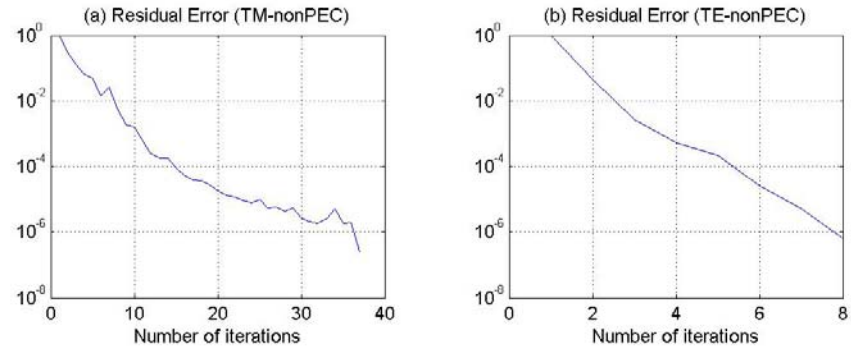

Figure 3.44 Residual errors of Figure 3.43

Figure 3.45 shows an imperfect conductor rough surface (the maximum height deviation is a multiple of wavelength) of width 200λ. The source is a dipole located at the center with a height 25λ above. P_{rad} is 25W. The strong region length is 12λ.

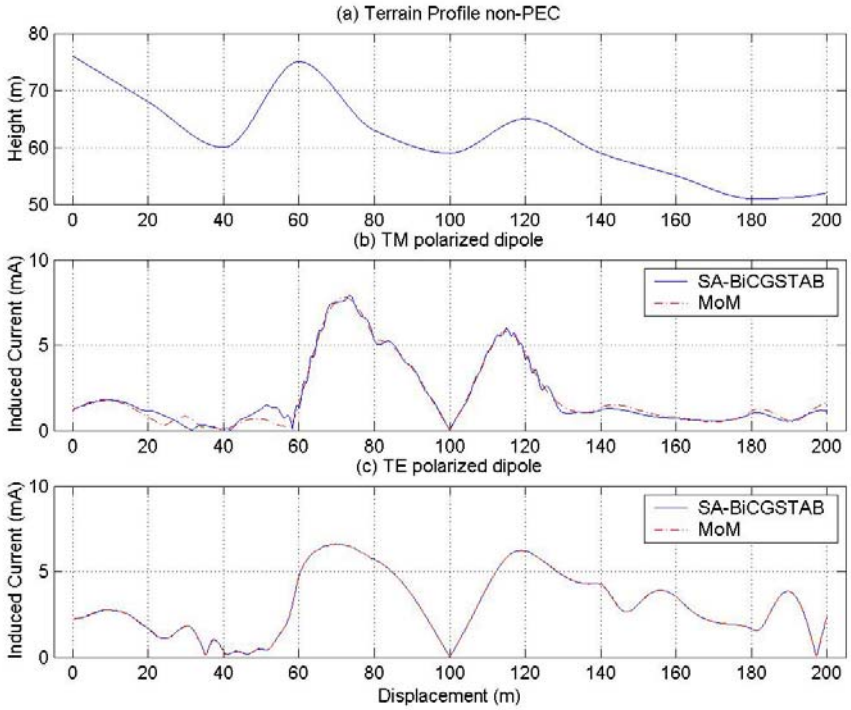

Figure 3.45 Dipole antenna on a quasi-planar surface

For the case seen in Figure 3.45 (b), differences occur between the MoM and SA-BiCGSTAB method. The original spectral acceleration algorithm is proposed for quasi-planar surfaces or slightly rough surfaces like sea profiles. When these kinds of surfaces are considered, the saddle points are distributed around the origin along the real axis of the complex ϕ plane. However, when the height deviation is increased, the homogenous distribution around the origin will no longer exist.

As the number of the surface increases, huge number of saddle points will start to make groups around the outer most saddle point $\phi_{s,\max}$. These saddle points' steepest ascent paths will cross the deformed contour. Hence, the limit value e^{20} of the integrand in the weak contribution region will not be suitable. To avoid the weak field from exponential growth situation, limiting the integrand value to a smaller quantity will be appropriate. However, this suggestion does not overcome inability of the spectral acceleration when undulating geometries are under of interest. The reason for that is the location of the deformed contour. For a downhill profile, the location of the saddle points will not be distributed around origin but a negative value on the axis on the real axis and for an uphill terrain geometry, saddle points will be allocated about a positive value on the axis. Thus, the deformed contour should cross the real axis at these medium points depending on slope of the terrain geometry.

In order to overcome this limitation, the spectral acceleration algorithm is modified to handle rough terrain geometries. Applications of the modified spectral acceleration algorithm issued for rough terrain profiles are discussed in the next chapter with also evaluation of scattered field.

Chapter 4

Computation of Scattered Field on the Rough Surface Profiles

4.1 Introduction

Once the current distribution over the terrain profile has been evaluated by BiCGSTAB method in conjunction with spectral acceleration, the scattered field can be computed using this current distribution to find the coverage due to the source. If the region of interest is limited to a small portion of the surface, the numerical evaluation of the scattered field consists of a reduced number of operations but if the region under study is extended to the complete path of the terrain profile, the computation of the field strength requires an operation count of $O(N^2)$ similar to MoM discretization. This in an unsuitable situation for electrically large surface profiles. To overcome this fact, the spectral acceleration algorithm can be applied to scattered field calculations to reduce the computational cost to $O(N)$.

This chapter is devoted to the discussion of evaluating the scattered field over electrically large rough terrain profiles. Section 4.2 discusses the computation of the scattered field by making use of the spectral acceleration algorithm, and Section 4.3 presents numerical examples of the scattered field due to the current distribution evaluated by SA-BiCGSTAB method. The results are compared with conventional BiCGSTAB method and spectral accelerated forward-backward method (SA-FBM) [31].

4.2 Computation of Scattered Field with Spectral Acceleration

As explained in Chapter 2, the scattered field can be expressed as

$$E_y^{scat}(\boldsymbol{\rho}_n) \cong -\frac{\omega\mu}{4}\sum_{m=1}^{N} I_m \Delta x_m H_0^{(2)}(k|\boldsymbol{\rho}_n - \boldsymbol{\rho}_m|) - j\frac{k}{4}\sum_{m=1}^{N} I_m \Delta x_m \eta_m H_1^{(2)}(k|\boldsymbol{\rho}_n - \boldsymbol{\rho}_m|)\hat{n}_m.\hat{\rho}_{nm} \tag{4.1}$$

for TM polarization, and

$$H_y^{scat}(\boldsymbol{\rho}_n) \cong \frac{\omega\varepsilon}{4}\sum_{m=1}^{N} I_m \Delta x_m \eta_m H_0^{(2)}(k|\boldsymbol{\rho}_n - \boldsymbol{\rho}_m|) + j\frac{k}{4}\sum_{m=1}^{N} I_m \Delta x_m H_1^{(2)}(k|\boldsymbol{\rho}_n - \boldsymbol{\rho}_m|)\hat{n}_m.\hat{\rho}_{nm} \tag{4.2}$$

for TE polarization. In (4.1) and (4.2), I_m denotes the computed induced current on the source point ρ_m, and ρ_n is the observation point where the scattered field is evaluated.

Consider a terrain profile *C* depicted in Figure 4.1 and assume that the scattered field is to be computed at *h* meters above of the original path given with C_s in the same figure. To include the spectral acceleration algorithm to scattered field computations, radiations due to source points are divided into two groups; those coming from the *forward region,* and those coming from the *backward region* as illustrated in Figure 4.1. With this decomposition, the scattered field for the k^{th} element can be given by

$$SF(\boldsymbol{\rho}_k^s) = SF_f(\boldsymbol{\rho}_k^s) + SF_b(\boldsymbol{\rho}_k^s). \tag{4.3}$$

Here, *SF* denotes the scattered field given by (4.1) for TM polarization and by (4.2) for TE polarization, respectively. The subscript *f* at the right hand side of

(4.3) indicates the contribution due to forward region and subscript *b* symbolizes the contribution of backward region. Analogous to the original spectral acceleration algorithm, these two regions are treated separately.

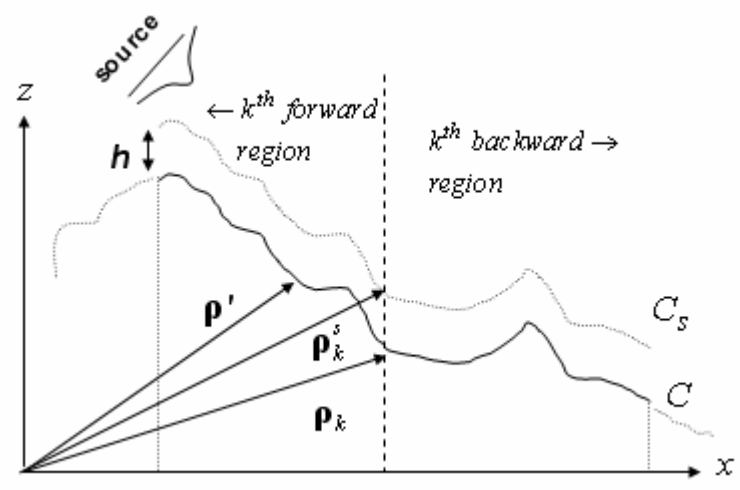

Figure 4.1 The scattering zone of a generic terrain profile

For the forward region, due to typical spectral acceleration assumption, contributions are also divided into two clusters denoted as *strong* and *weak*, namely. The forward field at the k^{th} element can be estimated from the preceding element by reevaluating the *strong* group radiation and updating the spectral representation of the *weak* group interaction like recursive formulations in (3.60) for TM polarization and (3.66) for TE polarization, respectively. Backward region can be treated in the same manner. As a result of these approximations, the scattered field can be computed with a computational cost of *O(N).*

4.3 Numerical Results for Rough Surfaces

The numerical results for rough surfaces are obtained using BiCGSTAB method in conjunction with spectral acceleration algorithm. Plane wave,

isotropic radiator and infinitesimal dipole type sources, whose properties are explained in Section 3.3.1 are used. To show the validity of SA-BiCGSTAB method, scattered field computations are compared with conventional BiCGSTAB method and also the spectrally accelerated forward-backward method SA-FBM [31]. To validate the SA-BiCGSTAB method when comparing with the SA-FBM, the difference error is defined as

$$diff.\,error = \left| E_s^{SA-BiCSGTAB} - E_s^{SA-FBM} \right| \tag{4.4}$$

where $|\,.\,|$ denotes the absolute value. Scattered fields are evaluated at a height h = 1.8λ above the terrain. The study parameters, which are used in conjunction with the modified spectral acceleration algorithm for the rough terrain profiles, are also included in study parameter tables. In these tables, ϕ_{med} is the medium angle giving an idea about the slope of the terrain (downhill or uphill geometry) whereas, $\phi_{s,min}$ and $\phi_{s,max}$ are the minimum and maximum slopes of the terrain, respectively. δ is the inclination angle of the central stretch of the deformed contour. Study tables also contain the number of the integral points taken on the deformed contour.

A non-PEC ($\eta_s = 20 + j15$) rough surface profile of width 200λ is depicted in Figure 4.2(a). The surface is illuminated by a dipole antenna located at a 25λ height above the left-most point on the terrain. The average radiated power is considered to be 25 Watts. Scattered field is plotted for both polarizations. The parameters needed to implement the SA-BiCGSTAB to this geometry are included in Table 4.1. To show the accuracy of the method, the results are compared with SA-FBM method and the difference error with respect to the displacement is illustrated in Figure 4.3. It is possible to notice the good grade of accuracy between the results provided by SA-FBM and SA-BiCGSTAB solutions.

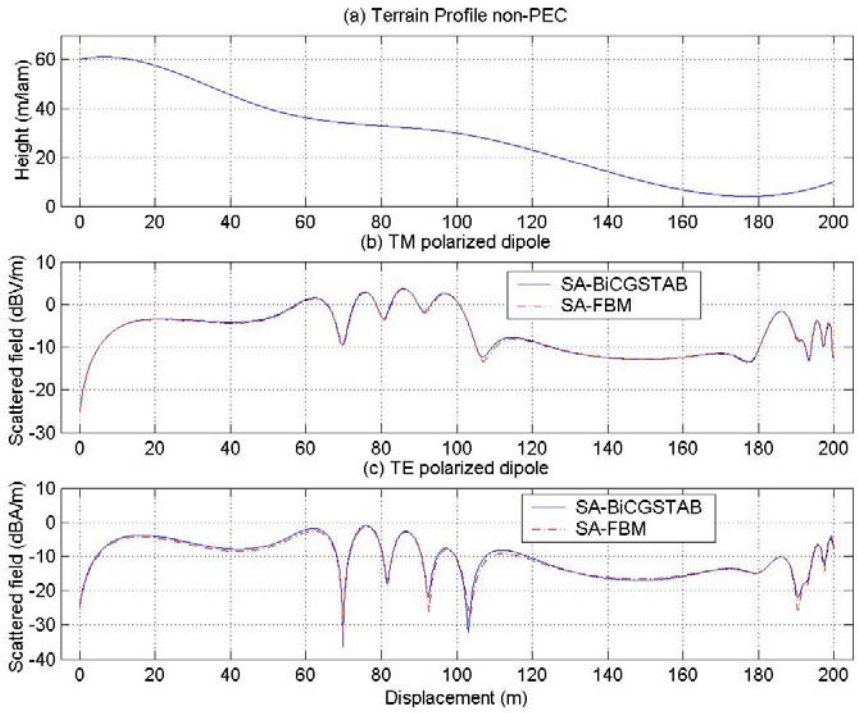

Figure 4.2 Scattered fields from a 200λ width rough surface

Figure No:	4.2	4.4	4.6	4.8	4.10
Number of unknowns (N)	2000	5000	10000	10000	10000
Frequency (MHz)	300	300	300	300	300
ϕ_{med} (rad)	-0.290	-0.075	0.143	-0.036	-0.057
$\phi_{s,min}$ (rad)	-0.572	-1.112	-1.012	-0.256	-0.700
$\phi_{s,max}$ (rad)	0.511	0.955	0.896	0.262	0.452
L_s (λ)	2	2	2	2	2
Num. of integr. Points	312	700	814	260	425
δ (rad)	0.264	0.103	0.112	0.188	0.108

Table 4.1 Study parameters

As can be seen in Figure 4.2 (a), since the terrain geometry is a downhill profile the medium saddle point (in Table 4.1) giving an idea about the slope of the terrain, is located on the negative real axis. The deformed contour of numerical integration is located nearly symmetrically around this saddle point, thus, the numerical integration yields good results. One other important detail about the modified SA algorithm is the limitation of strong region length L_s. The original acceleration technique for the quasi-planar surfaces usually generates accurate results when the neighborhood distance is chosen as $L_s = (z_{max} - z_{min})/4$. But since this region is evaluated through the conventional matrix-vector multiplication, the computational cost increases for rough geometries because of large height deviation. By forming robust integral paths along which the integrand decays rapidly, shrinking the strong region lengths therefore enlarging the weak contribution zones independent of height deviation or unknowns not only delivers precise results but also decreases the computational cost.

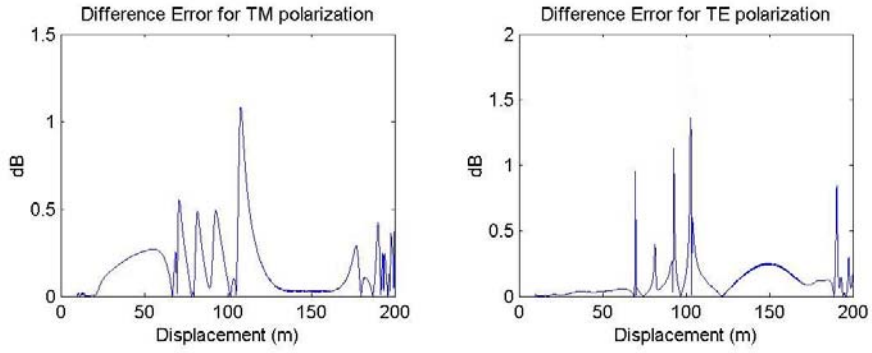

Figure 4.3 Difference errors for scattered fields of Figure 4.2

Figure 4.4 is an example of a 500λ with PEC terrain profile. The study parameters for spectral acceleration algorithm are included Table 4.1. Since the geometry is a downhill profile the medium saddle point is located on the negative real axis. The surface is considered to be illuminated by a dipole

antenna located at a 25λ height above the middle of the terrain. The average radiated power transmitted from the infinitesimal dipole is 40 Watts. The results are obtained for both horizontal and vertical polarizations and compared with SA-FBM. Scattered field is also determined by employing the spectral acceleration to reduce the operation count to *O(N)*. Difference errors are depicted in Figure 4.5. Error plots show that SA-BiCGSTAB converges successfully to accurate results. Figure 4.6 is an example of a rough surface of width 1000λ. Imperfect conductivity case is considered with the surface impedance $\eta_s = 15 + j20$. The parameters needed to implement the SA-BiCGSTAB to this geometry are included into Table 4.1. Since the geometry is an uphill profile the medium saddle point is located on the positive real axis.

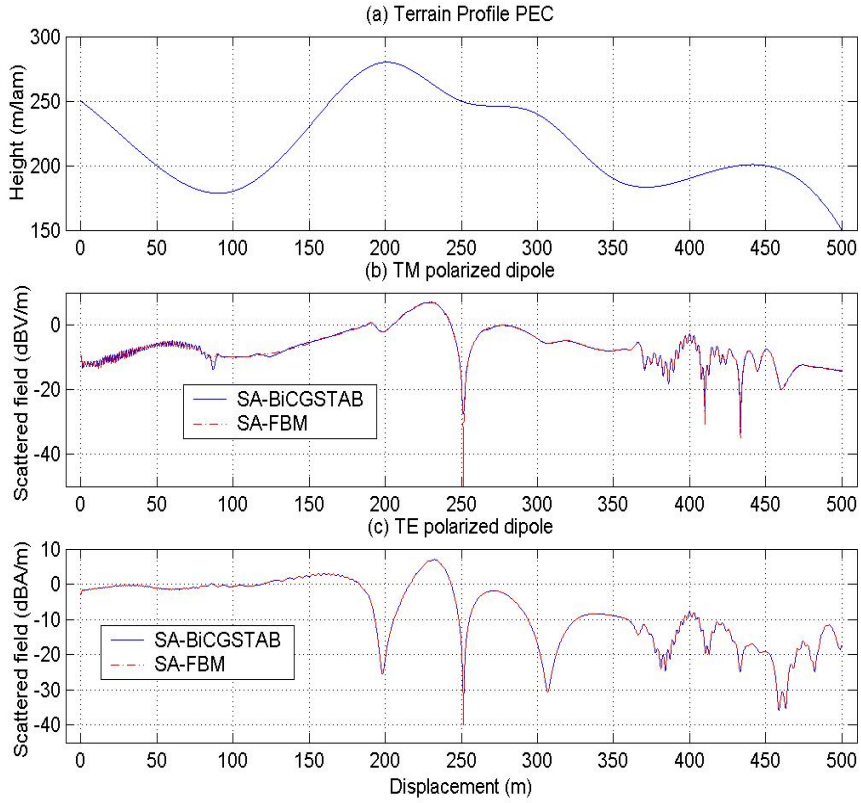

Figure 4.4 Scattered fields from a 500λ width rough surface

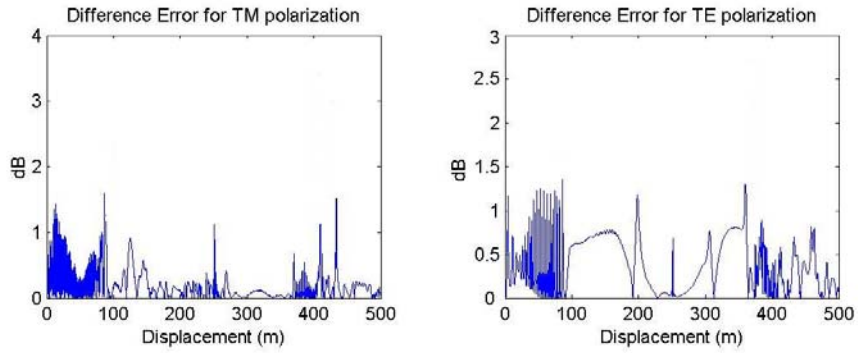

Figure 4.5 Difference errors for scattered fields of Figure 4.4

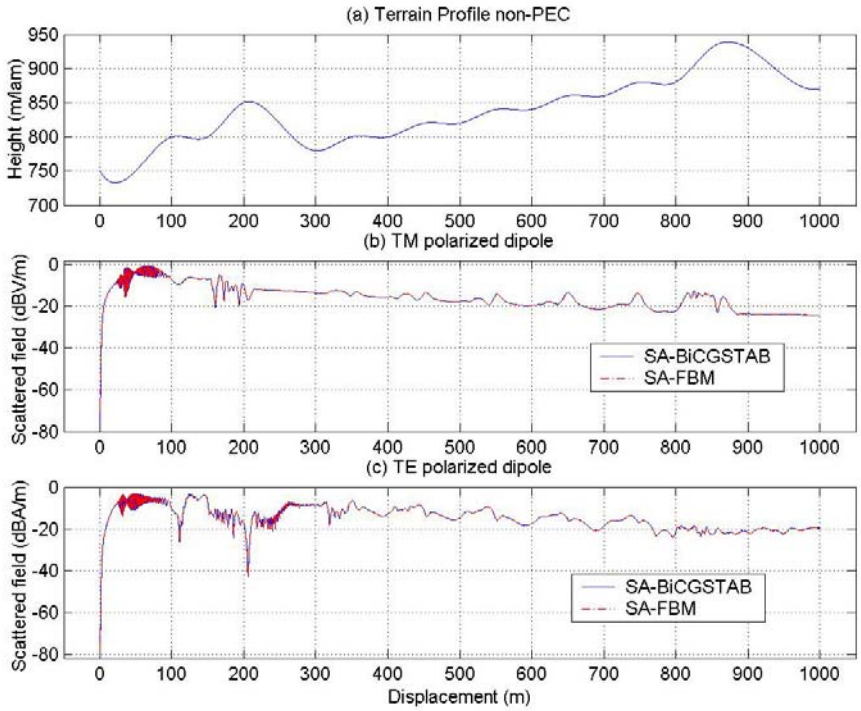

Figure 4.6 Scattered fields from a 1000λ width rough surface

This surface is considered to be illuminated by a dipole antenna located at 40λ height above the left-most point of the terrain. The average radiated power from the infinitesimal dipole is assumed to be 40 Watts. To guess the accuracy of the method, results are compared with SA-FBM. Scattered field results are also obtained by applying the spectral acceleration. As can be seen

from Figures 4.6 (b) and 4.6 (c), SA-BİCGSTAB successfully converges to the exact solution for both polarizations. The difference errors for this example are illustrated in Figure 4.7

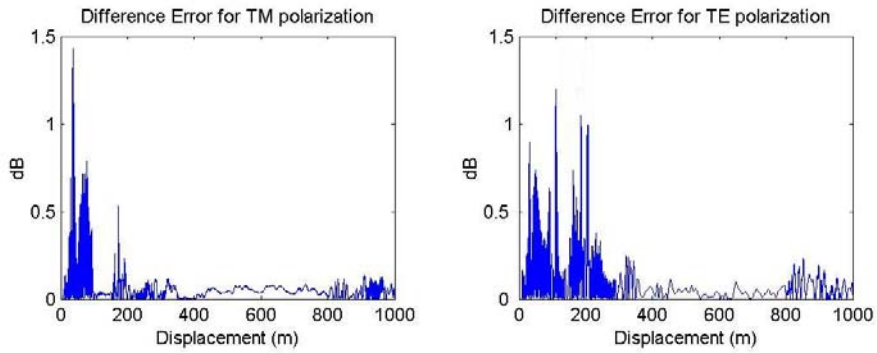

Figure 4.7 Difference errors for scattered fields of Figure 4.6

Figure 4.8 shows an example of a 1000λ width rough surface with the surface impedance $\eta_S = 17.6 + j16.8$. The parameters needed to implement the SA-BiCGSTAB to this geometry are included into Table 4.1. Since the geometry is a downhill profile, the medium saddle point is located on the negative axis. This surface is considered to be illuminated by a plane wave with an incident angle of $\theta = \pi / 20$ (grazing incidence). To show the accuracy of the method, results are compared with the original BiCGSTAB method. Difference errors are also depicted in Figure 4.9.

Figure 4.10 is another 1000λ width rough surface illuminated by grazing incident plane wave with the same surface impedance given for the preceding the example. Parameters required to implement the SA-BiCGSTAB to this geometry is included into Table 4.1. Since the geometry is a downhill profile, the medium saddle point is located on the negative axis. Results are compared with conventional BiCGSTAB method. Difference errors as defined in (4.4) are illustrated in Figure 4.11.

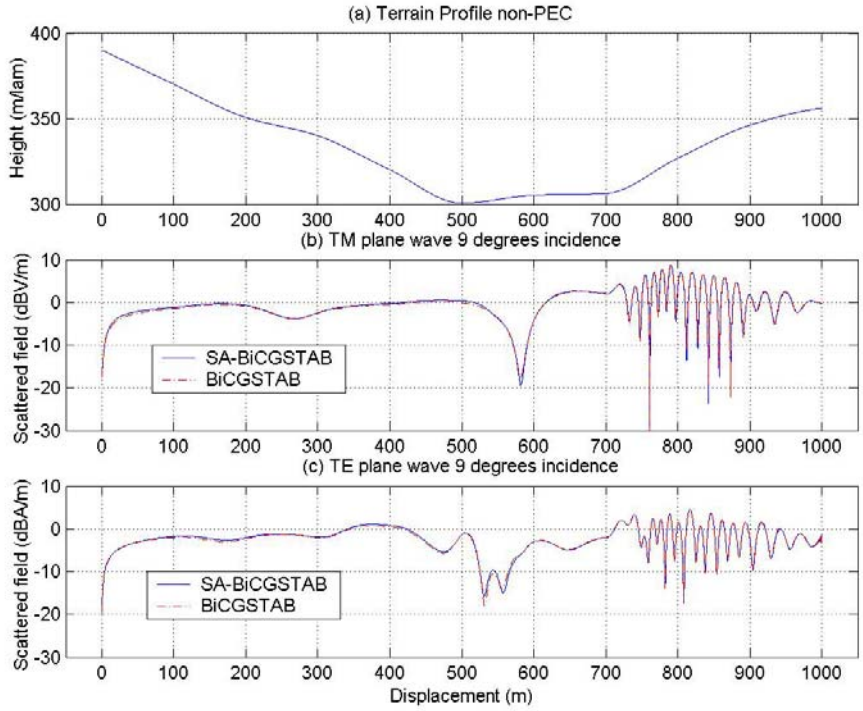

Figure 4.8 Scattered fields from a 1000λ width rough surface

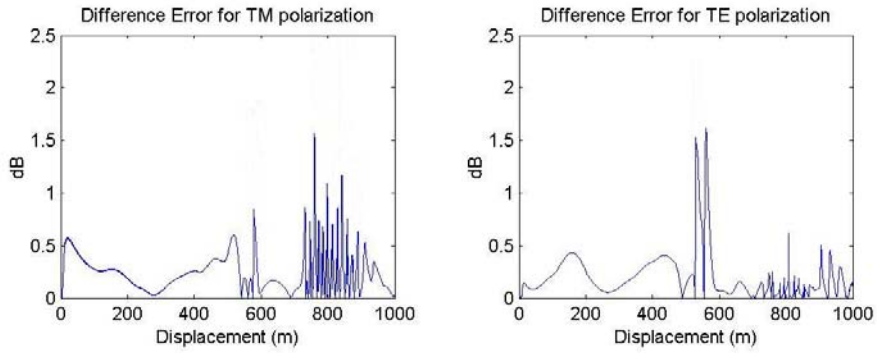

Figure 4.9 Difference errors for scattered fields of Figure 4.8

Figure 4.12 shows a 2000λ width non-PEC rough surface profile ($\eta_s = 20 + j20$). The study parameters for the recognition of the integral path due to this geometry are included in Table 4.2. Since geometry is going downwards, the medium saddle point is located on the negative real axis. This surface is assumed to be illuminated by a dipole antenna located at a 25λ above

the left-most point of the terrain. The average transmitted power is considered to be 25 Watts. Difference errors are depicted in Figure 4.13.

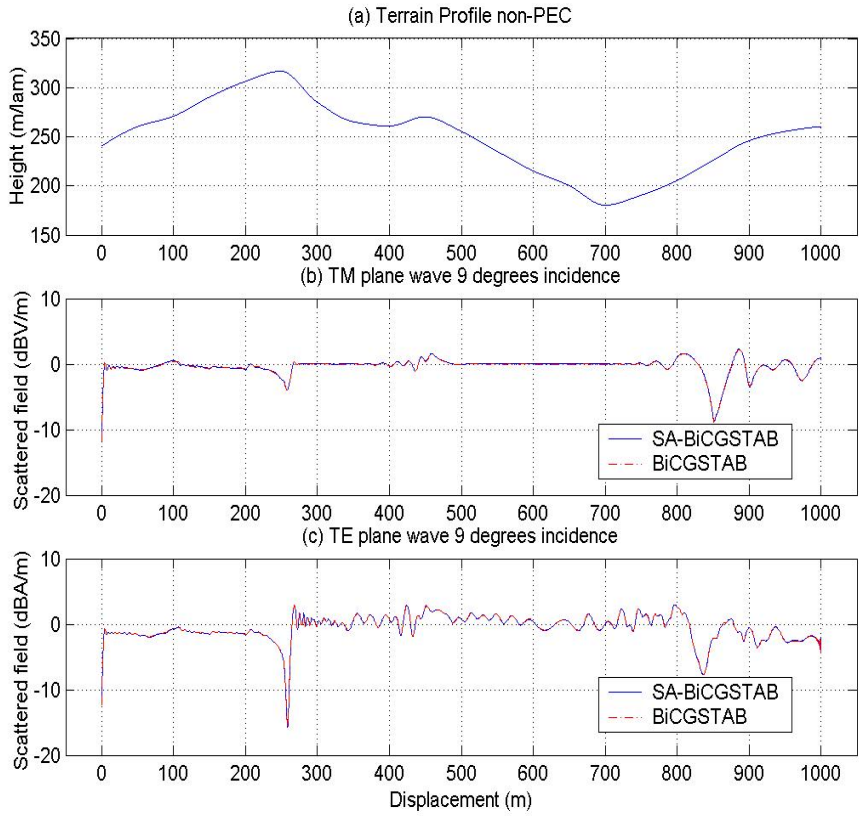

Figure 4.10 Scattered fields from a 1000λ width rough surface

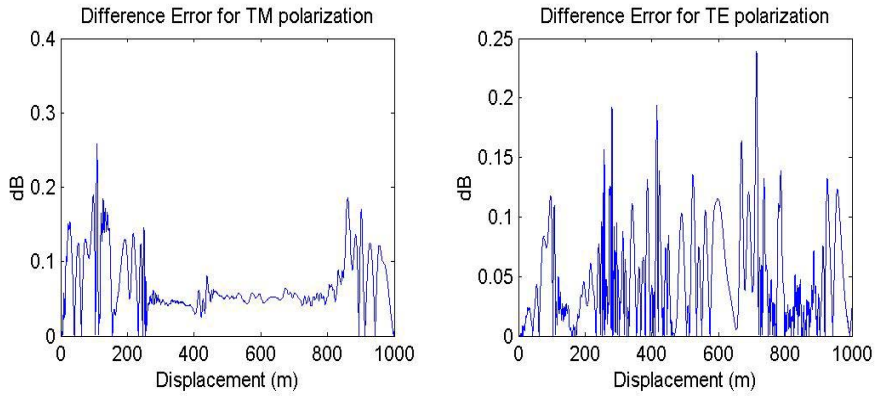

Figure 4.11 Difference errors for scattered fields of Figure 4.10

Figure No:	4.12	4.14	4.15	4.16	4.17
Number of unknowns (N)	20000	100000	100000	100000	200000
Frequency (MHz)	300	300	300	300	300
ϕ_{med} (rad)	-0.015	0.045	-0.011	0.026	-0.015
$\phi_{s,min}$ (rad)	-0.229	-0.137	-0.236	-0.214	-0.232
$\phi_{s,max}$ (rad)	0.120	0.371	0.204	0.176	0.120
L_s (λ)	2	2	2	2	2
Num. of integr. Points	743	468	594	483	538
δ (rad)	0.093	0.106	0.117	0.103	0.094

Table 4.2 Study parameters

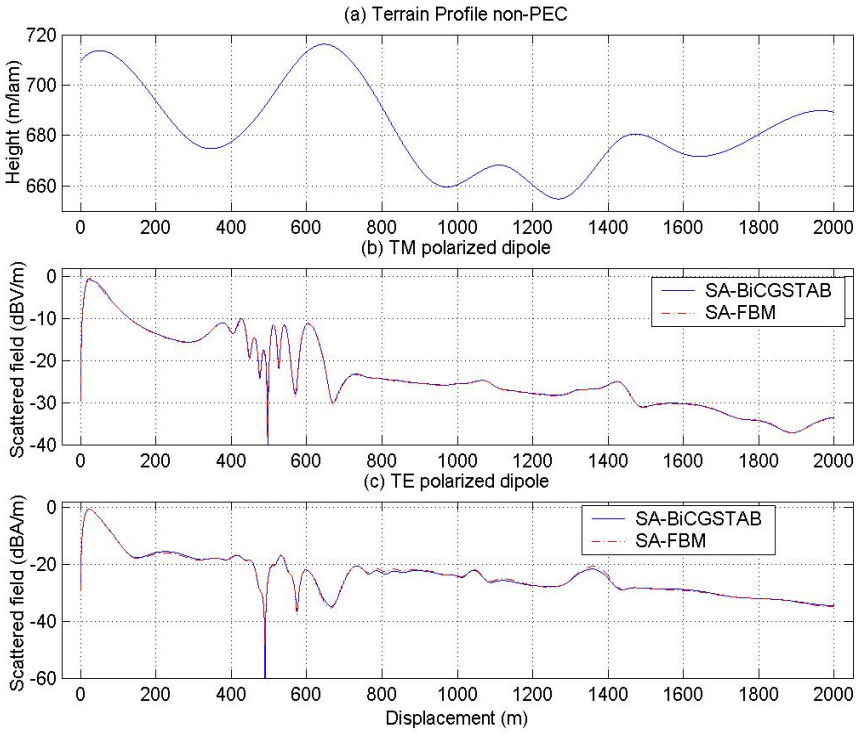

Figure 4.12 Scattered fields from a 2000λ width rough surface

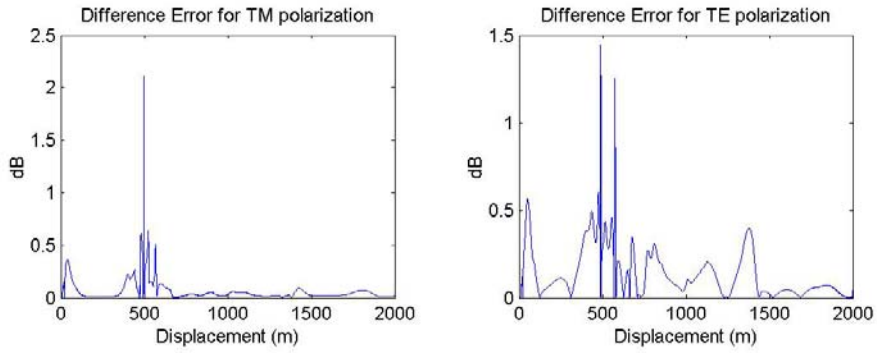

Figure 4.13 Difference errors for scattered fields of figure 4.12

Figure 4.14 shows a non-PEC terrain profile of width 10000λ with the surface impedance $\eta_S = 20 + j20$. The parameters needed to implement the geometry of the surface for the acceleration algorithm are included in Table 4.2. Since the geometry is an uphill profile, the medium saddle point is located on the positive real axis. Results are compared with SA-FBM. The surface is considered to be illuminated by a dipole antenna located at a 60λ height above in the middle point of the terrain. The average radiated power is 90 Watts.

Figure 4.15 shows a non-PEC terrain profile of width 10000λ with the surface impedance $\eta_S = 20 + j15$. The parameters defining the integration path for the weak contribution are included in Table 4.2. Since the geometry is a downhill profile, the medium saddle point is located on the negative real axis. The surface is considered to be illuminated by a dipole antenna located at a 50λ height above in the middle point of the terrain. The average radiated power is 100 Watts. To validate the SA-BİCGSTAB method with this geometry, the scattered field results are compared to the solution given by SA-FBM.

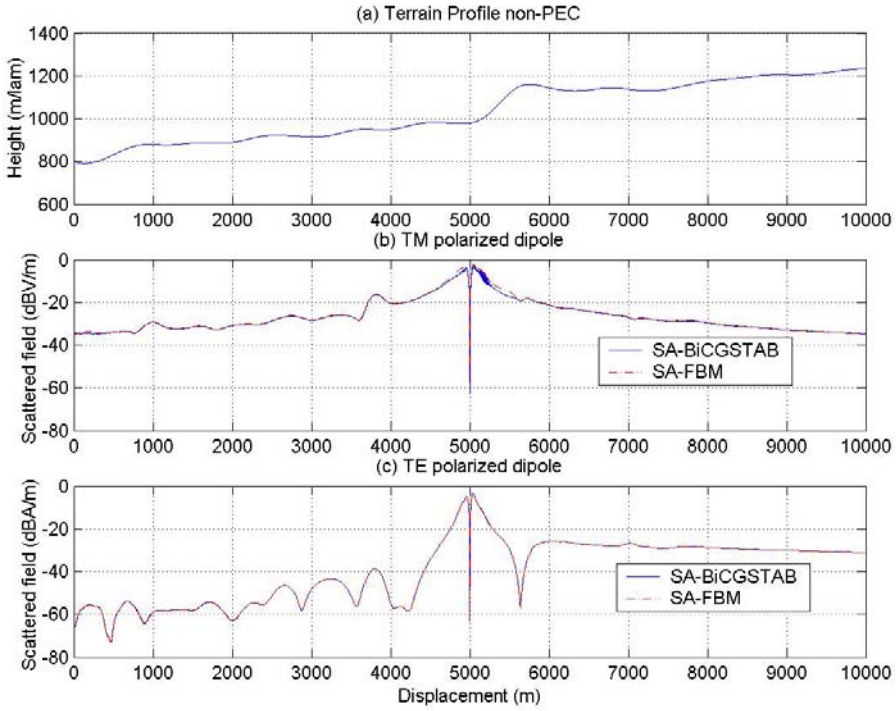

Figure 4.14 Scattered fields from a 10000λ width rough surface

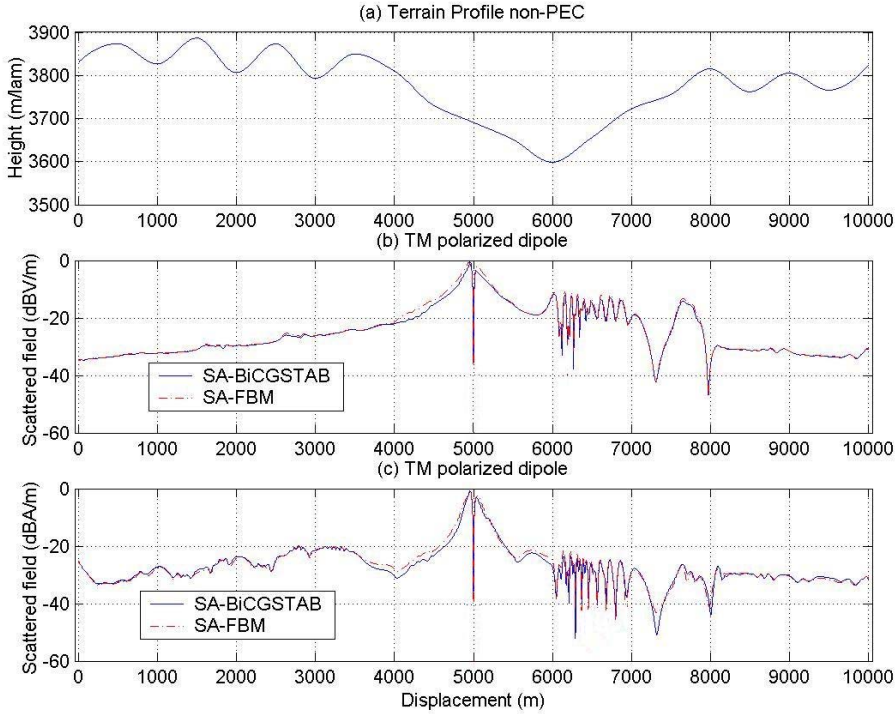

Figure 4.15 Scattered fields from a 10000λ width rough surface

A non-PEC terrain profile of width 10000λ with the surface impedance $\eta_s = 20 + j15$ is depicted in Figure 4.16. The parameters for SA-BiCGSTAB method are included in Table 4.2. Since the geometry is going upwards, the medium saddle point is located on the positive real axis. The surface is considered to be illuminated by a dipole antenna located at a 50λ height above in the middle point of the terrain. The average radiated power is now 100 Watts.

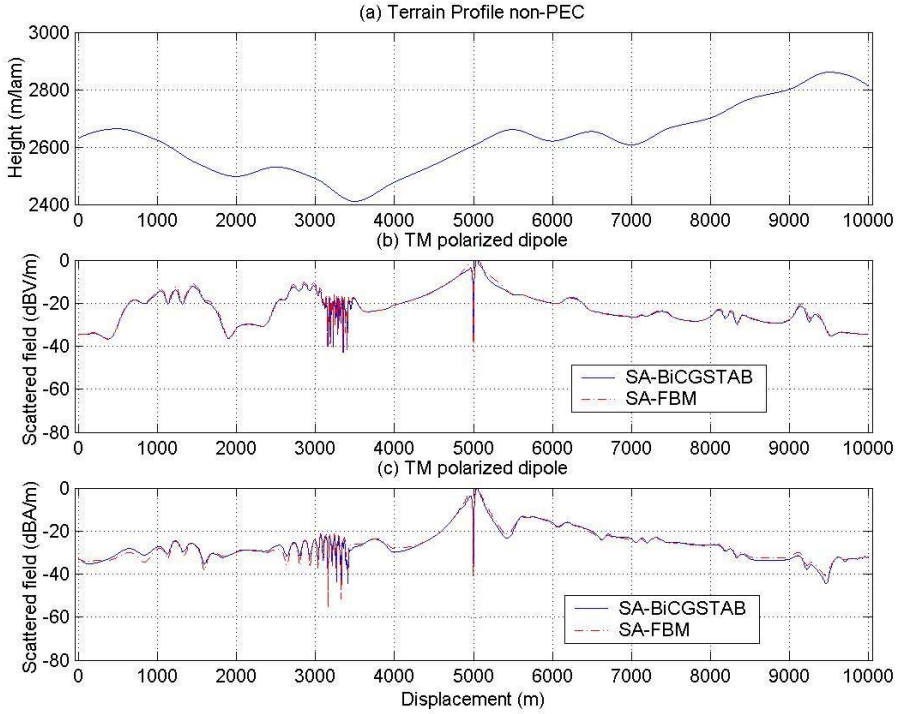

Figure 4.16 Scattered fields from a 10000λ width rough surface

Last example in Figure 4.17 is a rough surface of width 20000λ yielding 200000 unknowns to be solved in order to evaluate the scattered field for both polarizations. Imperfect conducting case with the surface impedance $\eta_s = 20 + j15$ is considered. The parameters for SA-BiCGSTAB method are included in Table 4.2. Since the geometry is going downwards, the medium saddle point is located on the negative real axis. The surface is considered to be illuminated by a dipole antenna located at a 90λ height above in the middle

point of the terrain. The average radiated power is 90 Watts. To show the convergence ability, the results are compared with the SA-FBM method.

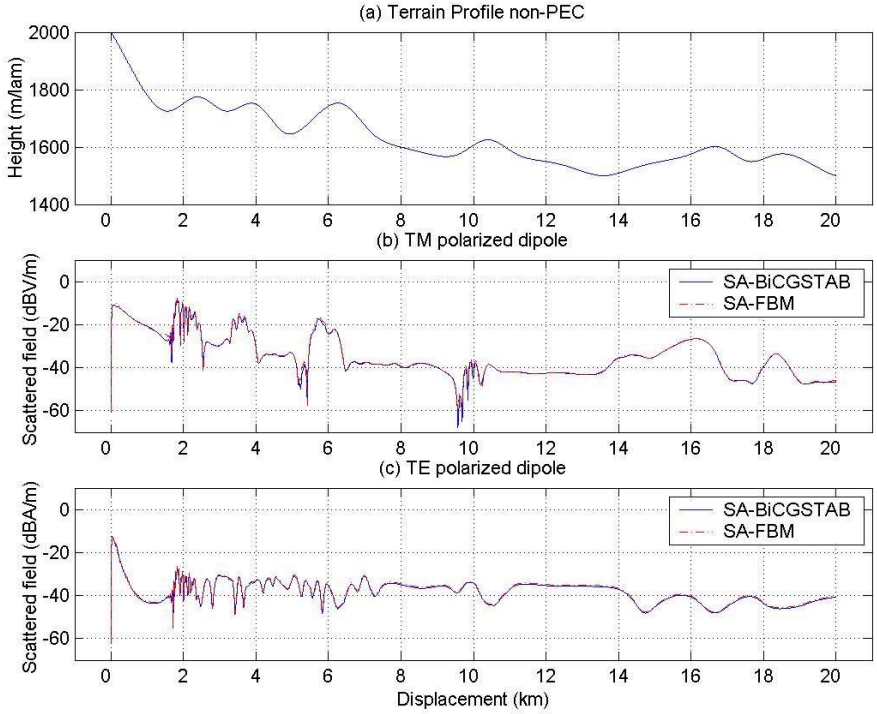

Figure 4.17 Scattered fields from a 20000λ width rough surface

4.4 Computational Cost of SA-BiCGSTAB for Rough Surfaces

Investigations over rough surface profiles show that the SA-BiCGSTAB method obtains numerically accurate results for both horizontal and vertical polarization cases. In order to compute the computational cost of the method with MoM and the conventional BiCGSTAB method, the computation time versus the number of unknowns N are illustrated in Table 3.3. As mentioned before, convergence rate for conjugate gradient type methods strongly depend on the number of unknowns N. Nevertheless, our examinations on the terrain profiles have shown that BiCGSTAB converges to the exact solution within 20

to 40 iterations for TM polarization and within 8 to12 iterations for TE polarization up to 200000 unknowns when the residual error is considered to be 10^{-3}.

N	**LU inversion(s)**	**BiCGSTAB/iter (s)**	**Number of integ. points**	**SA-BiCGSTAB/iter (s)**
2000	5018.5	13.26	312	1.69
5000	NA	81.47	700	8.47
10000	NA	332.15	425	8.91
20000	NA	NA	296	15.55
100000	NA	NA	458	97.16
200000	NA	NA	538	199.85

Table 4.3 Computational cost for SA-BiCGSTAB method

Table 3.4 can be utilized for the investigation of the computational cost,. The CPU-time values are obtained on Intel PIII microprocessor having 1000 MHz clock frequency. CPU-time results show that the computational cost depends on the number of integral points which vary based on the geometry of the terrain profiles. Nevertheless, it is clearly seen that when we increase the number of unknowns for a fixed number of integral points, the spectral acceleration algorithm yields an operation count of $O(N)$. The situation can be proved by looking at the cases for N = 2000 and N = 20000. Also, since the number of integral points for N = 5000 are twice as much as for those for N = 10000, the computation time for both cases are nearly the same. As depicted in Figure 3.22, the computational cost is really overwhelming for the MoM, since the operational cost is proportional with $O(N^3)$ because of the LU decomposition method. The enhanced operational cost (when compared with the MoM) of conventional BiCGSTAB method can not compete with SA-BiCGSTAB that it still requires $O(N^2)$ operations per iteration.

The comparisons reveal that SA-BiCGSTAB can be used as a numerically accurate solution technique instead of MoM or BiCGSTAB over terrain profiles in both horizontal and vertical polarization cases with minimal storage requirements and rapid convergence behavior. The total cost of operations are reduced to *O(N).*

4.5 Limitations of the Spectral Acceleration Algorithm for the Terrain Profiles

Analysis on a number of numerical tests on spectral acceleration technique over terrain profiles show that, the algorithm works properly up to 4 degrees of inclination angle which is an angle between the deformed contour of integration and the real axis in the complex angular space. For more complex geometries (very undulating), the inclination angle becomes too small so that the deformed contour may nearly overlap with the real axis where the integrand may exhibit a very oscillatory behavior. Because of these oscillations, the numerical integration is difficult. Also the treat of the exponential growth of the integrand due to the outermost saddle point could be formed. Thus, the contribution from the weak field may unexpectedly increase which will avoid the convergence ability of the method.

To overcome this limitation, the entire geometry can be split into several sections and the inclination angle of each section can be considered separately. After the analysis of each section, a new integration path can be formed to evaluate the weak group contributions. The partition process can be repeated several times along the profile of the terrain depending upon the geometry. The cost of this process is to recompute the integrand for each integration path, but it is carried out only few times and hence, the operation count is still *O(N).*

Chapter 5

Conclusions and Future Work

In this thesis, conventional BiCGSTAB and SA-BiCGSTAB methods over various kinds of terrain profiles rough in one dimension and multi valued surfaces have been implemented by a large number of examples.

In order to compare the accuracy of BiCGSTAB method, results have been tested with reference MoM solutions for both TM and TE polarization cases up to $N = 2000$ unknowns. This limitation is due to storage requirement to keep interaction matrices of MoM and due to computational cost of the direct solution technique, LU decomposition which has an operation count of $O(N^3)$. Numerical examples have shown that BiCGSTAB methods yield precise current distributions with a computational cost of $O(N^2)$ per iteration.

BiCGSTAB has also been tested on a reentrant target surface (a ship on the sea) and the accuracy of the results is compared with generalized FBM (GFBM). As stated earlier, GFBM has been developed to defeat divergence characteristics of FBM due to the multi valued portions of the surface leading large off-diagonal entries in the impedance matrices for TM and TE polarizations. But it should be noted that the number of iterations to reach the desired level of error is increased.

Later on, spectrally accelerated BİCGSTAB method has been applied over slightly rough surfaces with a height deviation multiple of few wavelengths. Results of SA-BiCGSTAB method with respect to MoM and BiCGSTAB method have been investigated. Also a multi valued target surface

has been examined and its convergence capability is compared with spectrally accelerated generalized forward backward (SA-GFBM) method.

This is an important case that, the non-stationary behavior of SA-BiCGSTAB method is not affected by the reentrant surface and operational count compared with conventional BiCGSTAB method is reduced significantly. Numerical results for quasi-planar surfaces have shown that SA algorithm works properly with BiCGSTAB.

After that, modified spectral acceleration in conjunction with BiCGSTAB method has been experimented for rough surfaces with a height deviation multiple of several wave lengths. Accuracy of the method has been tested with original BiCGSTAB method and SA-FBM. The evaluation of scattered field has also been addressed. The exact computation of the field requires computational cost of $O(N^2)$ which is really high since the problem is electrically large. Hence, an analogous procedure can be applied by means of spectral acceleration to fasten the matrix - vector multiplication. Consequently, the computation of scattered field yields to $O(N)$. Lastly the limitations of spectral acceleration have been discovered.

The main novelty of this work is to present electrically large rough surface scattering analyses with spectrally accelerated BiCGSTAB method up to 200000 unknowns. Another innovation is the examination of multi-valued surface profiles with a non-stationary technique without any computational complexity or high memory requirements. The variants of stationary techniques developed to treat such profiles can not compete with SA-BiCGSTAB method when the re-entrant surface is electrically large. Based on these results, we see that non-stationary iterative procedures be considered for the use with general scattering problems. The inherent robustness of these techniques allows their convergence speed to slow down through the geometry changes which transitioned the stationary techniques from very rapid convergence to

divergence. Their convergence ability is independent of the ordering used when forming the impedance matrix. The primary disadvantage of the non-stationary techniques is that they require more iteration to converge. One other drawback is that, the number of iteration varies with the increasing unknown number N. However, recent tests show that up to 200000 unknowns, iteration number varies within reasonable limits (between 20 and 40 for TM polarization and between 5 and 12 for TE polarization cases due to the better conditioning of TE impedance matrix over TM impedance matrix).

Future work will focus on accelerating CPU processing time of SA-BiCGSTAB method. Since it depends upon matrix – vector multiplies rather than forward – backward substitutions, it is well suited to parallel processing. Furthermore, some modifications corresponding to the spectral acceleration algorithm may be implemented to analyze very undulating terrain profiles in the rural areas.

Appendix A

Spectral Acceleration for the Quasi-planar Surfaces for the Backward Propagation

A.I Horizontal Polarization

The backward propagating field can be expressed as

$$E_b(\boldsymbol{\rho}_n) = \bar{\mathbf{Z}}^b . \mathbf{I} = \sum_{m=n+1}^{N} I_m Z_{nm} . \quad \text{(A.1)}$$

Similar to the forward propagation case, superscript *b* at the top of the impedance matrix denotes the upper triangular part. For simplicity, only the forward propagating field will be focused in here, the backward part can be treated in the same manner and is given in appendices.

The backward field is also divided into two groups; the contributions coming from the strong region and the contributions due to weak region, i.e.,

$$\bar{\mathbf{Z}}^b . \mathbf{I} = E_f(\boldsymbol{\rho}_n) = E_{f,w}(\boldsymbol{\rho}_n) + E_{f,s}(\boldsymbol{\rho}_n) \quad \text{(A.2)}$$

where the strong and weak contributions can be written as

$$E_{b,s}(\boldsymbol{\rho}_n) = \sum_{m=n+N_s}^{n+1} I_m Z_{nm} \quad \text{(A.3)}$$

$$E_{b,w}(\boldsymbol{\rho}_n) = \sum_{m=N}^{n+N_s+1} I_m Z_{nm} \quad \text{(A.4)}$$

with the impedance matrix elements defined in (2.48). It should be noted that the indices at the right hand sides of (A.3) and (A.4) are in descending order. The radiations of the strong group contributions are found in the conventional matrix-vector multiplication by evaluating the exact impedance elements. However, weak group contribution is obtained by employing spectral representation of the two-dimensional Green's function.

$$G(\rho_n, \rho_m) = \frac{-j}{4\pi} \int_{C_\phi} e^{jk[(x_n - x_m)\cos\phi - (z_n - z_m)\sin\phi]} d\phi \qquad \text{(A.5)}$$

where C_ϕ is the contour of integration in the complex ϕ space shown in Figure 3.25. We also need the derivative of the Green's function due to normal vector at the source point, which takes place within the off-diagonal entries of the impedance matrix defined in (2.49)

$$\frac{\partial G(\rho_n, \rho_m)}{\partial n_m} = \frac{k}{4\pi} \int_{C_\phi} [\cos\theta_m \cos\phi + \sin\theta_m \sin\phi] \cdot e^{jk[(x_n - x_m)\cos\phi - (z_n - z_m)\sin\phi]} d\phi \qquad \text{(A.6)}$$

where θ_m is the angle between the normal vector at the source point $\hat{n}_m$ and the unit vector $-\hat{x}$.

Substituting equations (A.5) and (A.6) into (A.4) and interchanging the summation and integration gives,

$$E_{b,w}(\boldsymbol{\rho}_n) = -\frac{\omega\mu}{4\pi} \int_{C_\phi} F_n(\phi) e^{-jk(z_n \sin\phi)} d\phi \qquad \text{(A.7)}$$

where

$$F_n(\phi) = \sum_{m=N}^{n+N_s+1} I_m \Delta x_m \left\{ 1 - \frac{\eta_m}{\eta_0} [\cos\theta_m \cos\phi + \sin\theta_m \sin\phi] \right\} \cdot e^{jk[(x_n - x_m)\cos\phi + z_m \sin\phi]} \qquad \text{(A.8)}$$

The integrand $F_n(\phi)$ can be represented via recursive formulation:

$$F_n(\phi) = F_{n+1}(\phi)e^{jk(x_n - x_{n+1})\cos\phi} + I_{ns}\Delta x_{ns}\left\{1 - \frac{\eta_{ns}}{\eta_0}[\cos\theta_{ns}\cos\phi + \sin\theta_{ns}\sin\phi]\right\} \cdot e^{jk\left[(x_n - x_{ns})\cos\phi + z_{ns}\sin\phi\right]} \tag{A.9}$$

with $F_n(\phi) = 0$ for $n > N - N_s - 1$ .The subscript *ns* is equal to $n+N_s+1$. By employing this recursive procedure a great reduction of computational cost is obtained. Due to this formula, the integrand of *n*th element updates itself in terms of the previous one, which keeps all of the weak interactions until that receiving element. Hence, operation count required for the weak region process is *O(N)*.

A.II Vertical Polarization

If we use MFIE formulation for TE polarization, the backward propagating magnetic field, is the sum of strong and weak contributions,

$$H_b(\boldsymbol{\rho}_n) = H_{b,w}(\boldsymbol{\rho}_n) + H_{b,s}(\boldsymbol{\rho}_n) \tag{A.10}$$

with

$$H_{b,s}(\boldsymbol{\rho}_n) = \sum_{m = n-N_s}^{n+1} I_m Z_{nm} \tag{A.11}$$

and

$$H_{b,w}(\boldsymbol{\rho}_n) = \sum_{m=N}^{n+N_s+1} I_m Z_{nm} \tag{A.12}$$

where the elements of the impedance matrix is defined in (2.52). It should be noted that the indices at the right hand sides of (A.3) and (A.4) are in descending order. The radiations of the strong group contributions are found in the conventional matrix-vector multiplication by evaluating the exact impedance elements. However, weak group contribution is obtained by employing spectral representation of the two-dimensional Green's function.

Than by using (A.5) and (A.6), the forward propagating magnetic field is given by

$$H_{b,s}(\boldsymbol{\rho}_n) \;=\; -\frac{\mathrm{k}}{4\pi}\int_{C_\phi} F_n(\phi)e^{-jk(z_n\sin\phi)}d\phi \;\;, \qquad \text{(A.13)}$$

where

$$F_n(\phi) \;=\; \sum_{m\,=\,N}^{n+N_s+1} I_m\Delta x_m\left\{\cos\theta_m\cos\phi \;+\; \sin\theta_m\sin\phi \;-\; \frac{\eta_m}{\eta_0}\right\} \qquad \text{(A.14)}$$
$$\cdot\, e^{jk\left[(x_n\,-\,x_m)\cos\phi_n\,+\,z_m\sin\phi\right]}\,.$$

The integrand $F_n(\phi)$ can be evaluated via a recursive formulation given by

$$F_n(\phi) = F_{n+1}(\phi)e^{jk(x_n-x_{n+1})\cos\phi} + I_{ns}\Delta I_{ns}\left\{\cos\theta_{ns}\cos\phi+\sin\theta_{ns}\sin\phi-\frac{\eta_m}{\eta_0}\right\}$$
$$\cdot\, e^{jk\left[(x_n\,-\,x_{ns})\cos\phi_n+z_{ns}\sin\phi\right]} \qquad \text{(A.15)}$$

with $F_n(\phi)=0$ for $n > N-N_s-1$. The subscript *ns* is equal to $n+N_s+1$. By applying this recursive process on the integrand, we again provide an operation count of *O(N)*.

Appendix B

Spectral Acceleration for the Rough Surfaces for the Backward Propagation

B.I Horizontal Polarization

The backward propagating field can be expressed as

$$E_b(\boldsymbol{\rho}_n) = \bar{\mathbf{Z}}^b . \mathbf{I} = \sum_{m=n+1}^{N} I_m Z_{nm} . \quad \text{(B.1)}$$

Similar to the forward propagation case, superscript *b* at the top of the impedance matrix denotes the upper triangular part. For simplicity, only the forward propagating field will be focused in here, the backward part can be treated in the same manner and is given in appendices.

The backward field is also divided into two groups; the contributions coming from the strong region and the contributions due to weak region, i.e.,

$$\bar{\mathbf{Z}}^b . \mathbf{I} = E_f(\boldsymbol{\rho}_n) = E_{f,w}(\boldsymbol{\rho}_n) + E_{f,s}(\boldsymbol{\rho}_n) \quad \text{(B.2)}$$

where the strong and weak contributions can be written as

$$E_{b,s}(\boldsymbol{\rho}_n) = \sum_{m=n+N_s}^{n+1} I_m Z_{nm} \quad \text{(B.3)}$$

$$E_{b,w}(\boldsymbol{\rho}_n) = \sum_{m=N}^{n+N_s+1} I_m Z_{nm} \quad \text{(B.4)}$$

with the impedance matrix elements defined in (2.48). It should be noted that the indices at the right hand sides of (B.3) and (B.4) are in descending order. The radiations of the strong group contributions are found in the conventional matrix-vector multiplication by evaluating the exact impedance elements. However, weak group contribution is obtained by employing spectral representation of the two-dimensional Green's function.

$$G(\rho_n, \rho_m) = \frac{-j}{4\pi} \int_{C_\phi} e^{jk[(x_n - x_m)\cos\phi - (z_n - z_m)\sin\phi]} d\phi \tag{B.5}$$

where C_ϕ is the contour of integration in the complex ϕ space shown in Figure 3.25. We also need the derivative of the Green's function due to normal vector at the source point, which takes place within the off-diagonal entries of the impedance matrix defined in (2.49)

$$\frac{\partial G(\rho_n, \rho_m)}{\partial n_m} = \frac{k}{4\pi} \int_{C_\phi} [\cos\theta_m \cos\phi + \sin\theta_m \sin\phi] \cdot e^{jk[(x_n - x_m)\cos\phi - (z_n - z_m)\sin\phi]} d\phi \tag{B.6}$$

where θ_m is the angle between the normal vector at the source point $\hat{n}_m$ and the unit vector $-\hat{x}$.

Substituting equations (B.5) and (B.6) into (B.4) and interchanging the summation and integration gives,

$$E_{b,w}(\boldsymbol{\rho}_n) = -\frac{\omega\mu}{4\pi} \int_{C_\phi} F_n(\phi) d\phi \tag{B.7}$$

where

$$F_n(\phi) = \sum_{m=N}^{n+N_s+1} I_m \Delta x_m \left\{ 1 - \frac{\eta_m}{\eta_0} [\cos\theta_m \cos\phi + \sin\theta_m \sin\phi] \right\} \cdot e^{jk[(x_n - x_m)\cos\phi - (z_n - z_m)\sin\phi]} \tag{B.8}$$

The integrand $F_n(\phi)$ can be represented via recursive formulation:

$$F_n(\phi) = F_{n+1}(\phi) e^{jk\left[(x_n - x_{n+1})\cos\phi + (z_n - z_{n+1})\sin\phi\right]}$$
$$+ I_{ns}\Delta I_{ns}\left\{\cos\theta_{ns}\cos\phi + \sin\theta_{ns}\sin\phi - \frac{\eta_m}{\eta_0}\right\} \qquad \text{(B.9)}$$
$$. e^{jk\left[(x_n - x_{ns})\cos\phi + (z_n - z_{ns})\sin\phi\right]}$$

with $F_n(\phi) = 0$ for $n > N - N_s - 1$ .The subscript *ns* is equal to $n+N_s+1$. By employing this recursive procedure a great reduction of computational cost is obtained. Due to this formula, the integrand of *n*th element updates itself in terms of the previous one, which keeps all of the weak interactions until that receiving element. Hence, operation count required for the weak region process is *O(N)*.

B.II Vertical Polarization

If we use MFIE formulation for TE polarization, the backward propagating magnetic field, is the sum of strong and weak contributions,

$$H_b(\boldsymbol{\rho}_n) = H_{b,w}(\boldsymbol{\rho}_n) + H_{b,s}(\boldsymbol{\rho}_n) \qquad \text{(B.10)}$$

with

$$H_{b,s}(\boldsymbol{\rho}_n) = \sum_{m = n - N_s}^{n+1} I_m Z_{nm} \qquad \text{(B.11)}$$

and

$$H_{b,w}(\boldsymbol{\rho}_n) = \sum_{m=N}^{n+N_s+1} I_m Z_{nm} \qquad \text{(B.12)}$$

where the elements of the impedance matrix is defined in (2.52). It should be noted that the indices at the right hand sides of (B.11) and (B.12) are in descending order. The radiations of the strong group contributions are found in the conventional matrix-vector multiplication by evaluating the exact impedance elements. However, weak group contribution is obtained by employing spectral representation of the two-dimensional Green's function.

Than by using (B.5) and (B.6), the forward propagating magnetic field is given by

$$H_{b,s}(\boldsymbol{\rho}_n) \;=\; -\frac{\mathrm{k}}{4\pi}\int_{C_\phi} F_n(\phi)d\phi \;\;, \tag{B.13}$$

where

$$F_n(\phi) \;=\; \sum_{m\,=\,N}^{n+N_s+1} I_m \Delta x_m \left\{ \cos\theta_m \cos\phi \;+\; \sin\theta_m \sin\phi \;-\; \frac{\eta_m}{\eta_0} \right\} \tag{B.14}$$
$$\cdot\, e^{jk\left[(x_n \,-\, x_m)\cos\phi \,-(z_n - z_m)\sin\phi\right]} \cdot$$

The integrand $F_n(\phi)$ can be evaluated via a recursive formulation given by

$$F_n(\phi) = F_{n+1}(\phi) e^{jk\left[(x_n - x_{n+1})\cos\phi - (z_n - z_{n+1})\sin\phi\right]}$$
$$+ I_{ns}\Delta I_{ns} \left\{ \cos\theta_{ns}\cos\phi + \sin\theta_{ns}\sin\phi - \frac{\eta_m}{\eta_0} \right\} \tag{B.15}$$
$$\cdot\, e^{jk\left[(x_n \,-\, x_{ns})\cos\phi - (z_n - z_{ns})\sin\phi\right]}$$

with $F_n(\phi) = 0$ for $n > N - N_s - 1$. The subscript *ns* is equal to $n+N_s+1$. By applying this recursive process on the integrand, we again provide an operation count of *O(N)*.

Bibliography

[1] Hata, Masaharu, “Empirical Formula for Propagation Loss in Land Mobile Radio Services”, *IEEE Trans. on Vehicular Technology,* vol. VT-29, no. 3, pp. 317-325, Aug. 1980.

[2] S. Ayasli, “SEKE: A computer model for low altitude radar propagation over irregular terrain”, *IEEE Trans. Antennas and Propagat.,* vol. AP-34, pp. 1013-1023, Aug. 1986.

[3] R. J. Luebbers, “Finite conductivity uniform GTD versus knife edge diffraction in prediction of propagation path loss”, *IEEE Trans. Antennas and Propagat.,* vol. AP-32, pp. 70-76, Jan. 1984.

[4] C. L. Rino and H. D. Ngo, “Forward propagation in half-space with an irregular boundary”, *IEEE Trans. Antennas and Propagat.,* vol. 45, pp. 1340-1347, Sept. 1997.

[5] D. J. Donohue and J. R. Kuttler, “Propagation modeling over terrain using parabolic wave equation”, *IEEE Trans. Antennas and Propagat.,* vol. 48, pp. 260-277, Feb. 2000.

[6] A. E. Barrios, “A terrain parabolic equation model for propagation in the troposphere”, *IEEE Trans. Antennas and Propagat.,* vol. 42, pp. 90-98, Jan. 1994.

[7] R. F. Harrington, *Field Computation by Moment Method*, New York: IEEE Press, 1993.

[8] R. Janaswamy, “A Fredholm integral equation method for propagation over small terrain irregularities”, *IEEE Trans. Antennas and Propagat.,* vol. 40, pp. 1416-1422, Sept. 1994.

[9] J. T. Hviid, J. B. Anderson, J. Toftgard, and J. Bojer, “Terrain based propagation model for rural area – an integral equations approach”, *IEEE Trans. Antennas and Propagat.,* vol. 43, pp. 41-46, Jan. 1995.

[10] J. T. Johnson, R. T. Shin, J. C. Eidson, L. Tsang, and J. A. Kong, “A method of moments model for VHF propagation”, *IEEE Trans. Antennas and Propagat.,* vol. 45, pp. 115-125, Jan. 1997.

[11] C. Brennan and P. J. Cullen, “Application of the fast far-field approximation to the computation of UHF path loss over irregular terrain”, *IEEE Trans. Antennas and Propagat.,* vol. 46, pp. 881-890, June. 1998.

[12] D. Holliday, L. L. DeRaad Jr., and G. J. St.-Cyr, “Forward-Backward: A new method for computing low-grazing scattering”, *IEEE Trans. Antennas and Propagat.,* vol. 44, pp. 722-729, May 1996.

[13] R. Barret, M. Berry, T. F. Chan, J. Demmel, J. Donato, J. Dongarra, V. Eijkhout, R. Poza, C. Romine, and H. Ban der Vort, “Templates for the Solution of Linear Systems: Building Blocks for Iterative Methods”, Philadelphia, PA: SIAM, 1994.

[14] C. F. Smith, A. F. Peterson, and R. Mittra, “The biconjugate Gradient Method for electromagnetic scattering”, *IEEE Trans. Antennas and Propagat.,* vol. 38, pp. 938-940, June 1990.

[15] P. Cao and C. Macaskill, “Iterative techniques for rough surface scattering problems”, *Wave Motion*, vol. 21, pp. 209-229, 1995.

[16] D. J. Donohue, H. –C. Ku, and D. R. Thompson, “Application of iterative moment-method solutions to ocean surface radar scattering”, *IEEE Trans. Antennas and Propagat.,* vol. 46, pp.121-132, Jan. 1998.

[17] F. Chen, “The numerical calculation of two-dimensional rough surface scattering by the conjugate gradient method”, *Int. J. Remote Sensing,* vol. 17, no. 4, pp. 801-808, 1996.

[18] H.-T. Chou and J. T. Johnson, “A novel acceleration for the computation of scattering from rough surfaces with the forward-backward method”, *Radio Sci.,* vol. 33, pp. 1277-1287, Jun. 1998.

[19] J. A. Lopez, M. R. Pino, F. Obelleiro, J. L. Rodriguez, “Application of the spectral acceleration forward-backward method to coverage analysis over terrain profiles”, *J. of Electromagn. Waves and Appl.,* vol. 15, no. 8, pp. 1049-1074, 2001.

[20] A. Valero and R. G. Rojas, “Fast analysis electromagnetic scattering from finite strip gratings on a grounded dielectric slab”, *Radio Sci.*, 2000

[21] M. R. Pino, L. Landesa, J. L. Rodriguez, F. Obelleiro, and R. J. Burkholder, “The generalized forward-backward method for analyzing the scattering from targets on ocean-like rough surfaces”, *IEEE Trans. Antennas and Propagat.,* vol. 47, pp. 961-969, June 1999.

[22] L. N. Medgyesi-Mitschang, J. M. Putnam, “Integral Equation Formulations for Imperfectly Conducting Scatterers”, *IEEE Trans. Antennas and Propagat.,* vol. AP-33, no. 2, Feb. 1985.

[23] R. D. Graglia and P. L. E. Uslenghi, “Electromagnetic scattering by impedance bodies of revolution”, *Nat. Radio Sci. Meeting, session URSI/B-6-3,* paper 4, Univ. Houston, Houston, TX, 23-26 May 1983.

[24] C. A. Balanis, *Advanced Engineering Electromagnetics*, John Wiley & Sons, 1989.

[25] E. A. Ericson and D. R. Lyzenga, “Performance of a numerical iterative solution of the surface current integral equation for surfaces containing small radii of curvature”, *Radio Sci.,* vol.33, no. 2, pp. 205-217, Mar. 1998.

[26] D. A. Kapp and G. S. Brown, “A new numerical-method for rough surface scattering calculations”, *IEEE Trans. Antennas and Propagat.,* vol. 44, pp.711-722, May 1996.

[27] C. A. Balanis, *Antenna Theory Analysis And Design,* John Wiley & Sons, 1997.

[28] W. J. Pierson, L. Moskowitz, “A proposed spectral form for fully developed wind seas based on the similarity theory of S. A. Kitaigorodskii”, *J. Geophys. Res.,* vol. 69, pp. 5181-5190, 1964.

[29] M. R. Pino, R. J. Burkholder, and F. Obelleiro, “Spectral Acceleration of the Generalized Forward-Backward Method”, *IEEE Trans. Antennas and Propagat.,* vol. 50, no. 6, June 2002.

[30] R. G. Kouyoumjian and P. H. Pathak, “A uniform geometrical theory of diffraction for an edge in a perfectly conducting surface”, *Proc. IEEE,* vol. 62, no. 5, pp.1418-1461, 1974.

[31] C. A. Tunç, “Application of Spectral Acceleration Forward-Backward Method for Propagation over Terrain”, *M. S. Thesis in Electrical and Electronics Engineering,* Bilkent University, Sept. 2003.